Design and Evaluation of the **M**otor **A**ssisted **R**obotic **S**tereotaxy System
MARS

Maximilian Heinig

Dissertation

Universität zu Lübeck

Institut für Robotik und Kognitive Systeme

Aus dem Institut für Robotik und Kognitive Systeme
der Universität zu Lübeck

Direktor:
Prof. Dr.-Ing. Achim Schweikard

Design and Evaluation of the Motor Assisted Robotic Stereotaxy System MARS

Inauguraldissertation
zur
Erlangung der Doktorwürde
der Universität zu Lübeck
— Aus der Sektion Informatik —

Vorgelegt von Maximilian Johannes Heinig
geboren in München

Lübeck, im Juni 2012

Maximilian Heinig – Research Associate
Institute for Robotics and Cognitive Systems
Universität zu Lübeck
Ratzeburger Allee 160
23538 Lübeck, Germany

ลาก่อนครับ ขอบคุณมากสำหรับปลาทุกตัว

(ดักกลาส อดัม)

Zusammenfassung

Diese Arbeit befasst sich mit der Entwicklung und klinischen Erprobung eines stereotaktischen Roboters für neurochirurgische Eingriffe sowie eines neuen intrakraniellen Lokalisationsverfahrens für neurochirurgische Instrumente. Anwendungsszenarien für den Roboter sind Hirnbiopsien z.B. bei Tumoren oder die Tiefenhirnstimulation beispielsweise bei der Behandlung von Morbus Parkinson.

Basierend auf einer detaillierten Analyse vorhandener manueller und robotischer Stereotaxiesysteme werden die Anforderungen an ein neues, hybrides Robotersystem erarbeitet, welches die Vorteile der beiden Herangehensweisen kombiniert und sowohl eine manuelle als auch automatische Positionierung ermöglicht. Kern der Arbeit ist die hieraus entstandene Entwicklung und Realisierung des **M**otor **A**ssistierten **R**obotischen **S**tereotaxiesystems, kurz **MARS**.

Die kinematische Kette des MARS besteht aus fünf Achsen, deren Anordnung sich an dem klinisch erprobten ZD-Stereotaxiesystem der inomed Medizintechnik GmbH orientiert. Die Aktorik, Sensorik und weitere Komponenten sowie der mechanische und elektrische Aufbau des MARS werden detailliert beschrieben.

In zahlreichen Experimenten wird zunächst die Eignung des MARS für den chirurgischen Eingriff evaluiert, indem Absolut- und Wiederholgenauigkeit gemessen werden, die elektromagnetische Verträglichkeit des Systems mit anderen Geräten im Operationssaal validiert wird und die Anwendungsgenauigkeit im simulierten Eingriff ermittelt wird. Nach erfolgreicher Testung erfolgt der klinische Einsatz des MARS mit komplikationsloser Entnahme einer Hirntumorbiopsie.

Der zweite Teil der Arbeit beschäftigt sich mit der Lokalisation von Instrumenten im Gehirn. Verschiedene Fehlerquellen wie z.B. Interaktion von Instrument und Hirngewebe können intraoperativ zu einem Abweichen des Instruments von der geplanten Trajektorie führen mit möglicherweise fatalen Konsequenzen. Eine kontinuierliche Positionsüberprüfung ist daher von großer Relevanz für neurochirurgische Eingriffe. Ein Lokalisationsverfahren für Sonden basierend auf statischen Magnetfeldern wird entwickelt und evaluiert. Neben der hohen räumlichen Auflösung zeichnet sich das Verfahren dadurch aus, dass es keine zusätzlichen Komponenten im Gehirn des Patienten benötigt.

Zusammenfassend konnte gezeigt werden, dass MARS ein äußerst präzises, sicheres und mobiles Werkzeug für die stereotaktische Neurochirurgie darstellt. Die erfolgreiche klinische Evaluation des Roboters sowie dessen Kombination mit dem magnetischen Lokalisationsverfahren verdeutlicht die Qualität des Systems.

Abstract

The scope of this thesis is the development and clinical evaluation of a robotic system for stereotactic neurosurgery. Furthermore, a new intracranial localization method for neurosurgical instruments is presented. Potential clinical applications for the robot are brain biopsies, e.g. for tumors or deep brain stimulation, e.g. in the treatment of Parkinson's disease.

The requirements for a new hybrid robotic system are derived from a detailed analysis of existing manual and robotic stereotactic systems. The aim of the development is to combine the advantages of the two approaches and to enable both, manual and automatic positioning. The core of this work is the development and implementation of the **M**otor **A**ssisted **R**obotic **S**tereotaxy system, short **MARS**.

The kinematic chain of the MARS consists of five axes. Their alignment is similar to that of the clinically established ZD stereotaxy system from the industrial partner inomed Medizintechnik GmbH. The actuators, sensors and other components as well as the mechanical and electrical design of the MARS are described in detail.

The MARS is evaluated in numerous experiments regarding its suitability for surgical interventions. Therefore, its absolute accuracy and repeatability are measured. Then, the electromagnetic compatibility of the system with other devices in the operating theater is validated and its application accuracy is determined in a simulated surgery. After successful testing, the MARS is clinically evaluated in a brain tumor biopsy.

The second part of the thesis addresses the localization of instruments in the brain. Various error sources such as probe-tissue interaction during surgery can cause a deviation of the instrument from the planned trajectory with potentially fatal consequences. Continuous monitoring of the position of the instrument is hence of great relevance in neurosurgical interventions. A method for localization of probes based on static magnetic fields is developed and evaluated. The localization method is characterized by its high spatial resolution and the fact that it does not require additional components in the brain of the patient.

In summary, the MARS presents a highly accurate, safe and mobile tool for stereotactic neurosurgery. The successful clinical evaluation of the robot and its combination with the magnetic localization method emphasize the quality of the system.

Contents

Abbreviations

3D	3-dimensional
AC	Alternating current
AC	Anterior Commisure
ADC	Analog-digital converter
AMR	Anisotropic magneto resistive
CAD	Computer-aided design
CDC	Communication Device Class
CE	Communauté Européenne
CFRP	Carbon-fiber-reinforced polymer
CLK	Clock
CoS	Coordinate system
CSF	Cerebrospinal fluid
CT	Computed Tomography
DBS	Deep Brain Stimulation
DC	Direct current
DH	Denavit-Hartenberg
DOF	Degrees of freedom
EMI	Electro-magnetic interference
FDA	Food and Drug Administration
FEM	Finite element method
GI	Gastro intestinal
GPi	Globus pallidus internus
GUI	Graphical User Interface
LED	Light-emitting diode
MARS	Motor Assisted Robotic Stereotaxy System
MCU	Micro-controller unit
MDU	Micro drive unit
MER	Micro electrode recording
MISO	Master in slave out
MOSI	Master out slave in
MRT	Magnetic Resonance Tomography
OT	Operating theatre

PACS   Picture archiving and communication system
PC   Posterior Commisure
PCB   Printed Circuit Board
PD   Parkinson's disease
PID   Proportional integral derivative
Pin   Positive intrinsic negative
PSD   Position sensitive diode
RM   Riechert-Mundinger
RMS   Root mean square
SPI   Serial peripheral interface
SQUID   Superconducting Quantum Interference Device
SS   Slave select
STN   Subthalamus nucleus
UKSH   Universitätsklinikum Schleswig-Holstein
US   Ultrasound
USB   Universal serial bus
Vim   Ventral intermedius nucleus
VOI   Volume of interest
ZD   Zamoranow-Duchovny

1 Introduction

The scope of this thesis is to develop a hybrid robotic system for stereotactic neurosurgery. The system incorporates means to validate the intracranial position of a probe when penetrating into tissue. To clarify the use of such a system, a brief overview over the range of applications is given in this introduction.

First, the generic workflow for stereotactic neurosurgery based on the analysis of various interventions is introduced. Second, two examples with high clinical relevance are presented: The treatment of Parkinson's disease (PD) using deep brain stimulation (DBS) and the collection of tissue samples for biopsies in oncology. To conclude, the structure of the remaining thesis is presented.

Neurosurgery is a very complex and delicate craft. In this work, the demanding processes concerning the medical aspect are simplified to enable the technically experienced reader to understand the challenges. No information is given on how a diagnosis is established, as this would go beyond the scope of this work.

1.1 Generic workflow of stereotactic interventions

A set of stereotactic interventions was analyzed to derive a generic workflow for stereotactic interventions [1, 2, 3, 4]. Neurosurgeons usually abide by the following steps:

- **Fixation of the stereotactic base unit:** The patient is anesthetized and the base unit is attached to the patient's head using sharp tipped pins (Figure 1.1, left). The locations of the pins are chosen such, that they do not cause interference with the volume of interest (VOI) in the 3-dimensional (3D) imaging. Furthermore, they have to allow for easy mounting of the localizer.

- **3D imaging:** The localizer is attached to the base unit which is fixed to the patient's head (Figure 1.1, center). A computed tomograph (CT) or magnetic resonance tomograph (MRT) is used to acquire a 3D image of the patient's head with the localizer attached to the base ring (Figure 1.1, right).
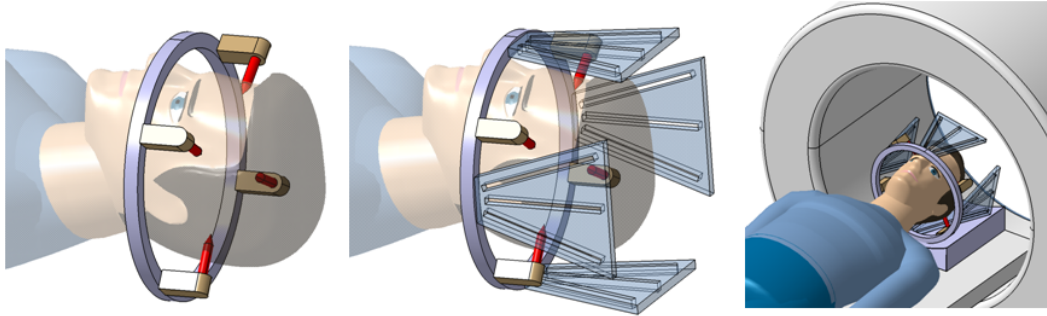
Figure 1.1: *Preoperative steps in the generic workflow for stereotactic neuro-surgery. Left: Stereotactic base unit (gray ring) is fixed to the patient's head with sharp tipped pins (red). Middle: Localizer is mounted to the base unit. Right: A 3D image of the patient's head with attached localizers is taken.*

- **Target- and trajectory-planning:** A surgical planning software is used to identify the target or targets on the 3D image. For each target, a corresponding entry point is defined. Based on these point pairs, the trajectories for the instruments are calculated by the software.

- **Calculation of stereotactic parameters:** The parameters for the stereotactic aiming device are calculated by the surgical planning software. The calculation is based on the planned trajectories and the relative position of the localizer.

- **Mounting of the stereotactic aiming device:** The stereotactic device is attached to the base unit (Figure 1.2, blue device). Its axes are adjusted according to the parameters calculated by the surgical planning software.

- **Trepanation:** A surgical drill is attached to the stereotactic aiming device. Next, the skull of the patient is opened and the dura mater is removed (Figure 1.2, left).

- **Probe insertion:** After removing the drill, the actual probe (electrode, biopsy tool, etc.) is mounted to the stereotactic aiming device (Figure 1.2, right). It is forwarded along the previously planned trajectory until the target is reached. The final position of the probe is validated using imaging technologies. Correct positioning assumed, the clinical purpose of the probe is fulfilled by either collecting a specimen, electronically stimulating the area or delivering drugs.
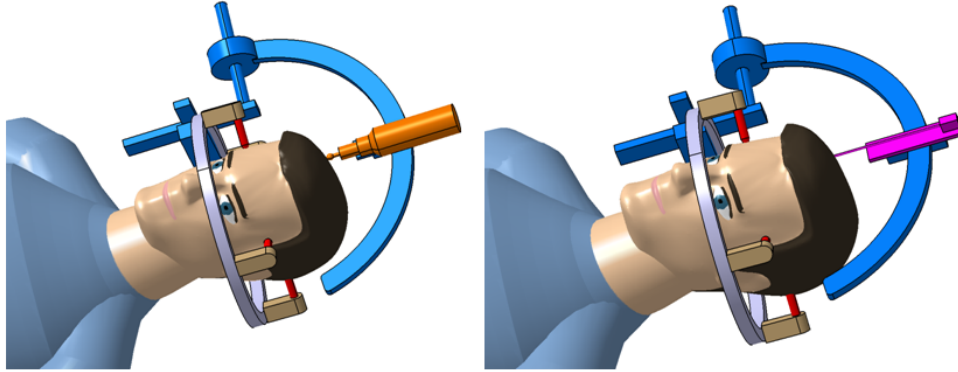
Figure 1.2: *Intra operative steps in the generic workflow for stereotactic neuro-surgery. Left: Trepanation of the patient's head with a surgical drill (orange). Right: Feeding of the probe (pink) into the brain.*

Some procedures differ in one or more points from the above described workflow. Most interventions, however, will follow the pattern and it therefore presents the fundament for further considerations and discussions.

1.2 Treatment of Parkinson's disease using Deep Brain Stimulation

Parkinson's disease (PD) is the second most common neurodegenerative disorder after Alzheimer's disease [5]. The prevalence of PD in industrial countries among the population of age 60 and older is 1% and above age 80 around 3% [6]. In Germany, there are currently about 250 000 PD patients [7].

The cause of the disease is thought to be the inexplicable degeneration of nerve cells in the pars compacta of the substantia nigra. The axons of the nerve cells in the substantia nigra project to the striatum with dopaminergic connections. However, with too little dopaminergic input to the striatum, the activity of the nerve cells of the thalamus is inhibited. Afferent information cannot pass through the striatum to the cortex. Most prominent symptoms, resulting from this inhibition are: Resting tremor, rigor, bradykinesia (a slowing of movement, resulting in a shuffling gait) and hypokinesia or even akinesia [8].

The treatment with L-Dopa, a precursor of dopamine, is the current clinical standard. However, after 3-7 years, effect reduction as well as side effects occur in 60% of all

patients [8]. Deep brain stimulation presents a therapeutic option for many of these patients with lack of symptom control under L-Dopa or severe side effects.

In a recent study, the costs for conventional therapy with L-Dopa and therapy using DBS were compared [9]: For conservative pharmacological treatment, the annual costs were estimated at 15 991 $\pm$2 636 €. If treated using DBS, the costs were 21 082 $\pm$1478 € in the year of the operation and 7 223 $\pm$717 € in the following years. As PD is a chronic disease with does not reduce the life span, a course of disease over many years is common. DBS presents an economic alternative that moreover significantly reduces the symptoms when compared to the L-Dopa control group.

The aim of the DBS surgery is to position a stimulating electrode in close proximity to one of several potential target regions. The two most prominent target areas are: The globus pallidus internus (GPi) and the subthalamus nucleus (STN) [10, 11, 12, 13]. Note that there is an ongoing debate on which target yields better post-operative results. Furthermore, new targets are investigated, e.g., ventral intermedius nucleus (Vim) [14] but the discussion of their properties is beyond the scope of this work.

Both STN and GPi are neither spherical nor cubic, hence their size cannot be described without errors. An estimation based on [15] for the STN and [16] for the GPi is given: The maximal extent of STN covers up to $5\times5\times5$ mm^3 and the GPi $8\times6\times5$ mm^3. There is an ongoing discussion, which area of the nuclei to target for best stimulation results, in [17] the optimal stimulation area for the STN was found to be close to its dorsal end.

In preparation of the intervention, a stereotactic base unit is fixed to the head of the anesthetized patient using sharp tipped pins or bone screws. After that, a localizer unit is mounted to the base unit and a 3D image is acquired using a computer tomograph (CT) or a magnetic resonance tomograph (MRT). Next, the image data is displayed in a surgical planning software.

Immediately before the actual surgery, the target points for the stimulation electrodes are identified on the acquired images using the surgical planning software. It is difficult to directly identify STN and GPi on the 3D images, hence an indirect targeting approach is chosen. Therefore, the anterior commisure (AC) and posterior commisure (PC) in the third ventricle, two well visible anatomical structures on the 3D image, are identified. They provide one axis of the base coordinate systems for the target point identification. Its origin equals the middle of the two commisures. One of the two remaining axes is defined by the patient's cranial-caudal axis. The last axis is perpendicular to the remaining two [1]. With the help of neuro anatomical atlases,

e.g. Schaltenbrand atlas [15] or Talairach & Tournoux atlas [16], the position of the target with respect to the AC-PC coordinate system is identified. To complete the trajectory planning, an entry point is specified by the surgeon to avoid any major blood vessels or the ventricles. Next, the surgical planning software calculates the required parameters for the stereotactic device.

After identifying the target point and the trajectory, the actual intervention starts. The stereotactic aiming device is mounted to the stereotactic base unit and its axes are set to the parameters determined by the planning software. The skull is opened using a surgical drill and the micro electrode is fed into the brain using a micro-drive unit (MDU). During this process the electric signals from the brain are recorded, amplified and displayed to the surgeon via loud speakers. These micro electrode recordings (MER) provide information about the brain area, which is currently penetrated by the electrode. To validate if the target position is reached, a test stimulation is performed and a control X-ray image is taken. Once the correct position is found, the electrode is removed and replaced by a permanent electrode. The trepanation is closed and the electrode is connected to a stimulator that is implanted under the patient's clavicle bone. The parameters for the stimulator can be adjusted wireless.

In case the correct target is not reached by the electrode, it has to be removed from the brain. Next, the stereotactic aiming device has to be readjusted before starting a second attempt. If a suboptimal target is reached, higher currents are required to achieve alleviation of symptoms. Neighboring, healthy brain areas can be stimulated and severe side effects can occur.

1.3 Brain tumor biopsy

Stereotactic tumor biopsy is the simplest of all stereotactic interventions [3]. It represents an ideal starting point for newly developed stereotaxy systems. A great variety of brain tumors exist, the most commons are Gliomas (50.3%), Meningiomas (20.9%), Pituitary adenomas (15%) and Nerve sheath tumors (8%) [18]. Approximately 1.5% of all cancer diseases are brain tumors [19].

In order to establish a diagnosis, the first method of choice are imaging tools, e.g., CT and MRT. Sometimes, however, there is a need for a histopathologic characterization of a tissue sample as some tumors cannot be characterized with the necessary certainty. There is evidence that over 10% of diagnoses based on histologies were unsuspected based on prior imaging [20]. Furthermore, biopsy tissue can be used for supplementary

information, e.g., molecular and genetic assays [21].

Since the 1960s, tumor biopsies are common [22, 23]. After the invention of the CT, biopsies were often based on individual 3D image data [24]. This development lead to a mayor increase in clinical applications of stereotactic interventions. In the 1980s, the use of biopsy has further increased and has become a neurosurgical standard procedure by today [25, 26].

In order to determine the type and grade of a tumor, it can be necessary to acquire one or more tissue samples [8]. Quite often, in metastatic tumors, one single specimen is enough to establish a diagnosis. In glial neoplasms it is best to provide multiple specimens from different regions in the tumor to the pathologist [3].

One of the most popular ways to obtain a tissue sample is the side window cannula originally described in [27]. It consists of an inner and an outer cannula. Both cannulas contain a 10 mm long side window at their distal end. Rotation of the inner cannula lines up the two windows or closes them. Once the stereotactic target is reached, a syringe is used to suck in the neighboring tissue. Next the inner cannula is rotated to cut the tissue. After that, the inner cannula is removed and the specimen is collected. The surgical procedure follows the above described pattern. A surgical planning software is used to identify the target area or areas on the 3D image. In contrast to DBS, the target area is well visible on the image data and there is no need for indirect targeting. The stereotactic aiming device is adjusted to the parameters determined by the software. Next, the skull is opened using a surgical drill. After that, the biopsy tool is fed into the brain using a micro-drive unit and once the target is reached, the specimen is collected. If required, the biopsy tool is reinserted and an additional sample is cut out.

Depending on type and stage of the tumor, the tumor volume and with it the stereotactic target can vary tremendously. Especially in small tumors, highly accurate targeting is required. Faulty positioning of the biopsy tool can lead to false diagnoses.

1.4 Structure

The work is organized as follows: This chapter contained an introduction to the clinical background of stereotaxy. A generic workflow for stereotactic neurosurgery was explained. Two exemplary clinical applications, DBS and the collection of a tumor biopsy, were described.

In the second chapter, the spatial orientation in stereotaxy is briefly explained. The chapter contains information about existing systems and related work in the field of stereotactic neurosurgery. Both manual and robotic systems are presented and their properties are discussed. To conclude, means to intracranially localize a surgical probe are discussed. The state of the art is presented and a promising new localization method is presented.

The requirements for a new hybrid stereotactic neurosurgery robot are discussed in the third chapter. The limitations and drawbacks of previous surgical robots are analyzed using the example of the ROBODOC. Next, general, hardware and software requirements for a medical robot are covered.

The fourth chapter describes the development of the **M**otor **A**ssisted **R**obotic **S**tereotaxy system, short **MARS**. To begin, the design is covered. Next, the hardware used in the MARS is described. After that, the control of the robot is explained. The describtion of the kinematics follows. Then, the calibration of the MARS is presented. To conclude, the operating modes of the hybrid robotic system are covered. The MARS presents the major contribution of this work to the field of neurosurgical robotics.

In Chapter 5, a novel intracranial probe localization technique based on static magnetic fields is presented. Its application in the context of stereotactic neurosurgery is discussed and the algorithms involved are explained. Next, the design and setup of the hardware is covered. Then, the integration of the magnetic probe localization into the MARS is explained.

The experimental applications of the MARS are discussed in Chapter 6. To start, the standard robotic parameters 'absolute accuracy' and 'repeatability' are measured. Next, the electromagnetic compatibility of the MARS with equipment in the operating theater is analyzed. After that, the application accuracy of the MARS is studied. After successful testing, the MARS is clinically evaluated in a tumor biopsy. To conclude, the results from the experiments with the magnetic probe localization are presented.

The seventh chapter critically reviews the achieved results. The properties of the design, hardware and software are analyzed and compared to the requirements specified in Chapter 3. Furthermore, the results from the experimental application are compared to other robotic and manual stereotaxy systems. Possible applications for the magnetic probe localization are discussed.

To conclude, a summary of the thesis and an outlook to future challenges is given in the eighths chapter.

2 Related work

Existing solutions for stereotactic neurosurgery will be presented and discussed in this chapter. The focus of this introduction to related work lies on stereotactic neurosurgery. This excludes systems that were solemnly designed for other purposes, e.g. tumor resection, as this would go beyond the scope of the work.

Stereotactic positioning systems can be grouped into two types: **Manual stereotactic frames** and **robotic systems**. A brief overview over current systems with selected examples from both groups will be given in this chapter. Further information about the systems can be found in the corresponding literature mentioned in the text.

As the spatial orientation is of great importance to reach a previously defined target, this chapter starts with an introduction to the coordinate systems involved in stereotactic neurosurgery. Their mutual relation is explained in detail.

Note that a great variety of systems exist and that this work cannot deliver a complete discussion. Furthermore, other solutions for neurosurgical interventions that show some overlap with stereotactic neurosurgery, e.g., navigated surgery [28, 29, 30], are excluded from the overview.

The chapter concludes with a 'strengths and weaknesses' analysis of the various systems and a transition to the requirements for a newly developed stereotaxy robot.

2.1 Spatial orientation in stereotaxy

For stereotactic neurosurgery, it is of utmost importance to reach a previously planned pose inside the human brain. As many different coordinate systems (CoS) are involved, the definition of a target pose can be confusing at a first glance. For this reason, a short overview over the involved coordinate systems is given. The knowledge of their mutual relation is referred to as registration. An overview over existing registration techniques is given in [31]. To conclude the section, a step-by-step instruction on how the required parameters for the stereotactic aiming device are derived from the determined target position is provided. The involved coordinate systems are:

- **Patient CoS:** For targets not well visible on the 3D image, e.g. STN, the target pose in the brain is specified with respect to natural landmarks. In clinical practice, the anterior commisure (AC) and posterior commisure (PC) in the third ventricle are most commonly used [1]. The middle between AC and PC defines the origin for this coordinate system. The AC-PC line defines one axis. Another axis is given by the caudal-cranial axis of the skull. The last axis is perpendicular to the other two and they form a right-hand coordinate system (see Figure 2.1, left).

- **Stereotactic device CoS:** The coordinate system is defined with respect to the base unit of the stereotactic device. This base unit is rigidly fixed to the patient's skull (see Section 1.1). The origin of the coordinate system varies between the devices of different manufacturers. The pose of the stereotactic tool can be calculated based on the settings of the axes (forward kinematics). Also, the required axes parameters to reach a target pose can be determined (inverse kinematics).

- **Imaging CoS:** To specify the target in the brain, a 3D image of the head is acquired. The coordinate system of the imaging data is dependend on the used system and the position of a voxel is given with respect to the origin of this coordinate system. To determine the transition between imaging CoS and stereotactic device CoS, a localizer unit is required.

- **Robot CoS:** The base coordinate system of a robot usually matches a well defined position in the stand of the robot. As with stereotactic devices, it can vary between different manufacturers and models. The pose of the tool can be derived from the positions of the joints of the robot (forward kinematics). Similar to stereotactic devices, the required joint positions can be derived from the target pose (inverse kinematics).

From a surgeon's point of view, the spatial orientation task can be simplified as follows: *Which settings for the stereotactic device are required in order to reach the position that I have identified on the 3D image as target?*

A step-by-step answer to this question is given in the following. Before the 3D imaging, a localizer unit is fixed to the stereotactic base unit (see Section 1.1), then the image data is acquired. Next, the transformation between the CoS of the stereotactic base unit and the CoS of the imaging modality is calculated. The localizer features 'N','V'
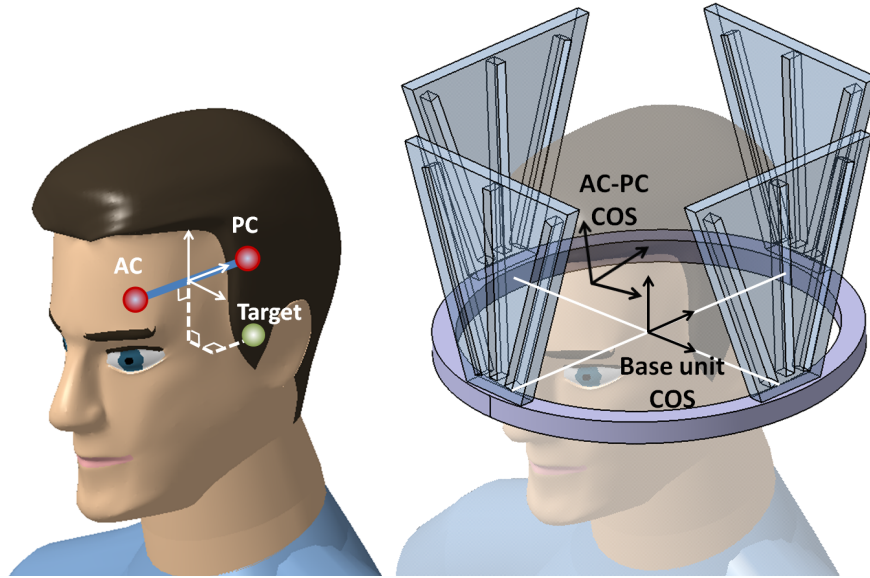
Figure 2.1: *Left: The anterior commissure (AC) and posterior commisure (PC) are two clearly recognisable landmarks in the human brain. Based on them, the AC-PC coordinate system is defined. Right: The stereotactic base unit coordinate system is defined by the manufacturer.*

or 'Z' like structures with known shape and dimensions that are well visible in the 3D image data. In the surgical planning software, these structures are identified on the image. Based on this, the transformation is determined.

In the next step, the image data is displayed to the surgeon. Depending on the intervention, the surgeon can either directly identify the target, e.g. in tumor biopsy, or he has to identify anatomical landmarks on the 3D image, e.g. for DBS. In the latter approach, the AC-PC coordinate system is defined, as previously described. As the definition of the AC-PC CoS is based on the imaging CoS, the transition between these two is apparent. Figure 2.1, right, shows the two described coordinate systems. The surgeon then identifies the target point in the image with respect to the AC-PC CoS. After the target identification, a trajectory to reach the target is required. For this purpose, a second point, the so-called *entry point* is selected by the surgeon.

In both, direct and indirect identification of the target, the required transformations between the involved coordinate systems are known. The surgical planning software transforms the coordinates of the target point identified on the image to the CoS of the stereotactic base unit. The rotational part of the target pose is defined by the angles between the target and entry point. Based on the target pose, the surgical

planning software calculates the required parameters for the stereotactic device (inverse kinematics).

For robotic neurosurgery, another coordinate system has to be considered: The transition between the CoS of the robot and the CoS of the stereotactic base unit has to be known in order to correctly position the probe. In contrast to stereotactic aiming devices, the robot cannot be directly connected to the patient's head. There is hence an offset between the coordinate systems of the robot and the stereotactic base unit. Just like the stereotactic aiming device, the forward and inverse kinematics of the robot need to be known in order to find the right parameters for the axes of the robot. This will be discussed later on in Section 4.4.

2.2 Manual stereotactic frames

The Russian anatomist Zernov performed the first stereotactic surgeries in 1889 with the aim to measure and map the human cerebral gyri [32]. In the early 20th century, stereotactic devices were used in animal studies [33]. Spiegel and Wycis [34] performed the first stereotactic intervention of the modern era in 1947. Since then, a great variety of mechanisms for stereotactic neurosurgery has been introduced [1, 35, 36].

There are three basic kinematic setups for manual stereotactic frames: Translational (e.g. [34, 37, 38]), center of arc (e.g. [39, 40, 41]) and burr hole mounted (e.g. [42, 43, 44]). The properties of each design will be explained by means of one representative example per group. Table 2.1 gives an overview of systems with their introduction date and their kinematic chain. Note that there is a great variety of devices and that the table only represents a fraction of the developed devices.

Most manual stereotactic frames are made of sterilizable metal, hence no sterile covers are required during surgery. Furthermore, manual frames can easily be transported between different operating theaters (OT). Their spacial demand is very limited, so they can easily be stored away when not used. All these features foster the acceptance among neurosurgeons.

The registration between patient and imaging coordinate system in manual systems is achieved by using localizer units. They are either attached to the stereotactic base unit or incorporated.

Table 2.1: *Overview over manual stereotactic devices categorized by kinematic principle with their introduction date and their trade name*

Device name	Kinematics	Introduction
Spiegel & Wycis	Translational	1947 [34]
Riechert-Mundinger	Translational	1955 [37]
Talairach	Translational	1958 [38]
Leksell	Center of arc	1949 [39]
Cosman-Robert-Wells	Center or arc	1991 [40]
Zamoranow-Duchovny	Center of arc	1994 [41]
Austin & Lee	Burr hole mounted	1956 [42]
Pelorus	Burr hole mounted	1985 [43]
Nexframe	Burr hole mounted	2004 [44]

2.2.1 Translational: The Riechert-Mundiger system

Translational systems were the first devices used for stereotactic interventions, e.g., by Spiegel and Wycis in 1947 [34]. Their name originates from the idea that each target point is defined by three mutually perpendicular translational coordinates.

One limitation of the early devices was, that only one trajectory would lead to a target point. If this trajectory would cross vital brain areas, the surgery could not be performed. In newer translational system, rotational axes were incorporated.

The Riechert-Mundinger (RM) system, depicted on the left side of Figure 2.2, presents a translational device with additional rotational axes. It was developed in the early 1950s [45, 37]. Thanks to continuous modifications and adaptations, the RM system has maintained its place in stereotactic neurosurgery [46].

The system uses a circular base unit which is fixed to the patient's head with sharp tipped pins. Four fiducial plates can be mounted to the base ring to register the ring in a CT or MRT image. The RM aiming bow is fixed along three points which equips the system with high stability and accuracy.

The mathematics involved in the target planning are complex, as translations and rotations are not decoupled from each other. Before computers were introduced into the OT, a target point simulator was used to determine the exact trajectory.

Commonly, the base unit is fixed to the patient's head. Next, the localizer is attached and a 3D image is acquired. The surgeon identifies the target and trajectory on the 3D image in the surgical planning software. Afterwards, the software calculates
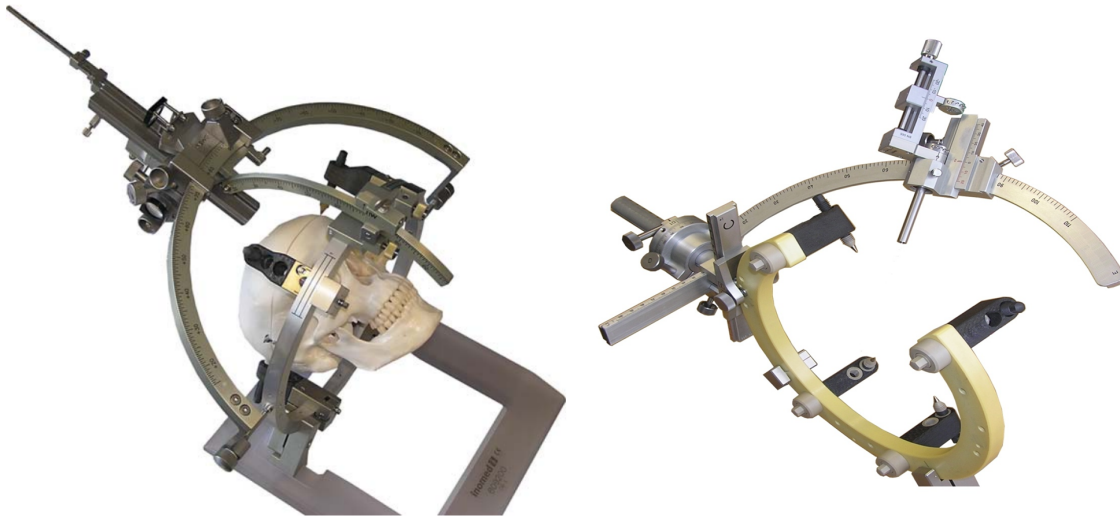
Figure 2.2: *Left: Riechert-Mundiger system, the aiming bow is fixed at three points. Right: Zamaranow-Duchovny system; the aiming bow is fixed on one side only. Images courtesy of inomed Medizintechnik GmbH.*

the parameters for the stereotactic frame. The simulator is set to the previously determined target position. The surgeon adjusts the axes of the frame to the calculated position and validates the settings using the target point simulator. He can now vary the settings until the tip of the probe matches the target point.

One advantage of this approach is, that slight deviations, e.g., caused by bending of the probe, are detected. Figure 2.2, left side, shows a RM aiming device attached to its circular base unit.

2.2.2 Center of arc: The Zamaranow-Duchovny system

Lars Leksell introduced the first center of arc–also referred to as arc-quadrant or iso-center–system in 1949 [39]. The system consists of a semi-circular arc with a movable carriage. The center of the arc corresponds to the determined target position. Figure 2.3 visualizes this idea: When ring and/or arc angle are altered, the probe tip remains in the same position, as it is in the center of the sphere. This property allows for an easy and intuitive target adjustment of the stereotactic frame. Translational and rotational part of the pose are decoupled.

The Zamoranow-Duchovny (ZD) system, developed in 1994 [41], is a commonly used representative of center of arc systems. Its circular base ring is fixed to the patient's
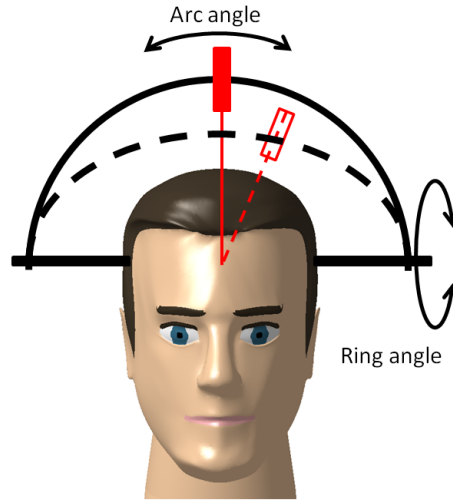
Figure 2.3: *Definition of the stereotactic angles after [39]. Two positions are over-laid: The initial position of the frame and with dotted lines a position after rotating about both axes. Note that the tool tip remains on the same translational position.*

head with four sharp tipped pins. An open serial kinematic chain with three translational and two rotational axes is used in the ZD frame. It features one additional translational axis to feed the probe into the brain. The three translational axes in the base of the system are mutually perpendicular. They are used to position the probe in the Cartesian space. The rotational part of the pose is adjusted by the two rotational axes. Figure 2.2, right, shows the ZD frame mounted to a ceramic base ring.

The surgical procedure resembles the procedure described for the RM system. As in the RM system, the frame is fixed to the head of the patient, the localizer is mounted to the base unit. Next, a 3D image is acquired and the trajectory is defined in the surgical planning software. After these common steps the procedure differs from the one used in the RM system. Here, no target point simulator is used. Thanks to the decoupling of translational and rotational part of the pose, the surgeon can fine adjust the rotational axes without the need of re-adjusting the translational axes.

2.2.3 Burr hole mount: The Nexframe system

Since the beginning of stereotaxy, many burr hole mounted systems were introduced, e.g. by G. Austin in 1956 [42]. Although these systems formerly lacked accuracy [47, 48], they are currently enjoying a renaissance [49, 50]. This is mainly due to

the incorporation of navigation systems in neurosurgery which greatly enhances the accuracy [51]. There is an ongoing discussion whether the accuracy of these navigated burr hole mounted devices is at the same level as frame based systems [2].

In burr hole mounted systems, a base unit or the device itself is directly fixed to the skull of the patient with screws. The location of the burr hole is chosen such, that the target is located perpendicular to the skull surface. The selection of the location is of great importance, as burr hole mounted devices can only compensate for small misalignments.

The Nexframe (Medtronic Inc., USA), presents a commonly used burr hole mounted system [52]. It consists of two parts: Nexframe base, which is fixed to the patient's head with two screws and Nexframe tower which is attached to the base unit. Before the trepanation, a 3D image of the patient's head is taken. Fiducials, visible on the 3D image, are incorporated in the base unit to determine the registration. The target and trajectory of the probe are calculated by the surgical planning software with respect to the coordinate system defined by the fiducials. The tower and the base unit incorporate a marker for an optical tracking system. Arbitrary alignment of the tower to the base unit is possible. The desired position is displayed by the surgical planning software. Next, the tower is manually manipulated by the surgeon, until the desired position is reached. Then, the tower is locked to the base unit.

Due to the alignment with the preoperative planning, the operating time is longer [53]. Furthermore, it is highly dependent on the accuracy of the tracking system.

2.2.4 Discussion

The properties of the three functional principles are briefly discussed in the following. The target planning and intraopertive adjustment of the trajectory is cumbersome for the translational systems. Furthermore, a target simulator is required to determine the axes' parameters. As the rotational and translational part of the pose are not decoupled, the targeting is not intuitive.

Center of the arc systems feature an intuitive and easy adjustment of the axes. Intraoperative changes in the rotational axes do not have any effect on the translational part of the target position. A target simulator is not required to adjust the axes. However, their mechanical design is complex compared to translational and burr hole mounted devices.

Assuming high accuracy requirement, burr hole mounted devices need an external

Table 2.2: *Advantages and drawbacks of the three kinematic principles used in manual stereotactic frames*

Kinematic	Advantage	Draw back
Translational		
	+ mechanically simple	- complex calculations
		- unintuitive targeting
Center of arc		
	+ simple calculations	- mechanically complex
	+ unlimited number	
	of target trajectories	
Burr hole mount		
	+ mechanically simple	- tracking device needed
	+ less invasive	- time consuming setup

tracking system to correctly align the aiming device to the base unit. This process is time consuming and introduces new error sources into the work flow. Burr hole mounted devices are mechanically simpler than center of arc and translational systems. Table 2.2 summarizes the properties of the three functional principles. The results of this analysis are an important aid to describe the requirements for a stereotactic robotic system later in this work.

2.3 Robotic stereotactic neurosurgery

Since the late 1980's several neurosurgical robots have been described [54, 55, 56]. This makes neurosurgery one of the earliest applications for robotic surgery [57]. An overview over the development can be found in [58]. Stereotactic neurosurgery provides ideal conditions for the application of robotic aids for the following reasons:

- **Limited movement of the target:** Robotic surgery is most successful when the motion of the target is limited. Compared to soft tissue, e.g. liver, the skull limits the target movement during surgery.

- **Rigid fixation of the skull:** In stereotactic neurosurgery, a base unit is fixed to the head of the patient. This rigid connection can be used to determine the

transformation between the coordinate system of the robot and the patient's coordinate system.

- **High accuracy required:** Small deviations from the planned trajectory can lead to significant brain damage, especially in eloquent brain areas [59]. Hence, high accuracy is of utmost importance in stereotactic neurosurgery.

Most neurosurgical robots are developed in research facilities and universities and are not commercially available. However, a few FDA/CE approved robotic systems exist. Some prominent and innovative examples of newly developed neurosurgical robots will be given in the following.

2.3.1 neuromate

One of the first robotic systems–and still on the market today–is the neuromate system, introduced in 1987 [60]. The neuromate consists of an industrial robot with five rotational axes and provides five degrees of freedom (DOF). The robot itself is mounted to a triangular housing which contains the power electronics for the system. At the lower end of the housing, an arm extends. The arm is used to rigidly fix the skull of the patient with a Mayfield clamp or to interface with a stereotactic base unit. Figure 2.4 shows the system; on the left, the latest version designed by Renishaw (Renishaw PLC, UK), the current owner of the neuromate technology, is pictured. The phantom skull is fixed to the arm of the robot with a Mayfield clamp. On the right, an older version of the neuromate is depicted. Next to the robot itself the control unit can be seen in the background of the picture. Sterility of the system is achieved by draping the robotic arm. The tool holder at the end-effector of the robot is sterilizable.

Two operating modes exist, frame-based and frame-less: In the frame-based mode, the stereotactic base unit is fixed to the patient's head. A localizer unit is attached to the base unit. After 3D imaging of the patient's head, the surgeon defines the target and the trajectory of the robot in a surgical planning software. Next, the base unit is fixed to the robot. Therefore, the interface at the end of the arm of the robotic system is used. No further registration steps are necessary, as the transformation between the end effector and the fixation of the base unit is known. The robot is then moved according to the preoperatively planned trajectory.

In the frame-less mode, a base unit for an ultrasound (US) localizer is fixed to the patient's skull with screws. After that, the 3D image is acquired and the trajectory is

Figure 2.4: *The CE/FDA approved neuromate system by Renishaw PLC, UK; Left: Currently distributed robot with phantom head attached to the head clamp. Right: previous version of the neuromate system with control unit in the background. Images courtesy of Renishaw GmbH.*

planned as in the frame-based mode. The skull is fixed to the end of the arm using the Mayfield clamp. To register the patient's coordinate system to the coordinate system of the robot, a US marker is attached to the base unit which is fixed to the patient's skull. After that, the tracking device for the US marker is mounted to the end-effector. The robot is manually moved in close proximity to the US marker. Next, the robot automatically approaches a number of positions. At each position, the current position of the US marker with respect to the US tracking device is saved along with the coordinates of the robot. Based on the recorded data, the transformation between robot and patient coordinate frame is calculated.

The application accuracy for both modes was measured in [61]. The authors found a mean error of 0.86 mm with a standard deviation of 0.32 mm for the frame-based mode. The frame-less mode showed a mean error of 1.95 mm with a standard deviation of 0.44 mm. The following CT parameter were used: Slice distance 2 mm, in-plane distance 1.18 mm x 1.18 mm.

The mobility of the system is limited, as it does not provide a mobile stand. Furthermore, the spacial demand in the OT is very high when compared to manual systems. In the frame-less mode, a tracking system is required to determine the transition between

the coordinate systems of the robot and the patient.

2.3.2 PathFinder

The PathFinder (Prosugics, UK) was first reported on in 2001 [62]. It is based on an industrial robot that is mounted to a mobile stand. The stand houses the power electronics of the robot. Figure 2.5 shows two pictures of the PathFinder system. On the left side, a close up of the robot is displayed, on the right the robot with its control station can be seen. As most industrial robots, the PathFinder robot has six degrees of freedom. The end-effector is equipped with a tool holder that accepts different tools for specific tasks. An optical tracking system can be attached to the end-effector. It is used to register the coordinate systems of the robot and the patient. A sterile cover insulates the robotic arm from the patient.

In the standard surgical procedure of the PathFinder, the following steps are executed: First, fiducials are fixed to the head of the patient. They are either screwed in the skull or attached to the skin with adhesive tape. Next, a 3D image of the patient with fiducials is acquired. After that, a surgeon plans the target and trajectory of the robot with a surgical planning software based on slice images from the 3D scan. In the next step, the robot is positioned in proximity to the patient. The patient's head is fixed to the operating table with a Mayfield head clamp. The optical tracking system determines the position of the fiducials from various angles. Based on this information, the transition between the stereotactic coordinate system and the robotic coordinate system is derived. The robot is automatically positioned according to the preoperative plan. The various surgical tools are attached to the tool holder and the surgery is executed by the robot.

In a phantom trial the following parameters for the application accuracy were found: mean norm error 2.7 mm, minimal error 1.8 mm, maximal error 3.2 mm. The parameters for the CT scanner were slice thickness: 2 mm, in-plate voxel distance: 0.7 mm in X and Y [63].

The footprint in the OT is much smaller when compared to the neuromate system, but still several orders of magnitude bigger than the demand of manual systems. Thanks to its mobile stand, PathFinder can be transported between different OTs. An optical tracking system is required to operate the system.
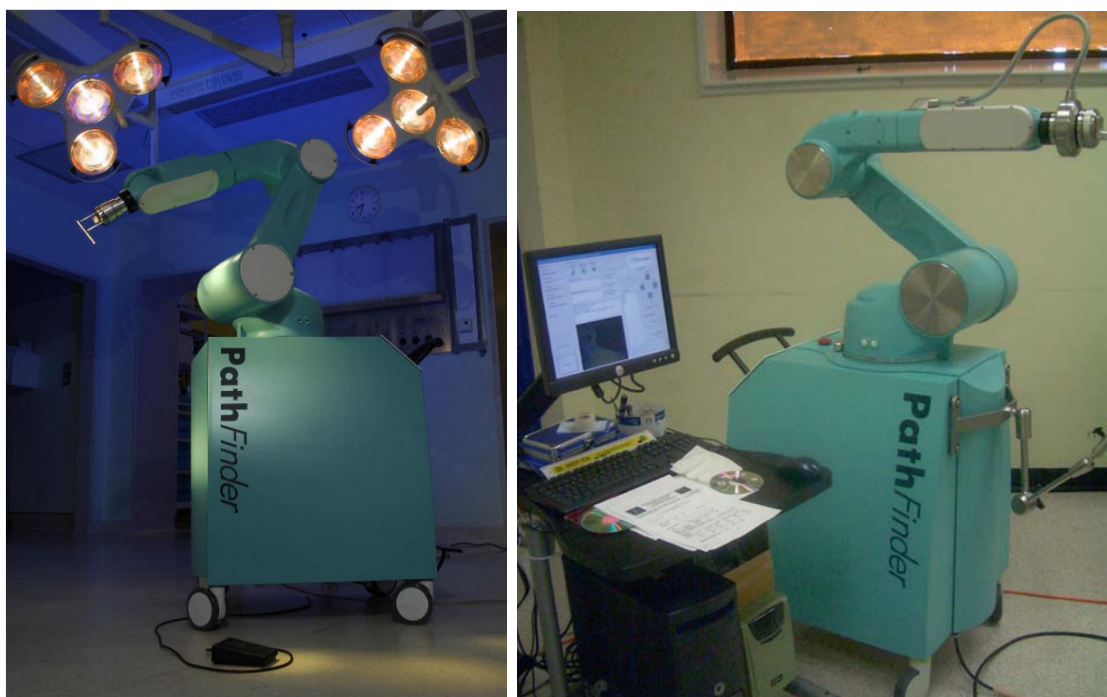
Figure 2.5: *The PathFinder (Prosugics, UK) neurosurgery robot. Left: Close-up of the robot with its stand (image from [63]). Right: Robot with surgical planning and control station (image from [59]). Images courtesy of the publishers.*
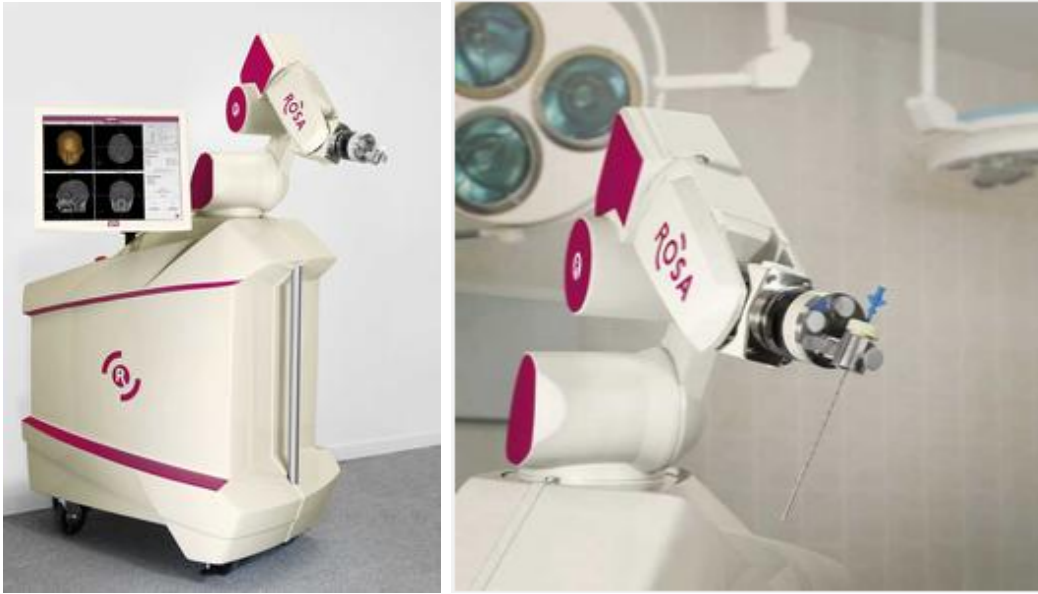
Figure 2.6: *ROSA neurosurgery robot (Medtech S.A.S., France). Left: Robot with user console; Right: close up on the tool holder of the robotic system. Images courtesy of Medtech S.A.S.*

2.3.3 ROSA

The ROSA robot, designed and distributed by Medtech S.A.S, Montpellier France, presents the latest CE (May 2008) and FDA (November 2009) approved robotic aid for neurosurgery [64]. The ROSA is a six degree of freedom industrial robot mounted to a mobile stand. Its design resembles the design of the PathFinder system. The stand houses the power-electronics and the control computer of the robot. Figure 2.6 shows the ROSA system. The left side depicts the system with the robot mounted to the stand, and the display for interaction with the user. On the right, a close up of the tool holder and the robot is shown. Note that the system is only designed to position probes in space and not to interact with the patient. The insertion of tools or other interaction with the patient lies within the responsibility of the surgeon.

The surgical procedure with the ROSA proceeds as follows: A 3D image of the patient is acquired and the trajectory of the probe is planned based on this data. The skull of the patient is fixed to the operating table using a clamp. Next, the robot is positioned in close proximity to the patient and fixed to the operating table. The breaks of the mobile unit are activated to further minimize undesired movement. The registration is achieved using a laser scanner. The scanner is attached to the end-effector of the

robot. It determines the distance to the patient's head and thereby acquires a 3D surface representation. This 3D data is registered to the preoperative image of the patient's head. No fiducials or frames are required to obtain the registration. Sterility is achieved by draping the robot. The tool holder at the end-effector is sterilizable.

The robot is equipped with a force-torque sensor attached to the end-effector. In the so-called haptic collaboration mode, the surgeon can move the robot by pulling and pushing the end-effector. Here, the robot only moves along the previously defined trajectory. This way, the surgeon can vary the distance to the patient's head intuitively. In 2011, twelve units are in clinical use [64]. So far, no studies about the application accuracy of the system are published.

The footprint of the system is smaller than the footprint of the PathFinder system which also enhances the mobility of the robot. Thanks to the haptic collaboration mode, an additional safety feature is provided. The system requires a laser scanner to determine the registration. This can introduce additional errors to the overall accuracy.

2.3.4 Nagoya Institute of Technology neurosurgery robot

In the work of Jumpei Arata [65, 66] a completely different approach is chosen compared to previously presented systems. Instead of using an industrial robot, a custom designed parallel robot is developed. The robot can be mounted to a modified stereotactic base unit (see Figure 2.7, left). The system provides a total of 8 DOF, of which 4 are active and 4 are passive.

The robot was designed for brain tumor removal surgery. It presents the slave side of a telemanipulation system that is controlled by the surgeon via a master console. Various sensors and tools are incorporated in the robot: A 3D endoscope, a light guide, a suction tool and a surgical tool manipulator. Furthermore, an irrigation system and a volume control mechanism for the suction tool are provided. A control PC processes the commands from the user and the information from the slave side.

The surgical procedure with this robot differs from the other manual and robotic systems described in this chapter. This is due to the purpose of the robot: It is designed to remove residual tumor from the brain. Currently, no operating mode for stereotactic neurosurgery is provided but the capabilities are clearly visible.

The weight of the robot (3 kg) as well as occurring torques need to be supported. Therefore, a rigid connection to both, the operating table and the head of the patient, is required. There is a risk of faulty positioning of the robot, as there are four passive
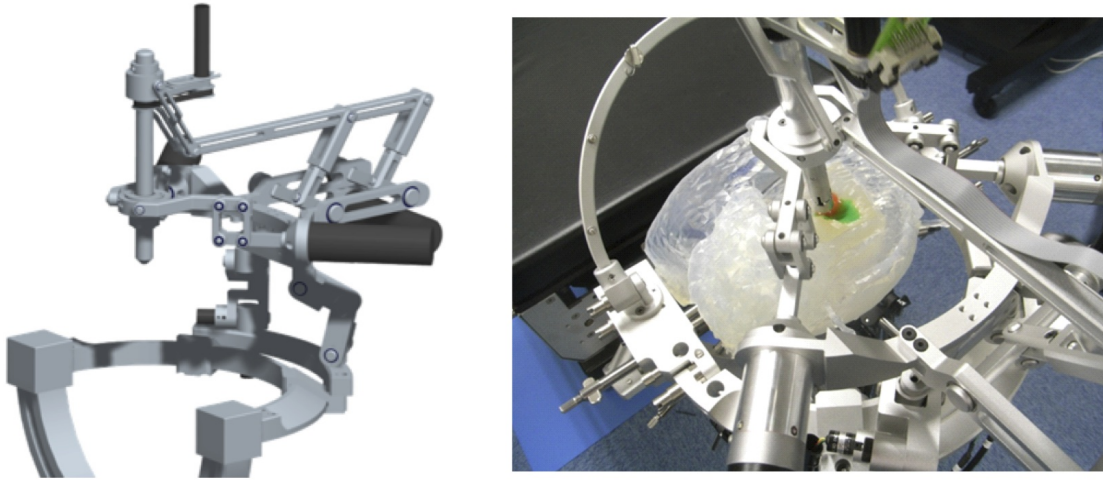
Figure 2.7: *Nagoya Institute of Technology neurosurgery robot. Left: CAD draft of the robot. It is mounted directly to a stereotactic base unit. It features a parallel kinematic chain with 4 DOF. Right: Actual robotic system with a phantom. Images courtesy of Prof. Jumpei Arata.*

DOF. Their position needs to be monitored carefully.

The parallel kinematic of the robot provides higher accuracy and stability compared to serial kinematic chains. One drawback is the limited work space [67]. Here, the passive part has a motion range of 45 *mm* × 30 *mm* × 30 *mm* (XYZ). The active part shows a lentiform motion range with a maximal diameter of 78 *mm* in the XY plane and a maximal movement in Z-direction of 45 *mm*. The mechanical accuracy is very high with a mean error of 0.04 *mm*. Two advantages of the system are its small footprint and its high mobility. As the system is not in clinical use, no information about sterilization or application accuracy is available.

2.4 Properties of stereotactic positioning aids

Table 2.3 summarizes the properties of the described manual and robotic systems. Some of the categories of the table are hard to quantify, e.g. 'Acceptance', others can easily be measured, e.g. 'Footprint'. Criteria like 'Acceptance' or 'Handling' were evaluated in close collaboration with the clinical and industrial partners. They represent the expert opinion of the team involved in the development of the new robotic system for stereotactic neurosurgery.

Please note that the criteria in Table 2.3 can be interdependent. The first two columns

of the table indicate whether a robotic or a manual system is analyzed. The column 'Handling' describes, how much effort is needed to set up the system and how intuitive this can be done. With 'Footprint', the spacial demand of the system in the OT is quantified. 'Additional Devices' indicates if the system requires external hardware, e.g. a tracking device, in order to work. 'Safety features' are features provided by the system that reduce the chance of faulty handling and positioning. The column 'Acceptance' depicts the acceptance of the respective device in the neurosurgical community. 'Mobility' indicates, if the system can be transported between different OTs and how much effort this requires. The 'Application accuracy' represents a standard benchmark for stereotactic devices. It indicates their accuracy under operating conditions. There is no standardized protocol on which hardware to use, but all experiments to determine the application accuracy of a system involve the following steps:

The application accuracy of a device is determined in phantom trials. A head phantom is equipped with target points. Next, the stereotactic base unit is fixed to the phantom and the localizer is attached to it. Then, a 3D image of the phantom is acquired. A surgical planning software is used to determine the stereotactic coordinates of the target points and the corresponding settings for the axes. Thereafter the aiming device is adjusted to these settings and the deviation between the tip of the probe and the target point is measured. Errors resulting from the imaging modality and resolution, the surgical planning software and mechanical inaccuracies of the system are considered in this benchmark. Note that patient specific error sources, e.g., brain shift, are not considered here.

Table 2.3 illustrates the advantages of manual systems: Their easy handling, their small footprint and their high mobility. This leads to high acceptance of manual systems in the neurosurgical community. Furthermore, their accuracy is still gold standard today. One drawback are the missing safety features: Misalignment of the axes are not detected.

Robotic devices, on the other hand provide high accuracy and integrated safety features. However they are not widely accepted in the neurosurgical community due to their limited mobility and their complex handling. They need additional devices to determine the registration which can prolong operating time. Furthermore, additional error sources are introduced.

Each system has its advantages and drawbacks. For the neurosurgical community, accuracy presents one of the most important criteria for a stereotactic device.

From the given application accuracies of systems in their frame-less mode (neuromate

Table 2.3: *Properties of the presented manual and robotic devices; '+' and '++' signs indicates an advantage, '-' and '- -' indicate a drawback for a system in the given category. A '0' indicates neutrality and a '?' that no data was available.*

Device Name	Robotic	Manual	Handling	Footprint	Additional devices	Safety features	Acceptance	Mobility	Application accuracy
Zamaranow-Duchovny		●	++	++	no	- -	+	++	+
Riechert-Mundinger		●	+	+	no	- -	++	++	++
Nexframe		●	++	+	yes	-	+	+	+
PathFinder	●		-	-	yes	+	0	0	+
Rosa	●		0	0	yes	++	0	0	?
neuromate	●		- -	- -	yes	+	0	-	+
Nagoya system	●		+	+	no	-	+	++	?

and PathFinder), one can conclude that the use of frame-less technology, e.g., US tracking system, does not result in higher accuracy. The highest accuracy is reached with frame-based methods and a rigid connection between the base unit and the targeting device.

The results of this section provide the fundament of the discussion concerning the requirements for a new robotic system in the next chapter. The goal is to combine the benefits of robotic and manual systems while avoiding their limitations.

2.5 Probe localization

First, a short motivation for the application of intra-cranial probe localization is given. After that, the state of the art is discussed. Second, the electro-magnetic probe localization and its properties are addressed. After that, the localization based on static magnetic fields is covered, as its application in a stereotactic context seems promising.

2.5.1 Motivation

In stereotactic neurosurgery it is crucial to position probes and electrodes exactly at the previously defined target location (see Chapter 1). One important step to achieve this goal is the use of highly accurate positioning aids (see Section 2.2 and Section 2.3).

However, as intra-operative error sources exist, faulty positioning can occur. The two most prominent error sources are:

- **Brain shift:** Brain swelling, celebrospinal-fluid (CSF) drainage, as well as the influence of gravitational forces all result in an intra operative deformation known as brain shift [68]. The displacement at the surface of the brain was analyzed in [69]. A mean error of 10 mm with the predominant directional component aligned with gravity was found. For stereotaxy the shift of the target depends on the intervention, e.g. for electrode implantation the average shift was 2.9 mm [70].

- **Probe-tissue interaction:** When the probe is forwarded into the tissue, interaction forces occur [71]. These forces can cause a deviation from the previously planned path. They originate from various sources, e.g. tissue inhomogeneity, organ deformation, respiration and flow of fluids [72].

Both error sources can result in missing the target inside the brain. Faulty diagnosis, e.g. in tumor biopsies, or the need to reposition an electrode e.g. in DBS, are the consequences.

The exact knowledge of the position of the probe also helps to evaluate new therapies, e.g. the targeting of new nuclei in DBS. The therapeutic effect can be evaluated with higher certainty, when the exact position of the probe is known.

For accurate targeting, it is beneficial to intraoperatively monitor the position of the probe. High spatial and temporal resolution is desirable. Furthermore, the burden of the patient should be as low as possible. Currently, four probe localization methods are in regular clinical use:

- **X-Ray:** The use of C-arms or other X-ray sources is the most commonly used technique to intraoperatively determine the position of a probe. The c-arm is aligned with the area of interest in the patient's brain. In order to validate the correct alignment of the probe, at least two 2D images are required. Even though the image acquisition itself does not require a lot of time, it is challenging and time consuming to determine the 3D position of an object based on two 2D projections. Furthermore, soft tissue is not well visible on X-ray images, hence it can be difficult for the surgeon to validate a probe position. Apart from that the exposure to ionizing radiation can harm the patient.

- **CT:** Some of the limitations of 2D X-ray images can be overcome by using intra operative CT imaging. This, however, is not available in all OTs and the applied radiation dose is higher. As with X-ray, soft-tissue is not well visible. The image acquisition requires more time than for conventional X-ray but is still very quick. The alignment of the patient with the CT, however requires more effort when compared to X-ray.

- **MRT:** The use of a MRT to validate the position of an implant is especially beneficial if the target planning is based on an MRT image [1]. No ionizing radiation is required to acquire an image. However, not all OTs are equipped with MRTs and the acquisition of an MRT image requires more time than a CT scan [73]. In the context of stereotactic neurosurgery the forces exerted by the MRT on ferromagnetic objects, e.g. head rings, need to be considered. They present an enormous danger to the patient.

- **Electromagnetic tracking:** Electromagnetic tracking presents the latest development in intra operative probe monitoring. An electro-magnetic field generator produces an alternating field. Based on the measured field at the probe, the location of the probe is determined. Real-time position monitoring with 6 DOF is feasible. No harming radiation is required. Furthermore neurosurgical instruments can be equipped with electromagnetic probes.

MRT, CT and x-ray can be used to validate the final position of a probe. However, they are not suitable for continuous monitoring of a probe for the following reasons:
The temporal and spacial resolution achievable with x-ray and CT images is very high. But both methods are not suitable as they use ionizing radiation.
In MR, the acquisition time is too long for continuous monitoring.
This leaves the electromagnetic tracking as the promising method for the intra-cranial probe monitoring.

2.5.2 Electromagnetic tracking

An electromagnetic tracking system consists of a field-generator, a control computer and one or more probes. Each probe features multiple coils to pick up the signal of the field generator. The field generator creates an alternating electro-magnetic field which induces the flow of currents within the coils of the probes. These currents are

amplified and processed by the control computer. Based on the measured current, the position of the probe is calculated. Modern systems, e.g. Aurora (Northern Digital Inc., Canada), can detect the probe with 6 DOF and a root mean square (RMS) error of 0.70 mm [74].

One major drawback for the daily clinical use of the system is that wires are required to connect the electromagnetic probes to the signal processing computer. As the surgeon has to cope with various cables already, e.g. for DBS electrodes, further wires in the work field are disturbing. Metallic objects in proximity to the setup present another problem for the use of electromagnetic tracking devices. They may distort the magnetic field of the field generator [75]. Furthermore, interferences between the electromagnetic tracking system and other equipment in the OT, e.g. deep brain stimulators, can occur. This might cause faulty position information from the tracking system or even undesired stimulation of the patient.

2.5.3 Localization based on static magnetic fields

As the previously discussed localization techniques are not suitable for stereotactic neurosurgery, a new localization method is required. The following criteria were specified:

- **Real time**: The new method should provide data in real time, with at least 1 frame/s.

- **Non ionizing**: To limit the exposure of the patient to ionizing radiation, the new method should work without ionizing radiation. It should not require the intake of a contrast agent or medication.

- **No cables**: To allow for easy integration in the surgical work-flow, no additional cables and wires should be required. Furthermore, the system has to be compatible to currently used probes and instruments.

The new localization method uses static magnetic fields to determine the position of the probe. This static magnetic field can be generated by permanent magnets, ferromagnetic objects or electro-magnets. The created magnetic flux is measured with several magnetic-flux sensors. Based on the flux measured at the sensors, the position of the probe is calculated. Figure 2.8 illustrates this idea and shows the difference to commercially available systems based on alternating magnetic fields. On the left,
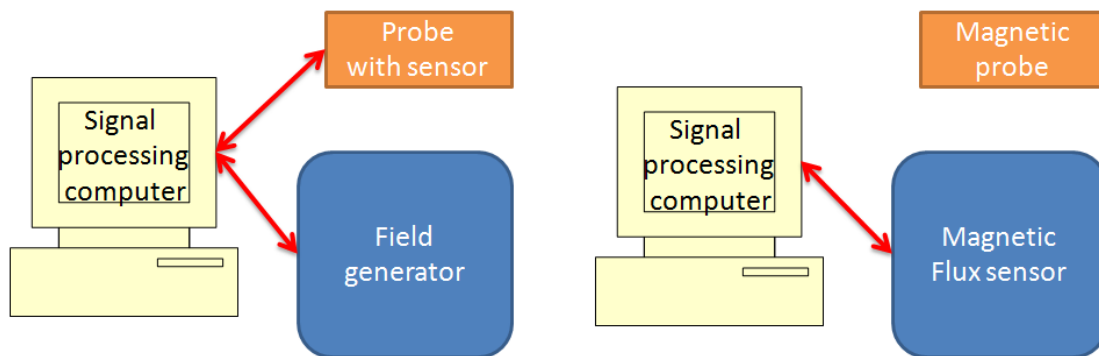
Figure 2.8: *Idea of the new localization system. Left: Conventional electromagnetic tracking system consisting of a field generator, a signal processing computer and the sensor that is attached to a probe. Right: Concept of the static magnetic field tracking with the signal processing PC, the magnetic flux sensors and the inherently magnetic probe. Double headed red arrows indicate the need to connect the components with cables.*

the components of currently used systems are depicted. On the right, the new system is shown. Note that no cable connection between the magnetic probe and the signal processing computer is required in this approach.

As the magnetic field of the probe is inherently generated, the method is robust against signal generation errors. Furthermore, static magnetic fields can penetrate biological tissue nearly without distortion. One drawback of the approach is the sensitivity to externally generated noise: The introduction of other magnetic fields, e.g. earth's magnetic field, need to be considered and compensated.

Stereotactic neurosurgery provides an ideal field for the application of static magnetic field tracking systems: First, the head of the patient is rigidly fixed. Hence, the registration between the sensors and the source does not need to be updated during the intervention. Second, the required work space is small in comparison to other surgical interventions. As the magnetic field decays rapidly, this is a major advantage: The distances between the magnetic source and the sensors is relatively small which yields a good signal to noise ratio. In most interventions only one probe is in the brain at a particular moment in time. Hence, no overlapping magnetic fields need to be considered in the application.

Table 2.4 shows the magnetic flux densities of different events. It gives the reader an overview over the expected signal from this localization approach.

Table 2.4: *Overview typical magnetic flux densities (estimations) from [76] and own calculations.*

	Magnetic flux density [T]
Driving car at 50 m	10^{-9}-10^{-8}
Permanent magnet($\varnothing 3 \times 6$ mm) at 1000 mm	1×10^{-8}
Earth's magnetic field	5×10^{-5}
Permanent magnet($\varnothing 3 \times 6$ mm) at 100 mm	1×10^{-5}
Static field in MRI	0.5-7

2.5.4 Static magnetic field tracking systems

A few devices for the localization of permanent magnets exist. So far, the examination of the gastro-intestinal (GI) tract is the main application. Here, the position of a permanent magnet that is swallowed by a patient is monitored. The permanent magnet can be idealized as a magnetic dipole. The magnetic flux $\mathbf{B}(\mathbf{r})$ generated by a dipole can be calculated as follows [77]:

$$\mathbf{B}(\mathbf{r}) = \frac{\mu_0}{4\pi} \left(\frac{3\mathbf{r}(\mathbf{m} \cdot \mathbf{r})}{r^5} - \frac{\mathbf{m}}{r^3} \right) \tag{2.1}$$

$\mathbf{B}$ denotes the magnetic flux, $\mathbf{r}$ the position and orientation of the magnet and $\mathbf{m}$ the magnetic moment of the magnet. The magnetic permeability is given by μ_0.

The current systems all share the same functional principle: A number of sensors is used to measure the magnetic flux generated by the magnet. The sensors are aligned to each other in a defined way: The distances and angles between all sensors are known. Once the magnetic flux at the sensors is digitized, the position and orientation of the source is determined. As Equation 2.1 presents an ill-posed inverse problem, it cannot be solved analytically [78]. Hence, the use of a numerical method is indicated. Most systems use the gradient based Levenberg-Marquardt [79, 80] algorithm to solve the inverse problem given by Equation 2.1.

A variety of sensors can be used, the most common sensors are: Hall Sensors, anisotropic magneto resistive (AMR) sensors, flux gate sensors or Superconducting Quantum Interference Device (SQUIDs). The most important parameters for the sensors are the resolution, the linearity and the size. For the overall system, the need for additional circuits needs to be considered as well. The number of sensors varies from

16 one dimensional to 48 three dimensional sensors.

One fact can be deduced from Equation 2.1: The magnetic flux decays rapidly with growing distance to the source. To obtain a good signal to noise ratio, the sensors need to be as close to the magnetic flux source as possible.

In the following, four distinguished systems are presented.

The first system is published by Schlageter et. al. [81]. Here, 16 Hall sensors are used to determine the magnetic flux. Each sensor measures the flux in one axis. They are aligned along a grid with 30 mm distance to each other. Every other sensor measures the magnetic flux in the X-axis, the others the magnetic flux in the Y-axis. The resolution of the sensors is around 6 μT. The setup is used to localize a cylindrical NdFeB permanent magnet ($\varnothing 6 \times 7$ mm).

No thorough resolution analysis is published. Instead, the error is estimated in a simulation. For a distance of 30 mm, the simulated error is around 1 mm, for 60 mm distance 2-4 mm. Note that the error is dependent on the orientation of the magnet. The Hall sensors are custom built for this application. A circuit to amplify the analog signals and to convert them into digital ones was designed and realized.

The second system is described by the authors Hu and Meng. Two related setups for permanent magnet localization are published [82, 83]. The first one consists of 16 Honeywell AMR 3-axes sensors HMC1043s. Their resolution is 1.2×10^{-8}T [82]. Each sensor provides 3D data about the magnetic flux. As a source, a cylindrical NdFeB magnet ($\varnothing 5 \times 6$ mm^3) is used. The analog signal of the sensors is amplified and converted. The dimensions of the sensor setup are ca. 500×500 mm^2. The reached accuracy is around 3 mm, with a strong decay for distances above 150 mm from the sensor plane.

In the second setup of Hu and Meng, the same sensor type as in the first setup is applied. Instead of 16 sensors, now 48 sensors are used. They are aligned along the inside of a cubic workspace. Now there is more sensor signal available and the maximal distance from the source to the sensors is limited. The workspace of this setup is ca. $500 \times 500 \times 500$ mm^3. The same permanent magnet as in the first setup is used as source. The accuracy is enhanced to a mean error of 1.8 mm with 97% of the position deviations lower than 4 mm.

The third system uses SQUIDs as sensors. They provide the highest resolution of all currently known magnetic flux sensors. In [76], an array of 83 1D SQUID sensors is used to measure the magnetic flux. Note that this type of sensor requires special cooling and that its implementation is very expensive.

Table 2.5: *Properties of model based static magnetic field localization systems*

Author	Sensors	Resolution	Min. error	Max. error
Hu [83]	16×3D HMC1043s	$1.2×10^{-8}$ T	0.5 mm	5 mm
Andrä [85]	1×3D HMS2300	$7.0×10^{-6}$ T	2 mm	10 mm
Schlageter [81]	16×1D Hall effect	$6.0×10^{-6}$ T	2 mm	17 mm
Weitschies [84]	83×1D SQUID	$< 1 × 10^{-12}$ T	2 mm	8 mm

The magnetic flux is not generated by a permanent magnet. Instead, a capsule (⌀10 mm) is coated with PMMA plastic. The plastic contains Fe_3O_4 particles. An external magnetic field is applied to magnetize the coated tablet. The advantage of this approach is, that arbitrary objects can be magnetized. One drawback is the resulting lower total strength of the magnetic source.

In [84] the accuracy of the approach is validated. In a distance of up to 150 mm, the position deviation is less than 2 mm and in a distance 150-250 mm, up to 8 mm. The numerical solution uses the Gauss-Seidel algorithm.

In the forth and last system, a different approach is chosen [85]. Instead of using a great number of sensors, only one 3D sensor is required. The permanent magnet is suspended in a capsule. Two parallel coils are used to generate an external magnetic field pulse. The magnet aligns with this pulse, hence its orientation with respect to the coils is known. This simplifies the inverse calculations which can now be solved with the data of one single 3D sensor.

One drawback of this approach is the need for additional coils. Furthermore, the magnet needs to be suspended to allow for alignment with the external field.

Table 2.5 gives details about the four presented systems. Some limitations in the comparison need to be considered: The size of the permanent magnets localized in the systems is not equal. In [76] a custom designed magnetic source is used. It is not as strong as the permanent magnets used in the other systems.

One important parameter for the determination of accuracy is the distance from the magnets to the sensors. They vary among the systems. Furthermore, the work space of the systems is not described with great detail.

Nevertheless, there are some conclusions to draw from the related work: High accuracy localization based on static magnetic fields is possible. The use of the Levenberg-Marquardt algorithm on the inverse problem yields good results. The sensor resolution is a key parameter for the accuracy of the system. The non-planar alignment of the

sensors is promising. The number of sensors needs to be as high as possible, or the orientation needs to be known. Furthermore, a resolution better than 10×10^{-6} T is required.

Note that the achieved accuracy of the presented systems is not sufficient for the application in neurosurgery. However, the method has great potential in the context of stereotactic neurosurgery as previously discussed.

3 Requirements for a robotic stereotaxy system

Current systems discussed in Chapter 2 provide an overview of possible solutions to the challenges of stereotactic neurosurgery. Based on the analysis of the solutions in the previous chapter, some requirements for a stereotaxy robot were deduced. Further requirements are imposed by the need to seamlessly integrate into the clinical scenario. All requirements were specified in close collaboration with our clinical (Universitätsklinikum Schleswig-Holstein (UKSH), Campus Lübeck, Department for Neurosurgery) and industrial (inomed Medizintechnik GmbH, Germany) partners. The specifications for a stereotactic neurosurgery robot will be discussed in this chapter.

3.1 Lessons from the ROBODOC

ROBODOC (Integrated Surgical Systems, Inc. ISS), CASPAR (Orto Marquet) and others caused a hype of surgical robotics in the 1990s [86, 87]. Robotic systems were mainly used in orthopedics, e.g. for total hip replacement. The main reasoning for their application was the promise of higher accuracy for cutting and milling tasks. This enhances the accuracy of the implant's fit which leads to less clearance between bone and implant and thereby improves the stability of the bone-implant interface. At the time of its introduction, ROBODOC was one of the most promising medical robots.

Compared to ROBODOC, the number of interventions performed by neurosurgical robots is small. For this reason, the example of ROBODOC is used to analyze the limitations that arise from the use of a robotic system in the OT. ROBODOC is a good example for a robotic system that was used on a regular basis in the OT for several years. It serves as representative for other fully automatic medical robots.

There were indications that the implant's fit was improved and that surgery time was reduced [88]. However, other publications reported on a high number of technical

complications during the intervention [89] and that the implant's primary stability was not enhanced [90].

The hype ended with a number of law suits against surgeons and hospitals [91] and recommendations by the 'German Bundesinstitut für Arzneimittel und Medizinprodukte' [92] and the 'Medizinischer Dienst der Spitzenverbände der Krankenkassen' [93] both stating that current data does not indicate the use of ROBODOC and similar devices.

Most first generation robotic systems, such as ROBODOC, were based on industrial robots. Several problems arise from their use in a medical environment. An analysis of limitations of these systems was conducted. Further generic limitations and requirements for surgical robots can be found in [94]. A summary of the drawbacks of first-generation medical robots is given in the following:

- **Bulky stand:** Industrial robots need a stand that provides enough space to house the power electronics of the robot. Furthermore, the dynamics of the robot require a counter weight or a rigid connection to the ground. This leads either to bulky stands limiting mobility and enlarging the footprint, or rigid installation in the operating theaters (OT)limiting mobility even further.

- **Safety zone:** As the workspace of industrial robots is several orders of magnitude bigger than the space needed for most surgical interventions, the robot can reach positions outside the operation field. The heavy robotic arm can exert great forces to objects in proximity when in motion. This necessitates a safety zone around the robotic manipulator.

- **Missing feedback:** Many surgeons rely on haptic feedback when they are evaluating a situation, e.g., tissue properties. This sense is lost in most early-days surgical robots as they were programmed to automatically position the tool at the previously defined target location.

- **Missing control:** During the intervention, the surgeon possesses limited control over the situation. The robot moves along a previously planned trajectory. If it leaves this trajectory, the surgeon can trigger an emergency stop of the system. Beside the emergency stop, there is no means to quickly interact with the robot, once the movement is started.

- **Technical complexity:** Technical difficulties were one major problem during surgery with ROBODOC [88]. This is a result of a complex technical system

being used by staff, that was not trained for this. The faulty usage of a robotic system can pose a danger to the patient.

These drawbacks, plus the fact that robotic systems are much more expensive than manual systems, lead to the currently low acceptance within the neurosurgical community [94].

Although newly developed robots overcome some limitations, the resulting second generation robotic systems, e.g., ROSA System (see Section 2.3), still suffer from several problems: A bulky stand is used in most systems. The systems are still based on modified industrial robots. Hence, their work space is not application specific and the need for a safety zone remains. Although force-torque sensors are used to detect interaction with obstacles, the robot is operated in an automatic mode. In the case of an emergency shut down, the surgeon is not able to continue the surgery manually. Furthermore, the mobility of the systems is still limited.

In the following the most important points to overcome the previously discussed limitations and drawbacks are discussed. Further requirements for a medical robot are given in [94,95]. To reach high acceptance in the neurosurgical community, the newly developed robot needs to provide the following features:

- **Mobility:** For seamless integration in the daily clinical routine, the transport between different OTs needs to be easy and safe. One single nurse should be able to perform the task without further equipment.

- **Application specific design:** Instead of an industrial robot with a work field several orders of magnitude bigger than required for the intervention, an application specific kinematic chain and design needs to be applied. The system should be based on a known kinematic chain to ease the transition between manual and robotic systems for the surgeon.

- **Control:** The newly developed robotic system should present a hybrid between robotic and manual stereotaxy and provide both: An automatic and a manual operating mode. The surgeon should be able to continue an intervention in the manual mode in case problems arise in the automatic mode.

- **Safety:** No safety zone should be necessary, to ensure possible application in all OTs. Speed and dynamics of the robotic joints should be intrinsically limited. The maximal forces exerted by the robot should not overpower a human operator.

- **Simplicity:** To paraphrase Occam's razor: The simpler the solution, the better. Highly complex systems can only be handled by specially trained staff which makes their use cumbersome and expensive. The goal of this development is a simple, reliable and competitive robotic system.

- **Compatibility:** In order to foster the acceptance of a robotic system, it needs to be compatible to currently used neurosurgical equipment, e.g. electrodes or biopsy probes.

The implementation of these abstract properties helps to overcome many of the drawbacks of first and second generation medical robots.

3.2 General

General considerations impose further requirements for a stereotaxy robot. In close collaboration with the clinical and industrial partners, three general requirements were identified: Usability and handling, compatibility, safety. Their implementation influences most of the parts and components of the robot. In combination with the required features identified in the previous section, these criteria provide an outline for the design of the new system.

Note that some requirements were already mentioned previously. In this section, their origin will be further explained and, if possible, the requirements will be quantified.

3.2.1 Usability and Handling

As discussed previously, one constraint for the use of first generation neurosurgical robots is their limited mobility and their high spatial demand. In addition to the often bulky stand, safety distances have to be taken into account when calculating the total spatial demand. In neuro-surgical OTs, space is often very limited.

Surgical staff has to be able to relocate the robot from the OT without special equipment. Furthermore, the overall spacial demand should not be greater than one standard instrument table (length $\times$ width $\times$ height $= 650 \times 500 \times 800$ mm^3), as the introduction of another bulky object to the OT is not desirable. To further increase the mobility and acceptance of the system, a possibility for battery operation is desirable. For seamless integration in the surgical workflow, it is necessary that the procedure of the system setup is intuitive, simple and error preventing. The same applies to the

handling of the robot during the actual intervention. It is desirable that two nurses can set up the system without further assistance, as specially trained staff is not always available.

In order to avoid contamination of the patient, parts in direct contact with the patient need to be sterilizable and parts in proximity to the patient have to be covered by sterile material. Furthermore, easy cleaning and maintenance of the robot is desired.

3.2.2 Compatibility

Most hospitals are experienced with manual stereotactic surgeries before they consider the acquisition of a robotic device. This leads to the conclusion that a great variety of stereotactic instruments and aids is available at the hospital. Most robotic systems require the purchase of new instruments from the producing company or an OEM, as they are not compatible to standard devices. This leads to a rise of overall costs. Furthermore, the acceptance of these silo solutions in the community is limited as surgeons and OT staff need to learn the handling of the new instruments.

For this reason, the newly developed robotic system needs to be compatible to standard neurosurgical equipment. This facilitates the transition between robotized and non-robotized procedures and at the same time limits the overall costs. Most notably, the robot has to interface the following items:

- Probes and electrodes

- Stereotactic base unit

- Micro drive unit (MDU)

- Operating table

- Surgical planning software

One key parameter for the compatibility of current probes and electrodes is the working length of the system. For the new system, it is set to 190 mm, thus resembling the ZD- and the Leksell stereotactic frame, two popular and widespread systems. This ensures compatibility to a great variety of stereotactic instruments, e.g. biopsy needles and electrodes.

To interface with different stereotactic base units, e.g. head rings, an exchangeable mounting unit is required. The connection between the stereotactic base unit and the

mounting unit needs to be rigid under application conditions. Both, the robot and the mounting unit need to be fixed to a common ground plate. To enable positioning of the robot with respect to the stereotactic base unit, the distances and angles between the robot and the mounting unit need to be well defined and reproducible.

A micro drive unit is used to feed the probes in the brain. To ensure compatibility to this device, easy, repeatable and safe mounting to the robotic positioning aid needs to be guaranteed.

The newly developed robot should be attachable to a standard operating table, comparable to the Mayfield clamp in manual systems. The connection between the table and the robot has to be rigid and stable. It is important that no permanent changes to the table are necessary. This guarantees wide acceptance in the neurosurgical community and high mobility of the system.

The development of a new surgical planning software is very time-consuming and a certification for interventions is expensive. Hence, an interface to currently used software should be provided. In stereotaxy, the trajectory is defined by two points: The entry- and target point. The trajectory definition should work accordingly in the new system.

Beside these points mentioned, it is of great importance, that the robotic system does not interfere with other equipment in the OT. For this reason, the electromagnetic noise of the system needs to be limited. This is of special interest, as the electromagnetic interference (EMI) generated by the system could interfere with the micro electrode recording (MER).

This work was created in close collaboration with inomed Medizintechnik GmbH as industrial partner. Hence ensuring compatibility to its equipment was important.

3.2.3 Safety

Safety is one of the key issues in neurosurgical robotics. For this reason a number of measures to increase the safety for the patient have to be taken:

First, no alternating current (AC) should be used to power the system, as this can cause lethal injuries [96] and presents a potential danger to the patient and surgeon alike. To limit the risk of electric injuries, the power supply of the robot should be direct current (DC) with low voltages (24 V).

Second, to minimize the risk of faulty positioning, each axis has to be equipped with two independent encoders, one of them being an absolute encoder. Furthermore, each

axis has to feature an additional manual scale. Before the intervention, the robot has to be referenced and its accuracy has to be verified. The results of this verification need to be documented. An additional external verification of the target pose is desirable. Third, the power of the axes has to be limited to minimize the danger that arises from an automated movement of the robot. The power has to be adjusted in a way that the user can manually stop the robot at all times without exerting great forces.

Forth, the robot should provide two operating modes: automatic and manual. In the automatic mode, the robot positions the probe according to a previously generated plan. In the manual mode, the robot is not necessarily connected to power. It serves as a fully passive positioning aid, just like conventional manual stereotactic frames. With this feature, it is not necessary to abort an intervention in the case of a power outage or malfunctioning of the robot. The surgeon can always continue the intervention in the manual mode.

3.3 Hardware

The previously discussed requirements impose constraints on the hardware of the robot. Further requirements are introduced by the workspace and kinematic chain as well as the desired accuracy of the system.

Common stereotactic interventions follow a two step approach: First, the probe is positioned according to the preoperative planning in which the longitudinal axis of the probe aligns with the line defined by entry- and target-point. In the second step, the probe is feed into the brain along this line until the target-point is reached. This approach requires six axes: Three translational axes to position the probe in three Cartesian directions, two rotational axes to adjust the ring and arc angle (Figure 2.3) and one additional translational axis to feed the probe into the brain.

The required workspace for the stereotaxy robot is predefined by the size of an average human head (approximately length $\times$ width $\times$ height = $170 \times 150 \times 190$ mm^3). As not all regions qualify for stereotactic neurosurgery, the actually needed workspace is slightly smaller. In this work, the workspace of the robotic system is derived from the manual ZD frame from the industrial collaborator (inomed Medizintechnik GmbH), see Table 3.1.

Several options for the kinematic chain were presented in Chapter 2. As discussed before, the use of a industrial robot kinematic chain is not desirable for medical robots. Center of arc systems allow an easy determination of the forward and inverse kinemat-

Table 3.1: *Kinematic requirements for a stereotactic neurosurgery robot; Travel ranges are derived from the commercially available Zamarano-Duchovny stereotactic frame.*

Parameter		Value
Range	x	-80–80 mm
	y	-20–65 mm
	z	0–105 mm
	α	0°–180°
	β	20°–110°
Speed	x	0.1–20.0 mm/s
	y	0.1–20.0 mm/s
	z	0.1–20.0 mm/s
	α	0.005–10°/s
	β	0.005–10°/s

ics. Furthermore, they provide an intuitive adjustment of the axes parameters (see Section 2.2.2). Additional properties are given in Table 2.2 in Section 2.2.2. To ease the transition between manual and robotic systems for the surgeon, a known kinematic chain should be used. Therefore, the kinematic chain of the newly developed robotic system should resemble the kinematic chain of the manual ZD system. With this design decision, the kinematic chain of the robotic system is specified. Table 3.1 also gives the desired speed of each axis as specified by the industrial collaborator.

In section 3.2, it was specified that the robot has to provide an automatic and a manual operating mode. Hence the drive train of each axis has to be designed such that manual manipulation is possible without damage and without applying great forces or torques. As no torques are exerted by the motors in the manual mode, all axes have to be self-locking to enable manual operations. Furthermore, the controllers of the axes have to provide feedback about the current load to the user.

In the DBS community, a consensus exists that higher accuracy is one of the key issues for further advancement of the field [97]. The newly developed robotic system should be at least as accurate as currently used manual and robotic systems. Table 3.2 summarizes the desired accuracy of the robotic system. Furthermore, the smallest step-width for each axis is specified.

Table 3.2: *Accuracy requirements for a stereotactic neurosurgery robot*

Parameter		Value
Stepwidth	x	$10\mu m$
	y	$10\mu m$
	z	$10\mu m$
	α	$0.005°$
	β	$0.005°$
Absolute accuracy		0.5 mm
Repeatability		0.3 mm
Application accuracy		0.7 mm

3.4 Software

Based on the generic workflow for stereotactic interventions and the analysis of the clinical workflow in Section 1.1, the following tasks for the stereotactic planning and control software were identified:

- **Registration:** The coordinate frames involved in the stereotactic planning need to be registered to each other.

- **Visualization of imaging data:** Preoperative CT and MRT images are displayed to the surgeon. Image fusion from CT and MRT is necessary to facilitate the identification of the target.

- **Preoperative path planning:** Based on the displayed images, the surgeon specifies the target- and entry point for the probe. Depending on the operation, multiple trajectories can be required.

- **Trajectory execution:** After the planning phase, the robot has to execute the planned trajectory. Therefore, it actuates its axes in a way that the desired pose is reached.

- **Intraoperative robot control:** In case of emergency or faulty positioning of the robot, the user has to be able to reposition the robot during the surgery.

- **Intraoperative status monitoring:** The software has to monitor and log the status of the axes and sensors during the intervention [94]. The user needs to be warned if the system shows unexpected behavior.

As discussed earlier in this section, the commercially available surgical planning software from the industrial collaborator (Praezis Plus, TatraMed spol. s r.o., Slovakia) is used for the registration, the visualization and the path planning. The newly developed software for the robotic device needs to position the robot according to this planning.

Furthermore, several general requirements for the control software were identified. The new software should provide a graphical user interface (GUI). A TCP/IP interface, to connect the robotic system to third party software also needs to be implemented.

The application of the robotic system should reduce the overall treatment time and especially reduce the time the patient is under anesthesia. Hence, the control software needs to be intuitive to use. Furthermore, it has to seamlessly integrate into the surgical workflow. To guarantee the highest possible safety for the patient, redundant safety features need to be included.

4 The Motor Assisted Robotic Stereotaxy System MARS

In Chapter 3 the requirements for a robotic neurosurgery system are described and, wherever possible, quantified. In this chapter the mechanic and electronic design of the newly developed robotic system is derived from the requirements. The **M**otor **A**ssisted **R**obotic **S**tereotaxy system, short MARS, aims to overcome the previously discussed limitations of manual and robotic systems. The chapter is subdivided into five section:

First, the design of the robot is discussed and the concept for a highly mobile robotic system is introduced.

Second, the hardware of the MARS is described in detail. The translational and rotational axes' drive trains are explained. Furthermore the properties of the motor controllers and encoders are discussed. The development of a motorized micro drive unit to forward the probes into the tissue is presented.

Section 4.3 explains the control of the robot and its software. It gives details about the general control concept and the calibration of the encoders.

In the forth section the kinematic calculations of the robot, i.e. forward and inverse kinematics, are presented. Furthermore it is explained how the referencing of the robot works. An analysis of the accuracy of the kinematic chain is conducted. To conclude, a calibration method to correct for inaccuracies is presented.

Fifth, the four different operating modes of the MARS are discussed. Their properties are analyzed and compared.

Based on the design sketch and hardware specifications presented in this chapter, IBG Technologies Hansestadt Lübeck GmbH, Germany, performed the final design and the assembly of the MARS.

4.1 Design

In this section, the steps that lead from the clinical scenario (Section 1.1) via the requirements (Chapter 3) to the first design sketches of the new robotic system are presented. The main purpose of the first draft was to communicate the design ideas to the clinical and industrial collaborators. Based on this draft, the robot was designed and specified.

Summarizing the design requirements: The goal is to create a light-weight robot that can easily be transported between OTs. The robot has to outperform current manual solutions in terms of safety, usability and accuracy. The required space should not be greater than that of currently used manual systems. Furthermore, the robot should be mountable to a standard operation table. A 'center of arc' kinematic chain is desired, as this facilitates the kinematic calculations. The alignment of the axes should resemble the ZD frame (see Figure 2.2) to ease the transition between manual and robotic devices and thereby leading to higher acceptance amongst surgeons.

The clinical scenario is derived from three sources: First, the literature discussed in Chapter 1. Second, the experience from our clinical and industrial partners and third numerous visits to stereotactic neurosurgeries by the author.

Figure 4.1 shows a computer-aided design (CAD) draft of the clinical scenario. A patient (bluish cloth) lies on the operating table with a head ring fixed to his skull. The head ring is rigidly connected to the ground plate of the robot. The ground plate of the robot in turn is attached to the side rails of the operating table.

The power electronics of the robot are housed on an instrument table which is also used to transport the system. A surgeon (green scrubs) controls and supervises the movements of the robot. The robot itself features three translational axes (labeled **t1**, **t2** and **t3**) in its base. The arc is rotated about its suspension by a fourth axis, labeled **r1**. A fifth axis, **r2**, moves a carriage along the arc. A tool-mounting is attached to the carriage. The micro drive unit can be fixed in this mounting. The power electronics and the control PC are attached to the wagon. One single cable connects the robot with its control PC and power electronics.

To reduce the overall weight of the system, structural parts such as the ground plate and the semi-circular arc are made of Carbon-fiber-reinforced polymer (CFRP). The design of a light-weight system facilitates handling and enables a highly mobile system. The described system features the following properties:
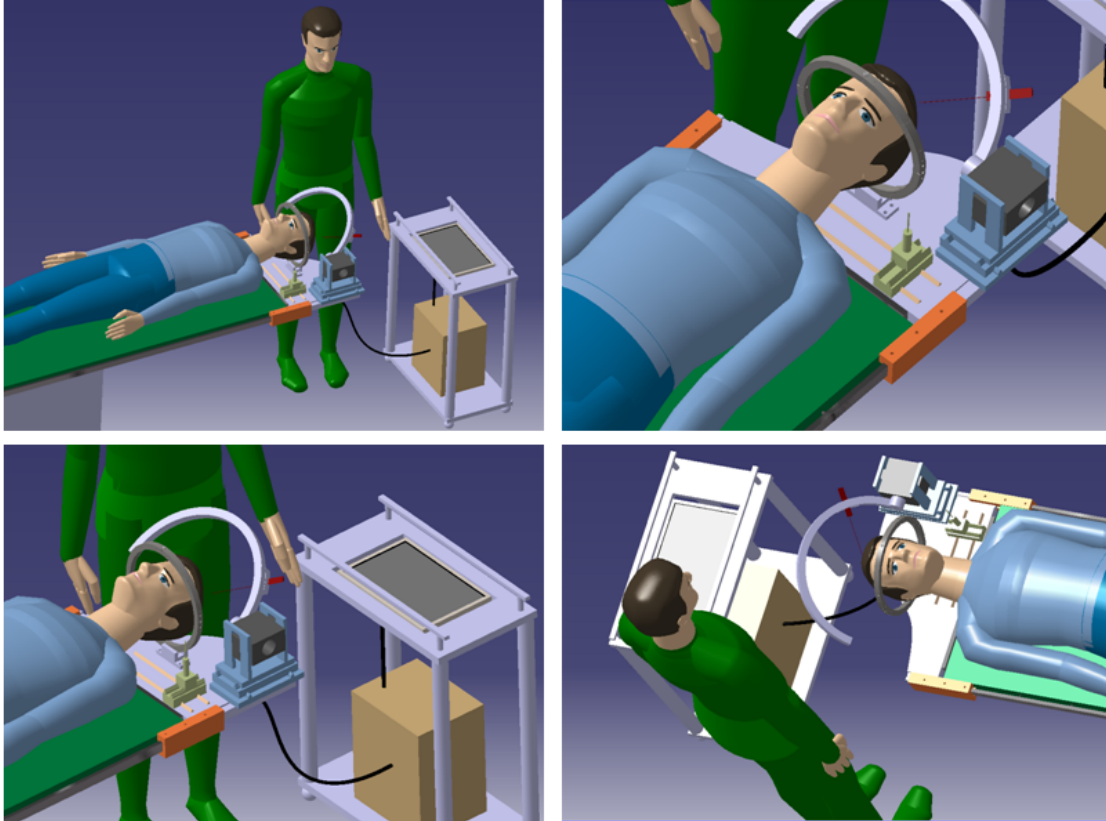
- Highly mobile system

Figure 4.1: *Clinical scenario for the MARS from different angles: The patient lies on an operating table. A stereotactic base unit is fixed to the head of the patient and to the ground plate of the robotic system. The surgeon (green) operates the robot. MARS is attached directly to the operating table. The power electronics and the control PC are attached to the wagon.*

- Compatible to standard equipment

- Center of arc based system

Based on the requirements specified in Chapter 3 and this first design, the hardware components of the robot were selected. The mechanical and electrical properties of the design will be discussed in the following section.

4.2 Hardware

This Section is subdivided into six parts: First, the drive trains for the five automated axes are described. To start, the drive train of the translational axes is presented. Next, the drive trains of the two rotational axes will be discussed. Second, the properties of the motor controllers will be explained. In the third part, the position encoders of the MARS are covered. The fourth part describes the setup of the hardware. The fifth part explains the design of a target point simulator, which provides additional safety. In the sixth part, the design and evaluation of a motorized micro drive unit is covered.

4.2.1 Drive trains

From the requirements discussed in Chapter 3, those applying to the drive trains were extracted. The following list explains, how these requirements effect the selection of the drive trains' parts:

- **Accuracy:** A high precision motor-gear combination is required. The motor needs to incorporate an encoder to monitor the position of its shaft. The clutch and the spindle need to work together backlash free, which is why a ball screw system was selected. The movement of the stage needs to be directed by guides. The torques required to actuate the axes should be as low as possible, hence the ball screw is supported by bearings.

- **Step width:** An intelligent controller that enables small step widths is required. Furthermore, the backlash of the whole translational drive train needs to be smaller than the smallest desired step width. Otherwise, a step command will not show any effect if the direction of motion has changed.

- **Travel range:** The length of the guides and the ball screw needs to be adapted to the desired travel range. At the same time a compact design is desirable as this reduces the overall footprint of the robot.

- **Manual and automatic operating mode:** The drive train needs to support both, manual and automatic operation. This requirement limits the selection of gears, as gears with high gear ratio are self-locking and cannot be manipulated manually. Furthermore, the gear must not be damaged when the knob is manipulated. At the same time, the gear-ball screw combination needs to be self-locking to prevent undesired movement of the axes when operated in manual mode.

- **Electro-magnetic compliance:** The electromagnetic noise caused by the motors must not interfere with MER hardware or other sensitive equipment in the OT. The main noise source is the commutation of the segments of the motors. Each time the brushes break contact with a commutator segment at the commutation point, the energy of the magnetic field of the motor windings causes an arc or a voltage spike between the brushes and the commutator segment. This voltage change results in an undesired EMI. For this reason, brushless commuted DC motors are used in the robot. Brushless DC motors inherently exhibit less EMI as they can commute their segments electronically without brushes [99]. Furthermore, they can produce more torque per weight and are more energy efficient. This results in a lower radiation of heat to the vicinity [100].

In the MARS, translational and rotational axes are used. The requirements for both axis types are nearly similar, however, their implementation differs. In the following, the drive trains of the translational axes will be discussed. After that, the design of the drive trains for the rotational axes will be explained.

4.2.1.1 Translational drive train

The translational drive train moves the robotic system along a straight line defined by the guiding rails of the considered axis. Figure 4.2 depicts the exemplary drive train of the first translational axis **t1** of the robot. The two structural parts are mounted to the ground plate. The motor with its gear is connected to the ball screw using a clutch. The ball screw is supported on both ends with ball bearings. Two guides are used to ensure strictly translational movement of the stage. The ball nut is attached
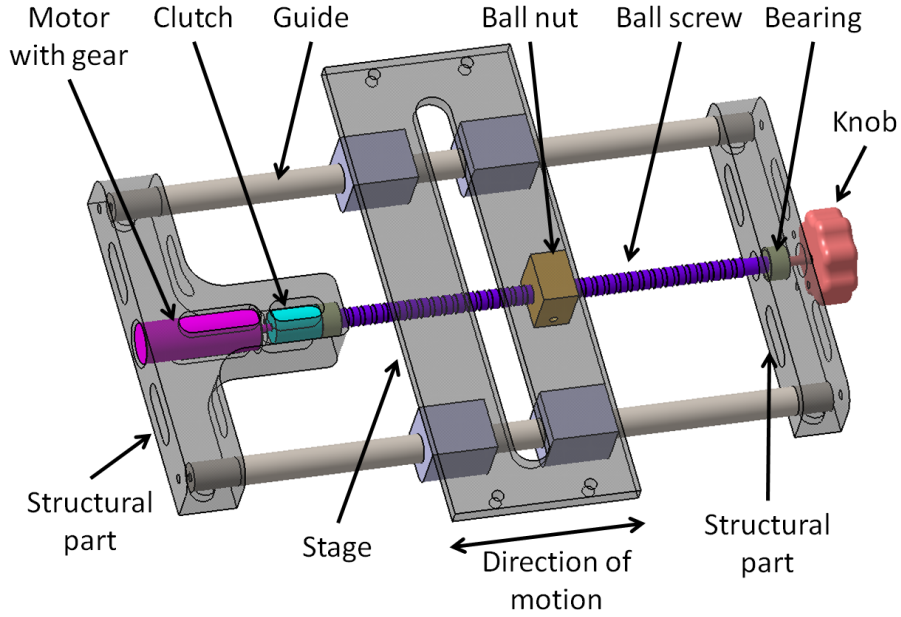
Figure 4.2: *Translational drive train of the MARS. Exemplary shown with translational axis **t1**.*

to the stage and transfers the motion of the motor into a translational movement of the stage.

The same principle is used in the other translational axes. Its main elements are the motor with gear, the clutch, the ball screw with nut, the guides, the bearings, the knob and the structural parts.

For the translational axes of the robot, three ball screw systems (KG17072 KGT-Z-08-01-208-180-O-VA-IT3) from Karl Hipp GmbH, Germany were used. They feature a spindle pitch of 0.5 mm per revolution. Thanks to the pre-loading of the system, the backlash is eliminated. The length of the ball screw and the guiding rails needs to provide the required travel range for the considered axis. To guarantee high precision positioning of the spindle, a torsionally stiff coupling was selected. Furthermore, the selected coupling provides large radial compensation, which is beneficial if the spindle and the motor shaft are not aligned correctly. The coupling provides electrical insulation between the spindle and the motor shaft. This increases the security for the patient: In case of electronic malfunction of the motor, the current cannot be transferred to the spindle and further in direction of the patient.

The most important part of the drive train is the motor-gear unit. For the previously

Table 4.1: *Motors and gears used in the translational axes of the MARS; The specification of motor, gear, gear ratio, resulting theoretical positioning resolution and maximal backlash at no load are given.*

Axis	Motor	Gear	Ratio	Theoretical Res.	Backlash
t1	1628T024B	K1155 167	14:1	$0.012\mu m$	$1.39\mu m$
t2	1628T024B	K1155 167	14:1	$0.012\mu m$	$1.39\mu m$
t3	1628T024B	K1155 167	14:1	$0.012\mu m$	$1.39\mu m$

discussed reasons, a brushless DC motor was selected. Table 4.1 gives an overview over the selected models with the chosen gear ratios. The maximal torque supported by the bearing must be smaller than the torque occurring when the system is operated in the manual mode.

The applied Faulhaber 1628 motors (Table 4.1) feature integrated Hall sensors that monitor the position of the motor shaft with 3000 counts per revolution [101]. The theoretical translational position resolution $\mathbf{r}$, which is equal for all three translational axes, can be calculated:

$$\mathbf{r} = \frac{spindle\ pitch}{counts\ per\ revolution \times gear\ ratio} = \frac{0.5\ mm}{3000 \times 14} = 0.012\ \mu m \tag{4.1}$$

This theoretical resolution of 0.012 μm is also given in Table 4.1. Note that this resolution is not reached in the actual system, as the backlash β of the K1155 167 14:1 gear at no load is specified with $\beta \leq 1°$ [102]. This results in a maximal backlash of the stage $\mathbf{b}$ at no load of:

$$\mathbf{b} = \frac{spindle\ pitch}{gear\ backlash} = \frac{0.5\ mm \times 1°}{360°} = 1.39\ \mu m \tag{4.2}$$

This shows, that the calculated accuracy of the system is even better than demanded by the requirements defined in Chapter 3. At this point it is not possible to specify the overall accuracy of the axes as other components, e.g., clutch, or the introduction of load, can introduce further inaccuracies. Please note that various experiments to evaluate the accuracy of the system were conducted in the scope of this work. They will be discussed in Chapter 6.
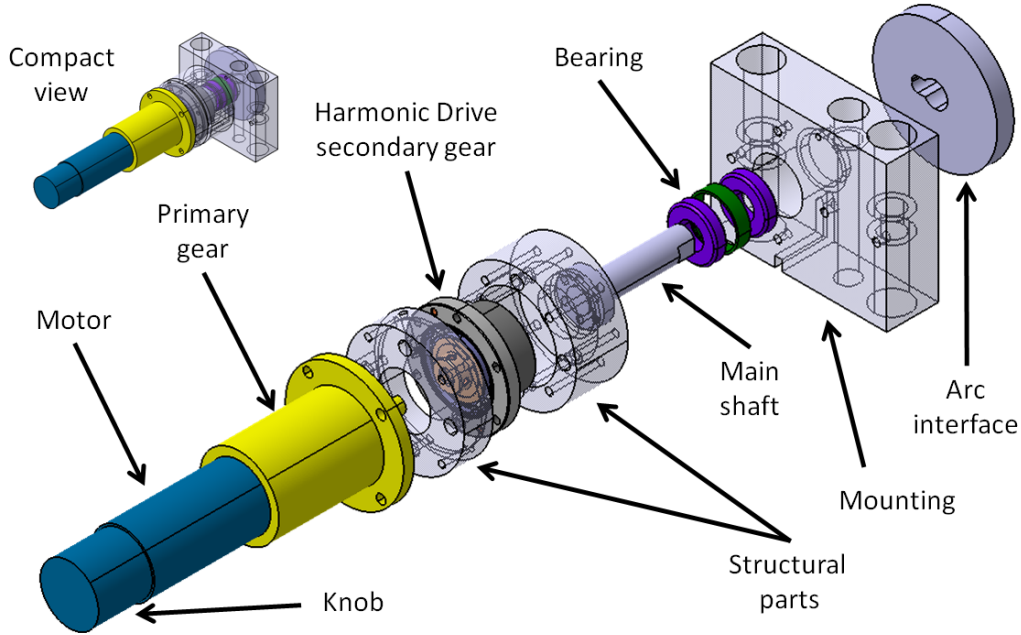
Figure 4.3: *Exploded view of the drive train of rotational axis **r1**. Top left, the assembled compact view of the drive train.*

4.2.1.2 Rotational drive train

Brushless commuted DC motors are used because of their superior EMI properties. In contrast to the drive train of the translational axes, two different designs are used for the rotational axes. This is necessary, as the required motion differs for the two rotational axes: Axis **r1** rotates a semicircular arc about its mounting. Axis **r2** moves a carriage along this semicircular arc (Figure 4.1). First, the drive train of rotational axis **r1** will be explained and then the drive train of **r2** will be covered.

Rotational axis **r1** is used to rotate the semi-circular arc about its suspension. This axis needs to support very high torques, when compared to the other four automated axes, as the arc serves as a lever. Figure 4.3 shows an exploded view of the drive train of rotational axis **r1**.

The motor is rigidly connected to the primary gear. A knob is attached to the motor to enable manual manipulation of the axis. The primary gear mounts to the secondary gear stage (HFUC-14-100, Harmonic Drive AG, Germany). The main shaft is fixed to the secondary gear and supported by two ball bearings which in turn are attached to the mounting part. The mounting part can be connected to the guides and ball screw system of translational axis **t3** (not shown). An interface for the semi-circular arc is

fixed to the rear end of the main shaft. On the top left of Figure 4.3, the drive train in its assembled state is depicted. Full rotation is possible with **r1**, hence the required travel range is reached.

At first glance, it might appear confusing to use two gear stages, but a secondary gear is necessary for the following reason: The semi-circular arc serves as a lever for forces applied to it which results in high torques exerted on the **r1** axis. The minimal length of the lever arm is **l** = 190 *mm*, to ensure compatibility with current equipment (see Chapter 3). The gear of **r1** needs to absorb these torques and forces. The Faulhaber company offers standard gears that can cope with these requirements, however their backlash β is specified with $\beta < 1°$ [102]. The resulting backlash motion **bm** at the far end of the arc can be calculated as follows:

$$\mathbf{bm} = sin(\beta) \times \mathbf{l} = sin(1°) \times 190 \ mm \approx 3.5 \ mm \tag{4.3}$$

This motion violates the requirements for high accuracy and high repeatability. Furthermore, this backlash is not only visible on motion direction changes, but results in a wobbling motion at the far end of the arc.

To overcome this problem, a cycloid gear was used. It can absorb high torques, especially in radial direction, and it is inherently free of backlash [103]. The gear ratio of stage 1 is 246:1 and 100:1 for stage 2. The resulting theoretical position resolution **r** is calculated as follows:

$$\mathbf{r} = \frac{360°}{counts \ per \ revolution \times gear \ ratio \ 1 \times gear \ ratio \ 2}$$
$$\mathbf{r} = \frac{360°}{3000 \times 246 \times 100} = 4.88 \ \mu° = 0.077 \ \mu rad \tag{4.4}$$

With the implementation of the secondary gear, the backlash was reduced to:

$$\mathbf{b}_{new} = \frac{\beta}{gear \ ratio \ 2} = \frac{1°}{100} = 0.01°$$
$$\mathbf{bm}_{new} = sin(\mathbf{b}_{new}) \times \mathbf{l} = sin(0.01°) \times 190 \ mm \approx 0.033 \ mm \tag{4.5}$$

Furthermore, the backlash only occurs after motion direction changes. The previously discussed wobbling is suppressed thanks to the inherently backlash free cycloidal gear. The results are summarized in Table 4.2. Note that as for the translational axes, the
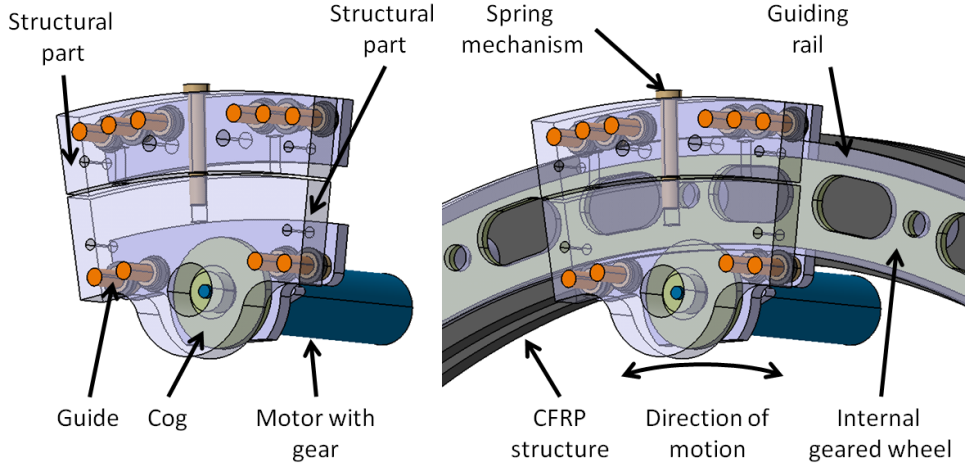
Figure 4.4: *Drive train rotational axis r2. Left: Motor subassembly with structural parts, guides (orange), motor with gear and cog. Right: Motor subassembly mounted to the semicircular arc.*

theoretical smallest step width equals the position resolution of the axes.

Figure 4.4 depicts the drive train of rotational axis r2. On the left, the motor assembly group is shown. It consists of the motor with gear, a cog attached to the gear shaft, two structural parts, ten guides (orange) and a spring mechanism. The spring mechanism pulls the two structural parts together, thereby ensuring contact of the cog with the internal geared wheel. On the right, the motor subassembly in contact with the semicircular arc is displayed. The guiding rail and the internal geared wheel are connected to the carrying CFRP structure of the arc. The direction of motion is indicated by a double headed arrow in Figure 4.4.

To ensure self-locking of the axis, a high gear ratio of 246:1 was selected. The pitch circle diameter of the cog and the internal geared wheel are $\mathbf{d_1} = 25\ mm$ and $\mathbf{d_2} = 367\ mm$, respectively. Hence, the second gear ratio is 367:25 The theoretical position resolution $\mathbf{r}$ of the internal encoder per degree can be calculated as follows:

$$\mathbf{r} = \frac{360°}{counts\ per\ revolution \times gear\ ratio\ 1 \times gear\ ratio\ 2}$$
$$\mathbf{r} = \frac{360°}{3000 \times 246 \times 14.68} = 33.2\ \mu° = 0.521\ \mu rad \tag{4.6}$$

The backlash of the gear is specified by $\beta \leq 1°$ [102]. At no load, this results in a

Table 4.2: *Motors and gears used in the rotational axes of the MARS; Gear ratio and resulting positioning resolution*

Axis	Motor	Gear	Ratio	Resolution	Backlash
r1	3056K024B	K312 K1155 381 MBZ 24V	246:1		
		Harmonic Drive HFUC-14	100:1	$4.88\mu°$	0.01°
r2	1628T024B	K1155 167	246:1		
		Custom designed gear	14.68:1	33.2 $\mu°$	0.068°

maximal rotational backlash **b** of the rotational axis and the resulting translational movement **bm** can be calculated:

$$\mathbf{b} = \frac{gear\ backlash}{gear\ ratio\ 2} = \frac{1°}{14.68} = 0.068°$$

$$\mathbf{bm} = sin(\mathbf{b}) \times \frac{\mathbf{d}_1}{2} = sin(0.068°) \times 12.5\ mm \approx 0.015\ mm$$

(4.7)

Table 4.2 summarizes the motor-gear combinations used for the two rotational axes. Furthermore, the resulting encoder resolution and the expected backlash is given.

4.2.1.3 Summary

The selected Faulhaber motors provide high precision shaft position control. Thus, it is possible to monitor the position of each axis with sufficient accuracy. For the translational axes, the backlash free ball screw systems enable highly accurate positioning. A theoretical overall backlash of only 1.39 μm was calculated. This is also possible with the rotational axis: In **r1**, a secondary backlash free gear stage was introduced to suppress wobbling of the arc structure. The expected backlash is 0.01° which results in a movement of the arc at the far end of 0.03 mm. For **r2** a backlash of 0.069° was determined. The resulting motion is 0.015 mm.

The smallest possible step width of each axis is equal to the positioning resolution of the encoders of the motors. For the translational axes, the smallest step width is 0.012 μm and for **r1** and **r2** 4.88 $\mu°$ and 32.2 $\mu°$, respectively.

Table 4.3 gives an overview over the travel ranges of the five automated axes. The required travel ranges are defined by the guides and ball screw systems for the translational axes. Rotational axis **r1** is primarily unlimited in its motion. Note that for the safety of the patient, the travel range is restricted by software. Axis **r2** moves along

Table 4.3: *Travel ranges of the five automated axes*

Axis	Range
t1	-1.5–145 mm
t2	-45–67 mm
t3	-55–41 mm
r1	0–360°
r2	-70–70°

the semi-circular arc structure. Its bounds are designed such that the required travel range is provided.

Manual and automatic operating modes are supported by all axes. All axes are self locking. The three translational axes feature a knob attached to the ball screw system to manipulate their position. Rotational axis **r1** provides a knob mounted to the motor and axis **r2** can be manipulated by pushing it from either side. The force required to move the axis is high when compared to the forces occurring in normal operation. This guarantees that the axis does not move accidentally.

The brushless commuted Faulhaber motors used in all five axes exhibit very low electromagnetic noise.

To conclude, the requirements for the drive trains are fulfilled by the presented system. Note that the values given in this section are only theoretical. Several experiments were conducted to validate the properties of the system. They will be discussed in Section 6.

4.2.2 Controllers

Each of the five brushless DC motors requires a separate controller unit. The controllers convert the commands from the user to currents and voltages which drive the motors. The requirements applying to these controllers are summarized in the following:

- **Accuracy:** The controllers need to monitor the position of the motor shafts with high temporal and spatial resolution. Furthermore, they need to manipulate their position. It is necessary to move the motor stepwise and hold a once reached position.

- **Manual and automatic operation:** In some cases it is desirable to contin-
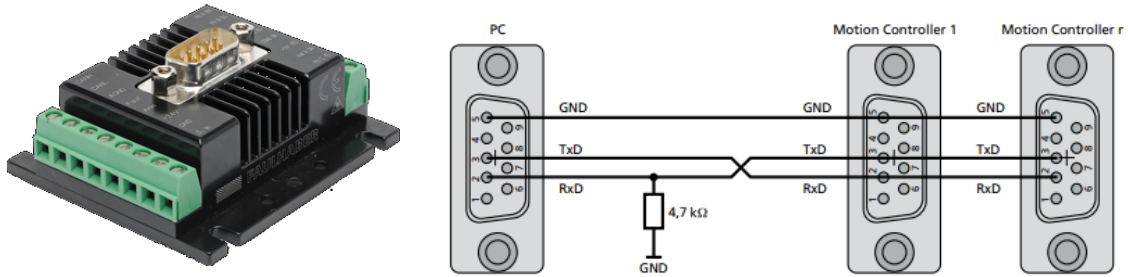
Figure 4.5: *Left: Faulhaber MCBL3006s controller unit; Right: Multiple MCBL3006s units can be controlled in daisy-chain mode by one single serial interface. Images courtesy of Faulhaber GmbH.*

uously monitor the position of the axes, even when the system is operated in the manual mode. For this feature, a function to disable the amplifiers of the controllers while at the same time monitoring the position of the motor shaft needs to be provided.

- **Simplicity:** To ensure that the system is as mobile as possible, the controllers should not require additional hardware, e.g. a motion control card. Instead, the whole system should be controllable via one single USB connection.

- **Safety:** The controllers need to provide feedback about the currently required electric current. This is necessary to detect interaction with the user or an obstacle. To minimize the danger for the patient and the surgeon, a function to limit the maximal current drain is required. Furthermore, the maximal travel-range needs to be adjustable.

The Faulhaber MCBL 3006s controller unit provides all the above mentioned functionalities. Several Faulhaber MCBL3006s units can be controlled using a single RS232 interface [101]. A USB-to-serial converter is used for the communication with the PC,. Figure 4.5 shows one controller unit (left). On the right, the electric connections to operate multiple controllers with one single serial port is displayed. This mode is called daisy-chain operation mode.

The five MCBL3006s controllers are housed in a metal box which is mounted underneath the ground plate of the robot (Figure 4.6). An USB connector provides an interface to the controllers. Furthermore, a connector for power and ground is provided. The USB to serial converter manages the communication between the software
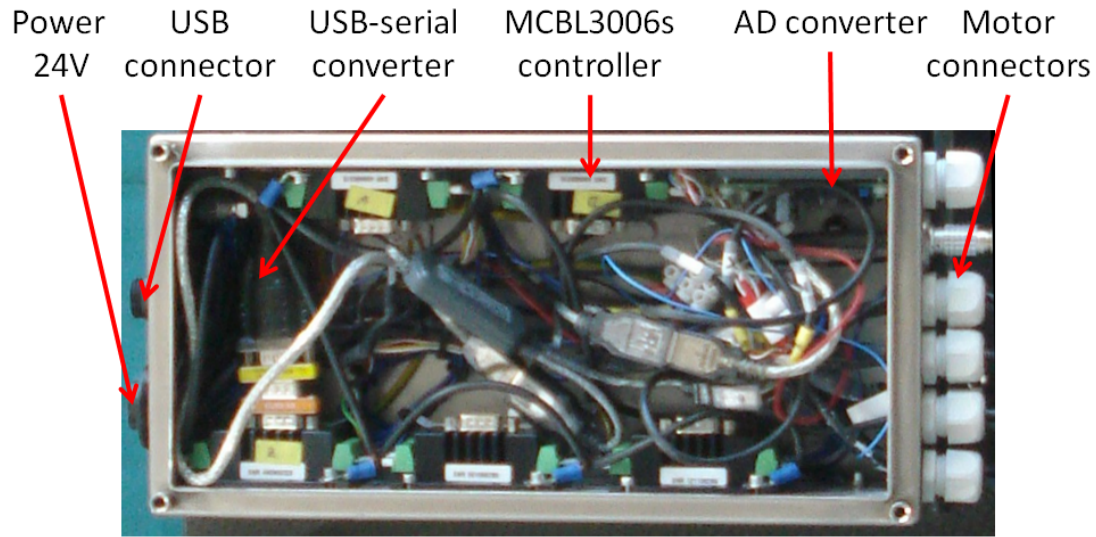
Figure 4.6: *Controller box of the MARS*

and the controllers. Furthermore, an AD converter for the absolute encoders of the translational axes is installed in the box. On the right of Figure 4.6, the connectors to the motors of the axes are shown. Note that the electronics for the absolute encoders of the rotational axes are attached to the lid of the box and are not shown here.

The controllers require 24 V direct current. Each unit can provide a peak current of 3 000 mA and a continuous current of 500 mA [101]. The signals from the Hall encoders of the motors are analyzed by the controllers. Each revolution of the motor shaft is monitored with a resolution of 3 000 counts per revolution. Furthermore, the controllers provide the following functions:

- **Position control:** A target position for the axis can be specified. The motor shaft is automatically moved to this position. A closed loop PID control enables the system to hold this target position. The parameters of the PID controller can be adjusted to suit the application. This enables accurate positioning of the axes and holding of a specified position.

- **Amplifiers:** The amplifiers of the controller that drive the motor can be enabled or disabled. The electromagnetic noise generated by the motors can be reduced by disabling the amplifiers. This feature is important for applications involving micro-electrode recordings, e.g. DBS, and the manual operating mode.

- **Position monitoring:** The current position of the motor shaft can be polled from the controller. This is also the case when the amplifiers are disabled. Furthermore, velocity monitoring is available. Here the current revolutions per minute at the motor shaft can be queried. The provided data helps the user to determine if the axis is positioned correctly. Furthermore, desired and undesired movement of the axis can be detected.

- **Current monitoring:** The current dissipated by the motor is available to the user. This contains information about the load on the motor shaft. If an obstacle is hit or when the user is interacting with the axis, the current dissipation will rise. The rise is detected by the control software and appropriate measures can be initiated.

- **Safety limits:** To enhance the safety of the system, a current limit for the peak and continuous current can be defined. Furthermore, the maximal revolutions per minute of the motor shaft can be adjusted. An upper and lower bound for the motor shaft position can be set. The user can specify no-go areas and limit the overall speed and torque of each motor.

The controllers require a 24 V DC power source. Power electronics can cause interferences with MER equipment. For this reason, the AC/DC converter is not installed in the controller housing. Instead, it is placed as far away from the electrode recording site as possible, at the instrument table (see Figure 4.1). A cable transfers the power to the controllers. Thanks to this setup, the EMI are minimized.

The controller units are the core components of the automated axes. The described properties show, that safety features and different operating modes can be realized. One drawback of the motor-controller combination applied is the missing absolute position monitoring. So far, only relative positions are available. For this reason, as well as for additional patient safety, secondary absolute encoders are installed at each axis. Their implementation and properties are described in the next subsection.

4.2.3 Encoders

Beside the internal Hall encoders, each axis is equipped with an absolute encoder. This measure ensures highest possible safety for the patient. All three translational axes use potentiometric encoders of the same type. The MBW encoder (Megatron AG, Germany) was chosen for its small dimensions and the very high theoretical
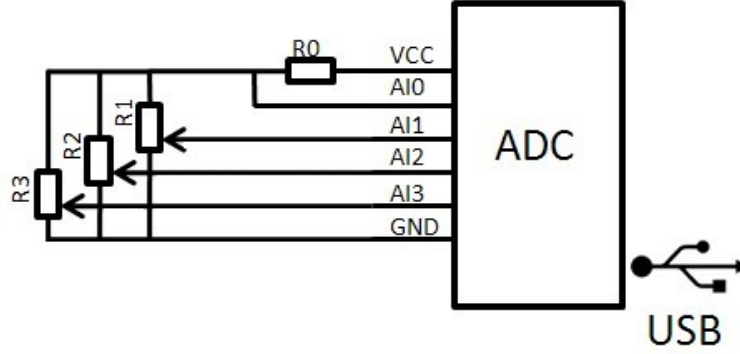
Figure 4.7: *Wiring of the absolute encoders for the translational axes. The analog-digital converter is connected to the USB port of the control PC. The voltage drop for each of the three potentiometric encoders as well as the reference voltage is measured on the corresponding channel AI0-AI3.*

resolution [104]. There are two drawbacks: The linearity tolerance of the encoders is specified with $>1\%$ and their resistance tolerance with 20%. These facts necessitate a calibration of the absolute encoders further discussed in Section 4.3.

Note that the actual achievable resolution is limited by the analog to digital converter (ADC) and the voltage source used in the setup. Here the HB627 USB (H-Tronic GmbH, Germany) ADC was used. It samples with 12 bit resolution, a frequency of up to 300 Hz and it provides eight analog channels [105]. The travel ranges of the three translational axes are ≤ 160 mm (see Table 3.1). Hence the theoretical position resolution **r** of the absolute encoder can be calculated:

$$\mathbf{r} = \frac{160\ mm}{2^{12}} = 0.039\ mm \tag{4.8}$$

The resulting accuracy **r** is sufficiently high for the application. The electronic setup of the encoder and the ADC is depicted in Figure 4.7. The ADC is powered by the USB voltage of 5.0 V. This voltage is forwarded to each of the three potentiometric encoders. The voltage at the potentiometers wiper is directly proportional to the position of the wiper. To adjust the voltages to the range of the ADC (0–4096 mV), an additional resistor (R0) is introduced.

In order to create a system that is robust against supply voltage fluctuations, the relative voltage is used to determine the position. First, the analog input AI0 is measured. This channel is connected directly to the supply voltage. Next the channel

corresponding to the desired axis, e.g. AI1, is queried. The value of AI1 is dependent on the supply voltage and the position of the wiper. The ratio between AI1 and AI0 gives the relative voltage of the potentiometric encoder and cancels out the influence of the supply voltage fluctuations.

For the two rotational axes, a digital inclinometer is used. An inclinometer measures the tilting with respect to the g-force. For the task of leveling the two rotational axes perpendicular to the ground plate, two separate inclinometer units are necessary. The first unit is housed in the controller box of the robot. The first unit measures if the operating table with the robot attached is tilted.

The second unit is attached to the carriage moving along the arc. In order to align the rotational axes to the ground plate of the robot, the angular difference between the two inclinometer units is calculated.

In the MARS two SCA100T-D02 dual axes inclinometer (VTI Technologies Oy, Finland) are used. They are controllable via Serial Peripheral Interface (SPI) and feature a resolution of $0.07°$ [106]. To integrate the inclinometers in the robot framework and to communicate with the inclinometer units, an interface board was designed. The interface board features an AT90USB162 (Atmel Corporation, USA) micro-controller unit (MCU), which is used to control the inclinometers and to communicate with the control PC. Therefore, it emulates a serial port using the Communication Device Class (CDC). The control software was programmed in C using AVR-Studio 4.

Two printed circuit boards (PCB) were designed: The first board, houses the MCU and the first inclinometer. This PCB is embedded into the controller box of the robot where it is connected to a USB hub. The second PCB houses the second inclinometer unit and three status light-emitting diodes (LED). The PCBs are connected to each other.

Figure 4.8 summarizes the wiring of the MARS hardware. A control PC connects via one single USB cable to the USB hub of the robot. The USB hub in turn is connected to the AD converter, the inclinometer PCB and a USB-serial converter. USB communication is indicated with red arrows, SPI with blue, serial with green and other information transmission with black. The USB-serial converter is used to control the MCBL units for the motors (see Subsection 4.2.2). The MCBL units are interconnected and share the same RX and TX lines for communication (see Figure 4.5). The AD converter is connected to the three potentiometric encoders of the translational axes (see Figure 4.7). The MCU interface controls the two inclinometer units as well as three status LEDs.
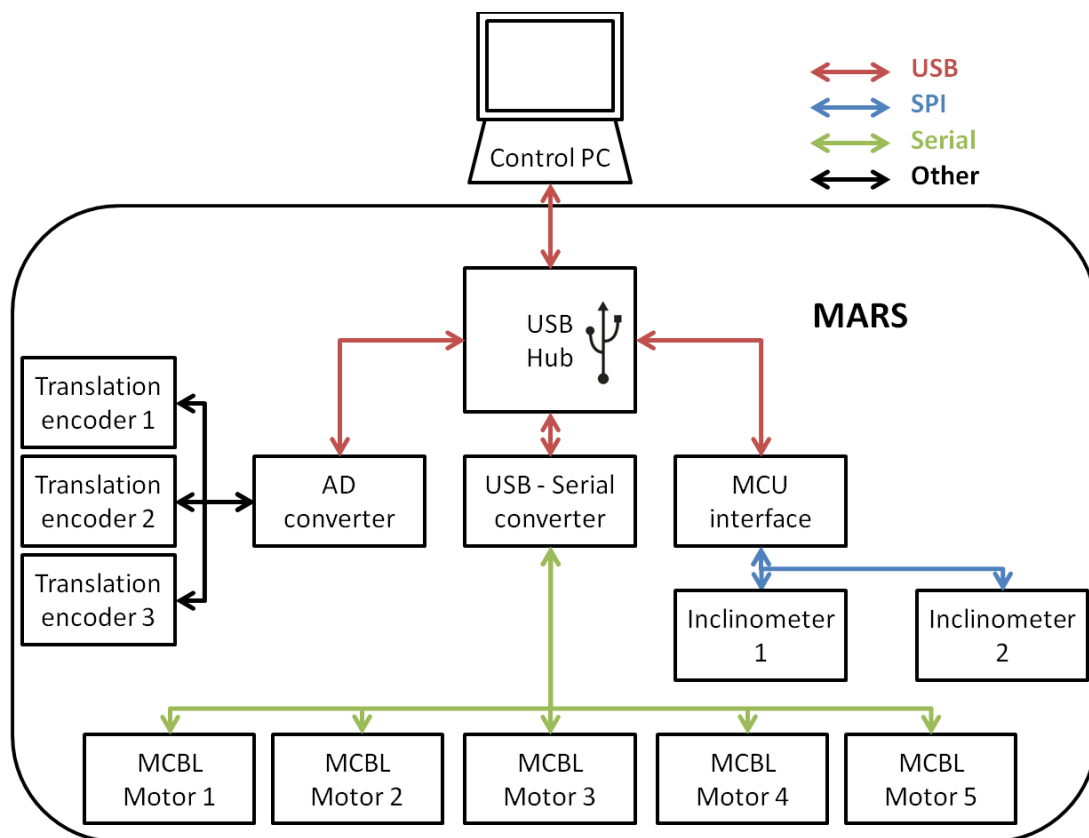
Figure 4.8: *Control structure of the MARS robot: A PC is connected to the MARS via USB. The encoders, controllers and inclinometers provide interfaces for USB communication.*
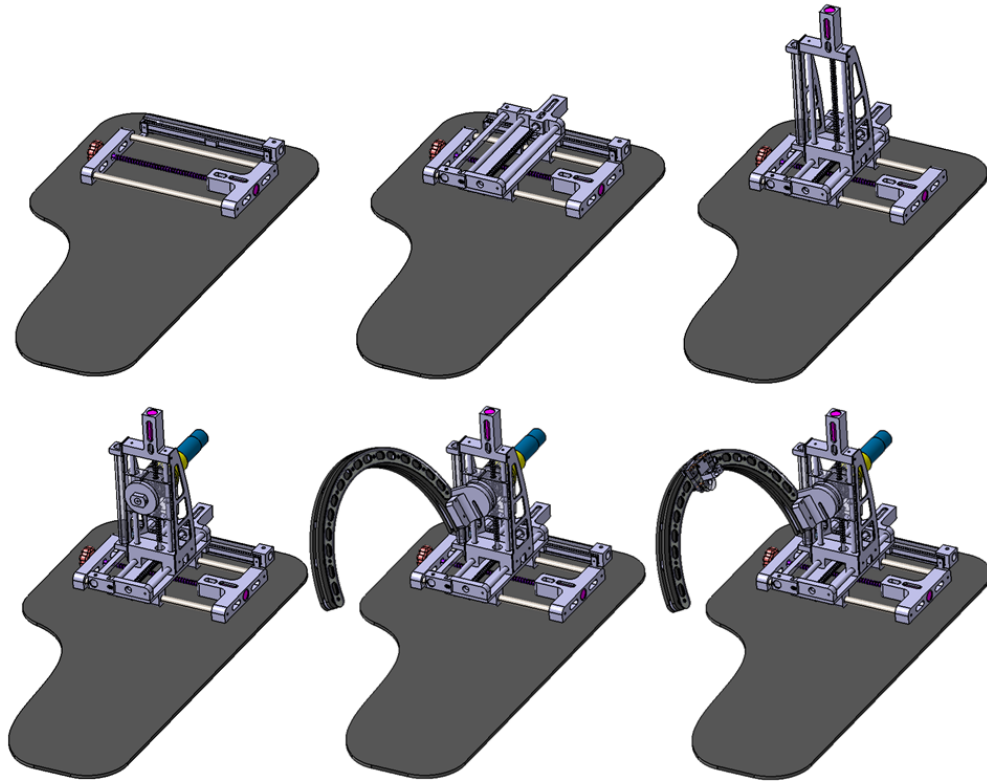
Figure 4.9: *Assembly of the kinematic chain on the ground plate of the robot.*

Note that the AD-converter as well as the MCU for the inclinometers emulate a serial interface. Hence, the robot is controlled via three serial interfaces. On the USB hub, one port remains empty for future sensors or hardware.

4.2.4 Setup

In Subsection 4.2.1, the drive trains of the rotational and translational axes were explained in detail. In this Subsection, the assembly of the kinematic chain of the robot based on the five drive trains will be discussed. Furthermore, the mobility concept of the system is explained and its setup in an application scenario is covered. As described in Section 4.2, the kinematic chain of the MARS consists of five automated axes. Figure 4.9 depicts the assembly of this kinematic chain. In the consecutive images (left to right, top to bottom), the assembly of the translational axes t1, t2, t3 (in more detail in Figure 4.2) and r1 (in more detail in Figure 4.3) are shown. In the fifth image (bottom middle) the arc structure of rotational axis r2 is mounted to the
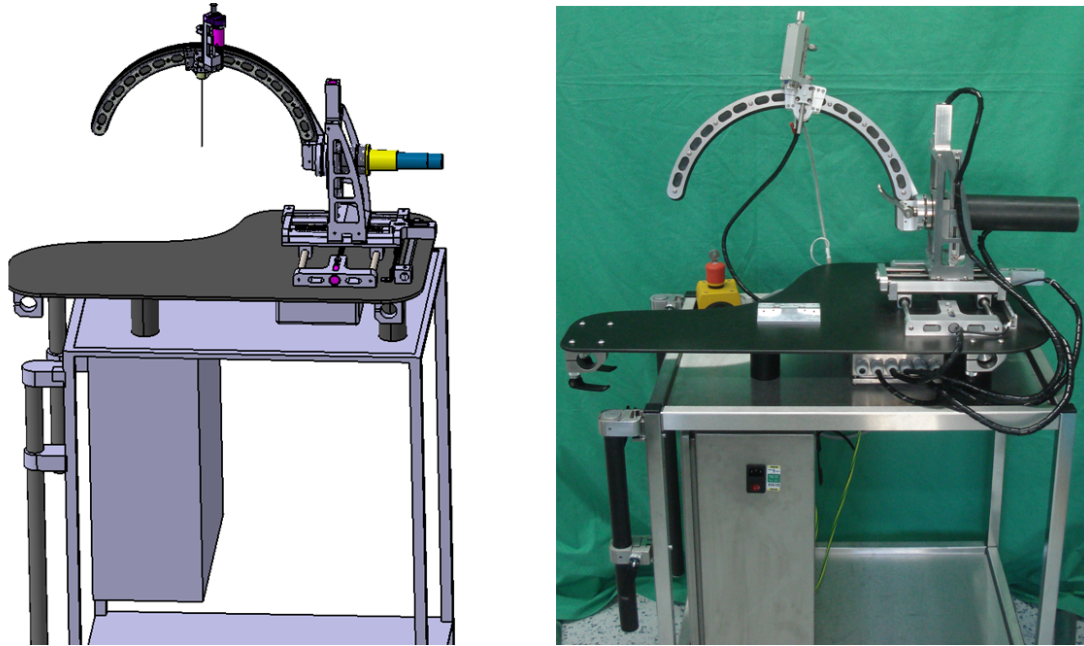
Figure 4.10: *The MARS mounted to the modified instrument table with the power electronics of the robot. The system can easily be moved by one single person.*

interface of r1. The last image shows the rotational axis r2 (in more detail in Figure 4.4) with the carriage that moves along the arc structure. The carriage provides an interface for the micro drive unit (see Subsection 4.2.6).

Beside the kinematic chain of the system, the encoders and controllers need to be assembled. The five MCBL3006s controllers as well as the AD converter and the electronics for the rotational absolute encoders are housed in the controller box (Figure 4.6). This box is mounted underneath the ground plate of the robot. The cables connecting the motors and the controllers as well as the encoder cables are shielded to suppress EMI.

As specified in Chapter 3, a highly mobile system is desirable. The design of a light-weight and application specific kinematic chain of the robot is one of two important parameters in the mobility concept. The weight of the robot is only 13 kg. Due to this feature, no additional transportation device is required. Instead, a modified conventional instrument table is used to transport the robot. It presents the second fundament of the mobility concept of the MARS system. This concept was briefly discussed in Section 4.1 and will be explained in more detail in the following.

Figure 4.10 shows the MARS on the modified instrument table. On the left, a CAD

sketch is shown, on the right the actual system is depicted. The power electronics of the robot are housed in the box on the left side of the instrument table. They are connected to the controller housing underneath the ground plate of the robot. If required, other equipment (e.g. control computer, micro electrode recording device, etc.) can be stored on the instrument table. Note that the robot is operated in this mode when outside the OT.

In the following the application scenario is described. The robot is transported into the OT using the instrument table. Next, the MARS is attached to the operating table of the OT. This is done by a special mechanism that interfaces to the side rails of the operating table. On both sides of the table, CFRP pipes are attached to the side rails. They are fastened using quick release fittings. Underneath the ground plate of the MARS system, mounting devices for the pipes are provided. Again, quick release fittings are used to ensure a rigid connection. This allows for easy mounting and unmounting of the system. The instrument table with the power electronics can be moved away from the operating table (length of the cables: 5 m).

There are three main benefits of this approach: First, the surgeon is not obstructed by the stand of the robot. Second, the robot follows the arbitrary alignment of the operating table, which is required for a number of interventions. Third, the system is compatible to almost all operating tables, as the side rails are provided by most of the manufacturers.

Figure 4.11 depicts the MARS mounted to an operating table. On the left, the CAD draft and on the right the actual system is shown.

4.2.5 Target point simulator

Safety is one key issue for a robotic positioning aid (Chapter 3). Although two independent encoders are incorporated in the MARS, faulty positioning can never be fully ruled out. Hence, a tool is desirable that independently validates the position of the probe before the intervention.

This is realized with a custom designed target point simulator, which provides additional safety for the patient. It features three mutually perpendicular and manual adjustable axes, each equipped with a scale indicating its current position. The axes are subsequently moved to the desired position. The last axis features a sharp tip indicating the target point. Once the target position is reached, the axes are locked. There are two modes to position the target point simulator: It can either be mounted
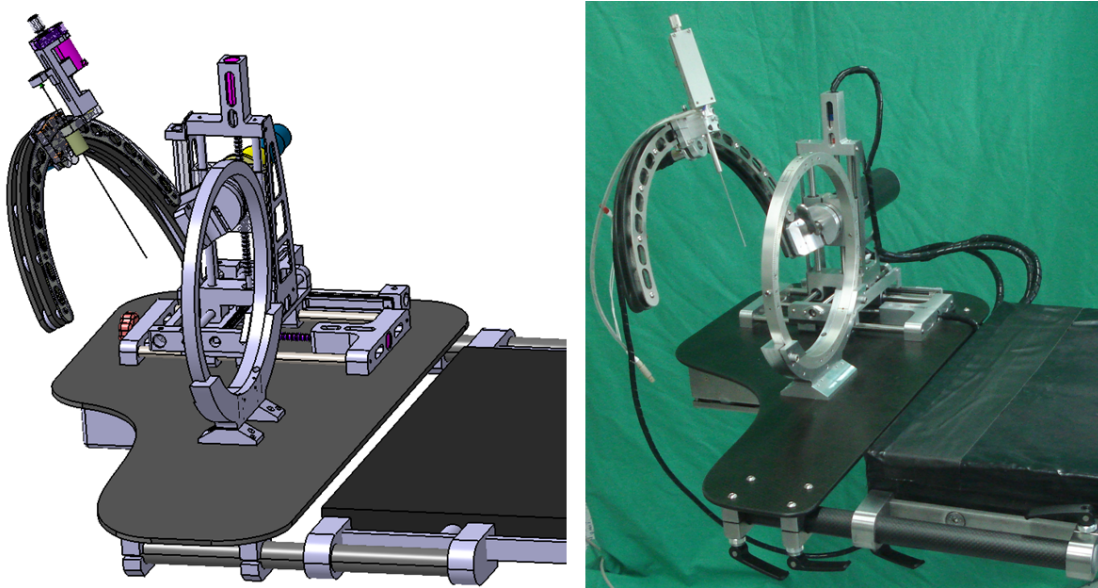
Figure 4.11: *The MARS with micro drive and stereotactic base unit mounted to the side rails of an operating table. Left: CAD draft. Right: Actual MARS.*

directly to the base unit of the stereotaxy system or to the ground plate of the robot using the fixation interface for the base unit. In both cases, no further adjustment of the scales is required. All mechanical parts are designed such, that the system can only be assembled in one way. This guarantees the correct setup of the target point simulator.

Figure 4.12 shows a CAD sketch (left) and the actual system mounted to the stereotactic base unit interface on the ground plate of the robot (right). Before the intervention, the surgeon mounts the target point simulator to one of the interfaces and adjusts its axes according to the settings provided by the surgical planning software. Then, he automatically moves the robot to the target position. Here, he validates if the target is reached. By using a target point simulator, errors in axis-assignment or typing errors during transfer of the target and entry-point coordinates are detected. Furthermore, bending of tools or probes is detected and can be corrected.

The use of the target point simulator provides the surgeon with additional confidence concerning the settings of the system prior to the intervention.
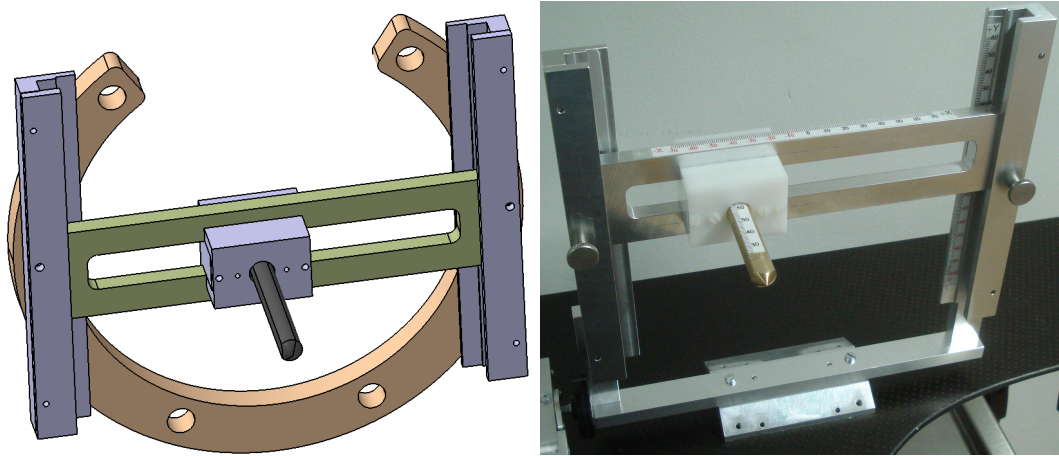
Figure 4.12: *Target point simulator. Left: Screenshot from the CAD software; Target point simulator mounted to the ceramic head ring. Right: Actual target point simulator mounted to the interface at the ground plate of the MARS.*

4.2.6 Motorized micro drive unit

So far, three translational and two rotational axes of the MARS were described, see Subsection 4.2.1. With these five axes, the probe can be positioned in an arbitrary pose. For a fully operational stereotaxy system, one additional axis is required: The axis feeding the probe into the tissue. Conventionally, manual micro drive units (MDU) are used. Figure 4.13 shows an example for such a device (inomed Medizintechnik).

The main application of MDUs are micro-electrode recordings, e.g. for DBS. The surgeon forwards the probes by turning the knob of the micro drive unit. The MDU has two manual scales to monitor the position of the probe tip: One showing the absolute insertion depth, the other indicating a relative value which is reset once the knob has completed one revolution. The smallest step width of the MDU is 50 μm.

It is of great importance, that the electrodes are located at the displayed position and that their insertation depth can be varied in small steps. Furthermore, it is desirable to have a smart system, i.e. a system that warns the user in case the probes are not positioned according to the preoperative plan.

Manual MDUs do not provide any feedback on whether a desired position is reached. This can be problematic, as the micro electrode recording computer is operated by technical staff, whereas the electrode is forwarded by the surgeon. If the two do not communicate carefully, it might lead to a misplacement of the probe.

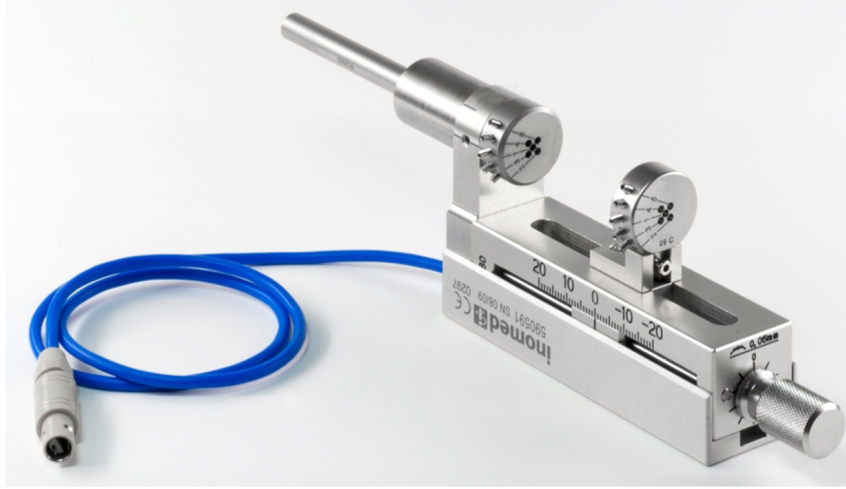An automated system can overcome most of the above mentioned problems: Continu-

Figure 4.13: *Commercially available manual micro drive unit. Image courtesy of inomed Medizintechnik GmbH.*

ous position monitoring and feedback to the user is possible. Furthermore, the system can warn the user if no-go areas are approached or other errors occur. Several commercially available fully automated micro drive systems exist, e.g. NeuroNav Drive from AlphaOmega Co., USA [107].

Compatibility with equipment of the industrial collaborator is aimed for in this project, so the existing micro drive unit of inomed Medizintechnik GmbH was motorized. The motorized micro drive unit is an independent stand-alone system. It can be used to upgrade manual stereotactic frames or in conjunction with the MARS.

First, a brief overview over the requirements is given. Next, the realization of the motorized micro drive unit is described. Furthermore, an intelligent end switch is presented, that ensures that a preoperatively selected depth limit for the electrodes can not be exceeded.

4.2.6.1 Requirements

Summarizing, the following requirements for a motorized micro-drive unit were identified:

- **Accuracy:** The positioning of the carriage should be as accurate as possible. The smallest step width of the MDU should undercut that of currently used manual systems ($\leq 50 \ \mu m$).

- **Compatibility:** The new device needs to be fully compatible with the interfaces of the manual MDU. Furthermore, to facilitate the transition from manual to motorized surgery, the design of the manual MDU should be retained.

- **Sterilization:** The MDU is in direct contact with the patient and therefore needs to withstand steam sterilization at 134° centigrade and 2 bar pressure.

- **Operating modes:** Just like the MARS, the motorized micro drive unit is required to provide manual and automatic positioning modes. A switching between the two modes should be possible.

- **Safety:** The position of the carriage of the MDU needs to be monitored by two independent encoders. The power of the drive has to be limited in a way that the MDU is stoppable by hand at all times and without exerting great forces or torques. After a stop of the MDU, the surgeon should be able to manually continue his work. The carriage must not exceed a preoperatively defined final limit.

4.2.6.2 Realization

As defined in the requirements, the motorized micro drive unit is based on manual system. This ensures compatibility to currently used interfaces. Figure 4.14 shows the newly developed system. To drive the carriage, a sterilizable brushless DC motor (2036T024B-K1000) in combination with an MCBL3006s is used. The properties of the motor and the controller are given in Subsection 4.2.1 and Subsection 4.2.2.

In contrast to the drive trains of the MARS, a custom-designed, sterilizable gear is used: A pinion (d = 6 mm, 11 teeth) is directly mounted to the shaft of the motor. It meshes with a cogwheel (d = 21.5 mm, 43 teeth) that is fixed to the spindle of the MDU. Both, pinion and cogwheel are made of sterilizable steel. Together, they form a gear with a ratio **g** of $\mathbf{g} = \frac{43}{11} = 3.91$.

The rotation of the motor is transferred via the gear to the spindle of the MDU. The spindle-nut combination transforms the rotation in translational movement of the carriage. One revolution results in a translational movement of 0.5 mm. Note that the spindle of the MDU can still be manually manipulated by turning the knob attached to its far end (Figure 4.14, bottom right).

The position of the motor shaft is monitored with 3000 counts per revolution by the MCBL3006s controller. DBS electrodes and other probes are fixed to the carriage of
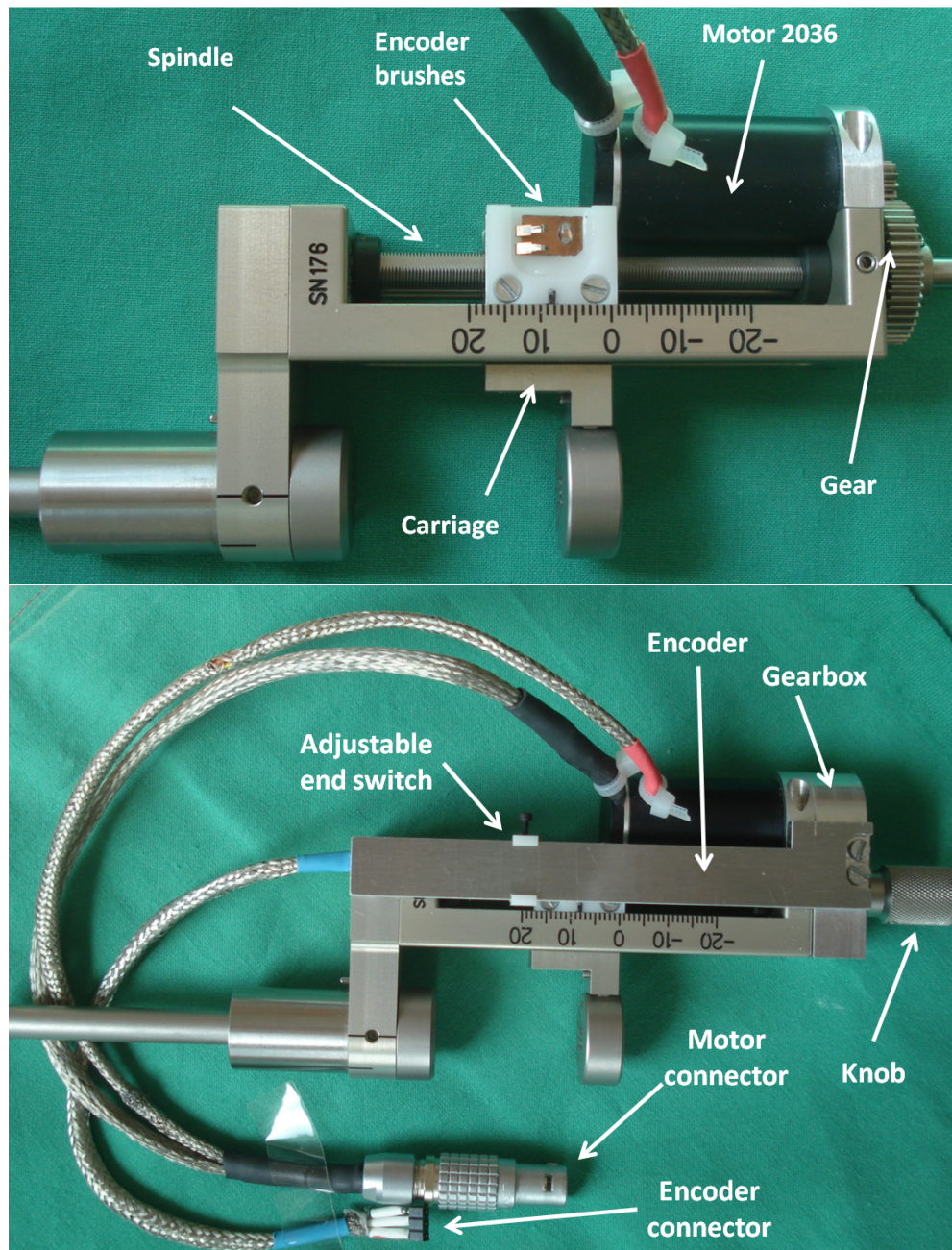
Figure 4.14: *Motorized micro drive unit. Top: Encoder not mounted to show electronics. Bottom: Encoder and gearbox mounted.*
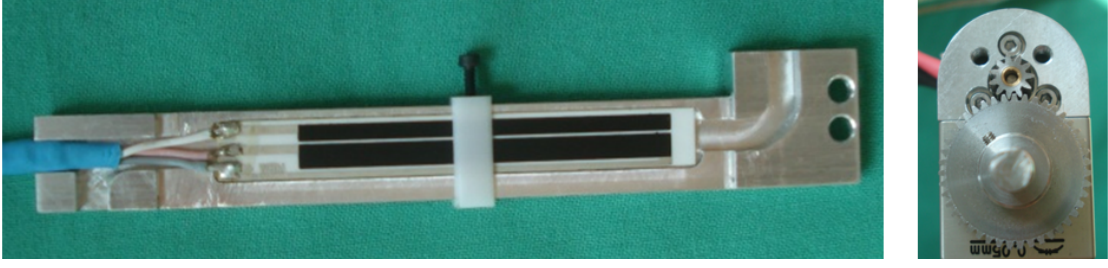
Figure 4.15: *Left: Absolute encoder based on an MBW potentiometer of the motorized micro drive unit with the adjustable barrier (white plastic). Right: The gear of the micro drive unit consists of the pinion on the motor shaft and the cogwheel on the spindle.*

the MDU, hence the accurate positioning of the carriage is essential for the overall accuracy of the device. For this reason the second encoder directly monitors the position of the carriage.

As for the translational axes of the MARS, an MBW potentiometric encoder is used. The wiper of the potentiometer is attached to the carriage of the MDU (Figure 4.14, top). The second part of the potentiometer, the tracks with the wires (Figure 4.15), are fixed to the MDU (Figure 4.14, bottom).

The theoretical position resolution, which is equivalent to the smallest step width of the carriage, can be calculated as follows:

$$\mathbf{r_{controller}} = \frac{spindle\ pitch}{counts\ per\ revolution \times gear\ ratio} = \frac{0.5\ mm}{3000 \times 3.91} = 0.426\ \mu m \tag{4.9}$$

In contrast to the drive train of the translational axes (Section 4.2.1), no ball-screws are used in the MDU for spatial limitations. As a result, backlash occurs at the screw-nut interface. On the other hand, the backlash from the gear is negligible because only two cog wheels mesh and because the gear only consists of one stage.

For the secondary absolute encoder, the calculations of Equation 4.8 are adapted: The maximal travel distance of the MDU is 45 mm. The same AD converter as for the three translational axes of the MARS is used. With an AD converter resolution of 12bit (HB627 USB, H-Tronic GmbH Germany [105]) the position resolution of the system is given by:

$$\mathbf{r_{encoder}} = \frac{45\ mm}{2^{12}} = 0.011\ mm = 11\ \mu m \tag{4.10}$$

Table 4.4: *Motor and gear of the motorized micro drive unit; The specification of motor, gear ratio, and resulting theoretical positioning resolutions at no load are given.*

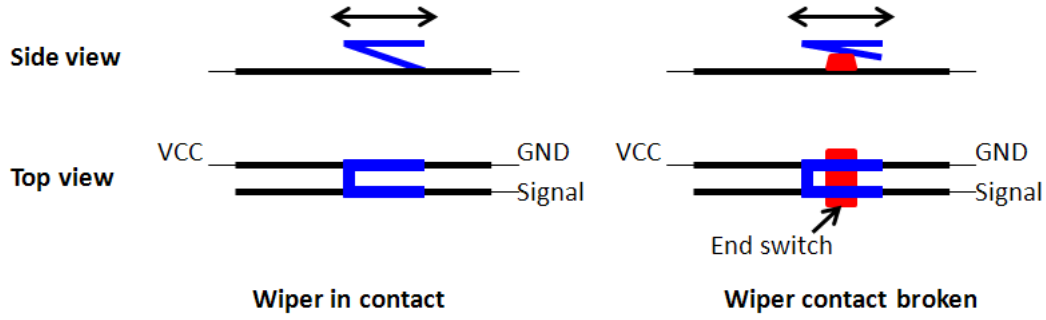| Axis	Motor	Gear ratio	Controller resolution	Encoder resolution
t4	2036T024B-K1000	3.91	$0.426~\mu m$	$11~\mu m$

Figure 4.16: *Functional principle of the end switch. Left: Regular operating mode. Right: Wiper of the potentiometric encoder looses contact to the tracks of the potentiometer after hitting the plastic barrier.*

Note that the same mechanisms to enhance the accuracy of the absolute encoder as described in Subsection 4.2.3 are applied.

Two operating modes are available: Manual and automatic. If the user wishes to stop the MDU in case of emergency, he can do so by simply holding the knob. This interaction will cause a raise in current consumption which is detected by the control-software. Next, the amplifiers of the controller will be deactivated. The user can continue the intervention in the manual operating mode.

Table 4.4 summarizes the properties of the motorized micro drive unit. In the context of MARS, the MDU is labeled **t4**, as it represents the forth translational axis of the system. Note that the given resolutions are only theoretical values. Several error sources, e.g. backlash, are not considered in this calculation.

As discussed in Chapter 3, automatic movement of axes poses a potential danger for the patient. Furthermore, surgeons often do not trust safety features that are solely implemented in software. For this reason, an adjustable electro-mechanical end switch was developed and realized. It presents an additional safety feature of the motorized MDU. Its functional principle, the design and the realization will be discussed in the following.

The functional principle of the end switch is shown in Figure 4.16: The wiper of the MBW potentiometer is shown in blue. It can be moved sideways along the conductive track (black). The resistive element is connected to VCC on one side and to GND on the other. The signal voltage is dependent on the position of the wiper. As shown in Figure 4.14, top, the wiper of the potentiometer is fixed to the carriage of the MDU. In the end switch, this signal voltage is used for an additional purpose. An adjustable plastic barrier is attached to the encoder housing at an arbitrary position. The position defines the limit for the travel range of the carriage. If the wiper hits the plastic barrier, the brushes will be lifted off the tracks and the contact will be broken (Figure 4.16, right). This breakage is detected by a sensor that then disables the controller of the motor. As a result, the motor will stop immediately. In Figure 4.15 the movable barrier (white) on the tracks of the encoder is shown.

Figure 4.17 shows the actual system. On top, the wiper of the potentiometer is shown, below the tracks of the potentiometer. The left side visualizes the regular operating mode, the right side shows the system after hitting the end switch. In the close up (bottom), the brushes of the wiper are depicted. First, they are in contact with the tracks (left). After hitting the barrier, the contact is broken and the movement is stopped (right).

This signal loss is detected by a custom designed circuit. Its main component is a relay that is switched by the signal voltage. The power for the MCBL3006s motor controller is regulated by the relay. If the brushes of the wiper are in contact, the relay is activated and allows current to pass through. If the connection between wiper and track is broken by the plastic barrier, the relay is deactivated and the current for the motor controller is cut. Hence, the motor stops moving immediately.

Figure 4.18 shows the populated PCB designed for the end switch (length×width = $22{\times}18$ mm^2). It features connectors to a 24 V power supply that is forwarded to the MCBL3006s once the relay is activated. Furthermore, two headers for the encoder are provided: One is connected to the potentiometer (encoder in) and the second is connected to an external AD converter (encoder out). Note that the AD converter provides the voltage for the potentiometer. Three status LEDs indicate if the power supply is connected, if the encoder voltage is provided and if the supply voltage is forwarded to the MCBL3006s.

The developed motorized micro drive unit presents an accurate tool for positioning of probes. It is fully compatible to standard equipment and, thanks to its custom design gear, sterilizable without constraint.
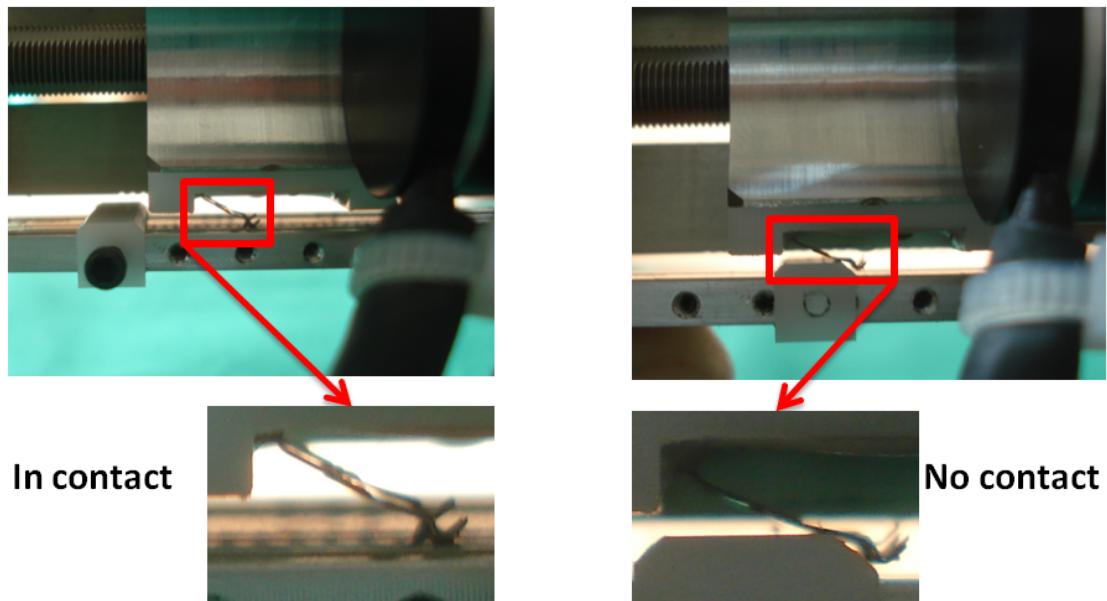
Figure 4.17: *Functional principle of the end switch: Left, the brushes of the encoder are in contact. Right: After hitting the end switch, the brushes are lifted and the contact is broken.*
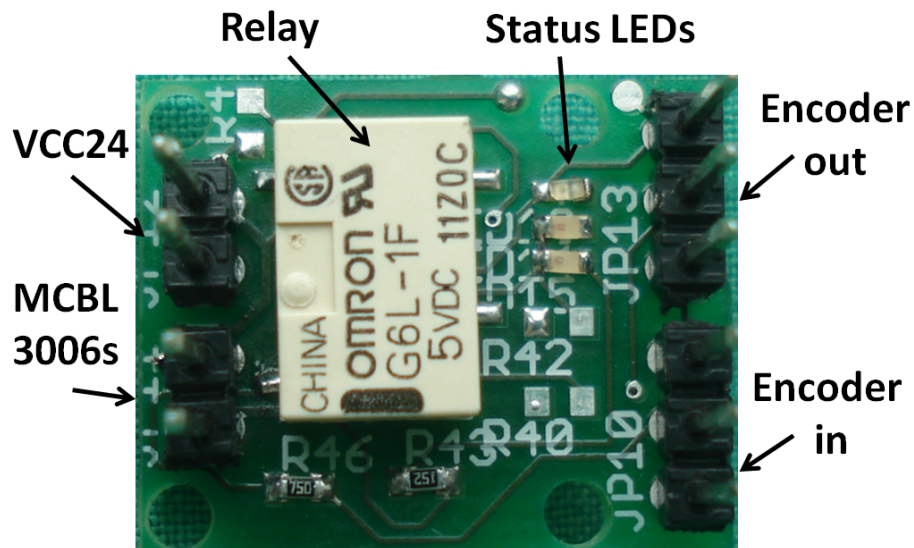

Figure 4.18: *End switch PCB with interfaces to VCC24, MCBL3006s and the potentiometric encoder. A relay is used to control the supply voltage of the MCBL3006s motor controller. When the wiper of the potentiometer reaches the end switch, the supply voltage for the controller is interrupted.*

Two operating modes exist: automatic and manual positioning. With two independent position encoders, one being an absolute encoder, accurate and redundant monitoring of the carriage position is possible. As an additional safety feature, an electro-mechanic end switch was developed. To conclude, the presented system fulfills the previously defined requirements.

4.3 Control

This section outlines the control framework and software of the MARS. All software is written in Java (Oracle Corporation, USA) which makes the software operating system independent.
The section consists of three parts: The general concept of the software, the calibration of the absolute encoders and further features of the software.

4.3.1 General

The software of the MARS needs to provide the following functionalities:

- Adjustment of robot settings

- Trajectory execution

- Intraoperative robot control

- Status monitoring

The control of the MARS consists of two layers: The first layer is given by the software running on the control PC, the second layer by the control algorithms running on the MCBL3006s axes controllers.
The software of the MARS is a multi-thread application. Each of the five axes is controlled by a separate thread, further threads manage the overall control of the robot and the GUI. For each axis, a great number of parameters can be adjusted in the GUI. The most important ones are:

- Maximal speed

- Maximal acceleration

- Maximal continuous current

- Maximal peak current

- Upper/Lower position bound

Remember that the torque of the motor shaft and with it the maximal force that the robot exerts on obstacles is dependent on the current the controller provides. By limiting the current, also the potential danger of the robot is reduced.

The axis threads communicate with the MCBL3006s units and manage the user interaction. In the software, the parameters for the MCBL3006s units, e.g. target position, position bounds, speed and current limits are specified. Then they are transferred to the controllers. All axis threads communicate with their controllers via one single COM port (Figure 4.8).

The software provides a safety routing that monitors the consistency of the positions of the axes. Therefore, the position information of the absolute encoders is compared to the information from the MCBL3006s controllers. The amplifiers of the axes are automatically disabled, if a positioning error is detected or if the current consumption is too high.

Each of the five MCBL3006s units features a proportional-integral-derivative (PID) controller for the position of the motor shaft. The parameters for the controller can be set via the software. The MCBL3006s unit ensures that the shaft is moved to the target position defined in the software and that it holds its position in the case of disturbances. The controller is the key-component for the positioning of the automated axes.

Furthermore, the current consumption as well as other parameters, e.g. controller temperature are monitored. The controllers monitor that the specified maximal parameters are not exceeded. This ensures that, even if the connection between the software and the controllers is lost, a minimum of safety is guaranteed.

Figure 4.19 depicts the control schema of the MARS. A control GUI transfers the user's commands to the threads of the axes. Based on the user commands, the parameters for the software and for the controllers are determined. After that, the corresponding commands are transferred to the controllers via the COM port. The parameters for the control layer running on the MCBL3006s unit are adjusted according to the commands. In regular intervals, information about the current status of the controller is polled by the software. Figure 4.19 shows only one of the five threads for the axes fully explained, as the other four are similar.
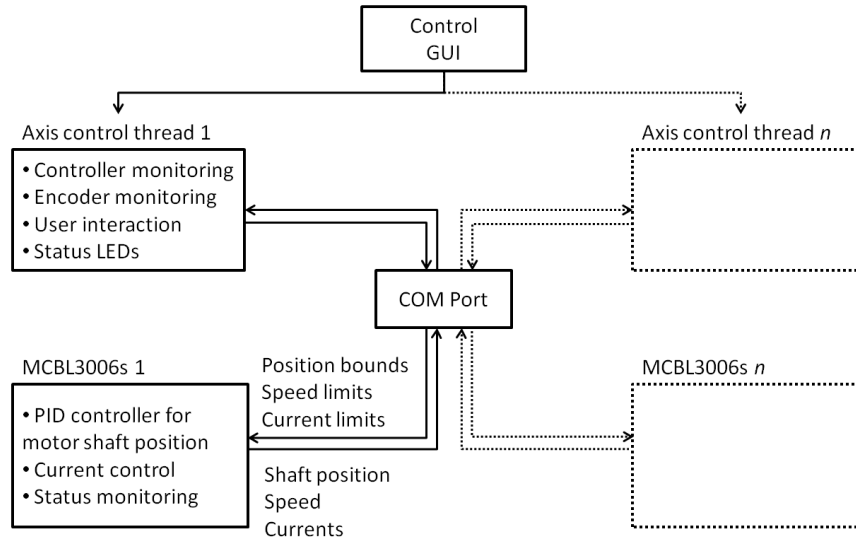
Figure 4.19: *Two layer control schema of the MARS: First, an axis control thread determines and monitors the parameters of the axis. Second, the MCBL3006s unit control loop monitors the compliance of the axis with the set parameters.*

4.3.2 Encoder calibration

For the above described control schema, a reliable secondary absolute position encoder is required for each of the five axes. As discussed in Subsection 4.2.3, the encoders for the translational axes require a calibration in order to provide highly accurate data. This calibration is described first. After that, the possibility to set an initial offset for the rotational encoders is explained.

The linearity tolerance of the encoders is specified with >1%, their resistance tolerance with 20% [104]. These facts necessitate a calibration algorithm for the absolute encoders which is integrated into the software. The main idea of the algorithm is to sample the whole travel range of the encoder with a number of discrete steps and later use the collected data to determine the position of the axis.

Therefore the user defines the number of steps for the discretization of each axis. The following procedure is executed for all selected axes. The robot automatically moves the axis to its bounds. There, the AD converter is queried. Note that averaging is used to minimize the noise and that the relative voltage is determined to minimize the effects of voltage fluctuations (see Subsection 4.2.3). After this, the axis is moved one step and again the AD converter is queried. This procedure is repeated until the bound of the axis is reached. The resulting data is stored in a lookup table.
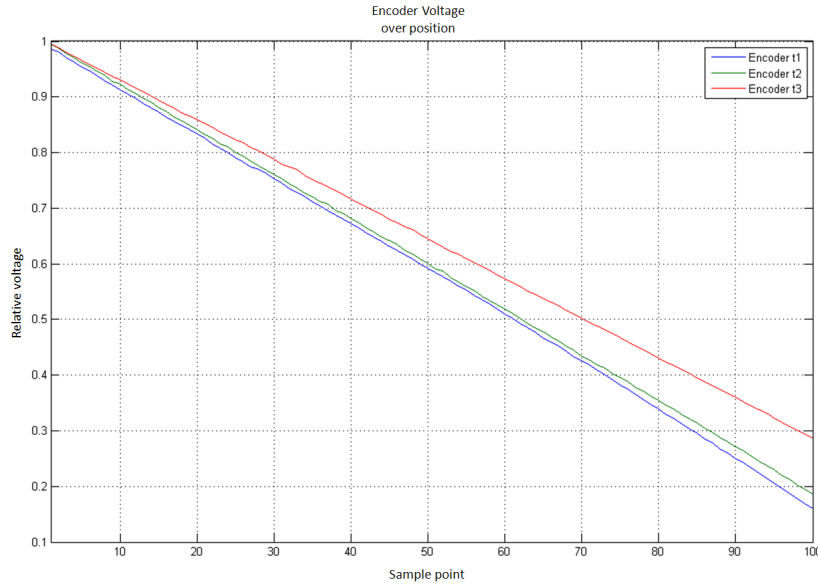
Figure 4.20: *Relative encoder voltage over the position of the axis. Here, 100 points were approached to obtain a calibration. This encoder type is used in translational axes t1, t2, t3 and the micro drive unit.*

Figure 4.20 shows the collected values during an exemplary calibration with 100 steps. The Y-axis shows the relative voltage at the sampled point. Although all three potentiometric encoders have the same nominal value of 10 kΩ, the three plotted lines are not parallel. This is due to the fact that the absolute value tolerance is 20%. Furthermore, inaccuracies in the liniarity are visible (for example between sample point 35 and 40, green). The calibration algorithm compensates for both error sources.

To obtain the position data, the AD converter is queried. The resulting relative voltage is compared to the data of the lookup table. Linear interpolation is used to provide continuous position values.

For the rotational axes, two SCA-100T inclinometers are used to determine the absolute position (see Subsection 4.2.3). One is located in the controller box, the other one is attached to the carriage of r2. The difference between the angular values from the two inclinometers is used to monitor the position of the rotational axes r1 and r2. To account for mounting inaccuracies, the user can specify an initial offset between the two inclinometers. No further calibration is required.

With the calibration of the absolute encoders, reliable and redundant position information for each axis is available. It is processed in the software to ensure the correct behavior of the robotic system.

4.3.3 Miscellaneous

Note that the software automatically loads the last known configuration. After closing the application, a new configuration file containing the current settings is created. Furthermore, there are hard-coded default values in case no configuration file was found.

A server for the MARS was developed. It provides an interface inspired by the robot server framework described in [108]. Here, basic robot commands, e.g. positioning of axes, are capsuled. The user only needs to start the server and can interact with the robot via TCP. This facilitates the integration of the robot in an existing software framework, e.g. the PraezisPlus surgical planning software (TatraMed spol. s r.o., Slovakia). Furthermore, it allows for easy adaptation to new problems without the need to modify the main software of the robot.

In this Subsection, the basics of the software were described. In the next Section the mathematical fundamentals for more advanced features, the kinematic calculations, will be discussed.

4.4 Kinematics

The description of the kinematics of the MARS is a prerequisite for the alignment of the end-effector (i.e. probe) with a previously planned pose. In the actual application, the target pose is determined by the entry and target point specified by the surgeon. The kinematic calculations to reach the target are discussed in the following. Thanks to the alignment of the axes as a center of arc system, the kinematic calculations are straight forward (see Section 2.2).

In stereotaxy, the base coordinate system is defined by the human skull: The X-axis is defined from left to right from a patient's point of view (transversal), the Y-axis from the back to the front of the head (sagital) and the Z-axis from the feet to the head (vertical). The alignment of the MARS coordinate system, shown in Figure 4.22, follows this definition. The origin is at the intersection of the centers of rotation of **r1** and **r2** (center of arc). The direction of motion for the six axes is indicated with double headed red arrows.

In this section, first the forward and inverse kinematic are discussed. After that, a method to determine the transition between the coordinate systems of the robot and the stereotactic base unit is presented. Next, the accuracy of the kinematic chain is
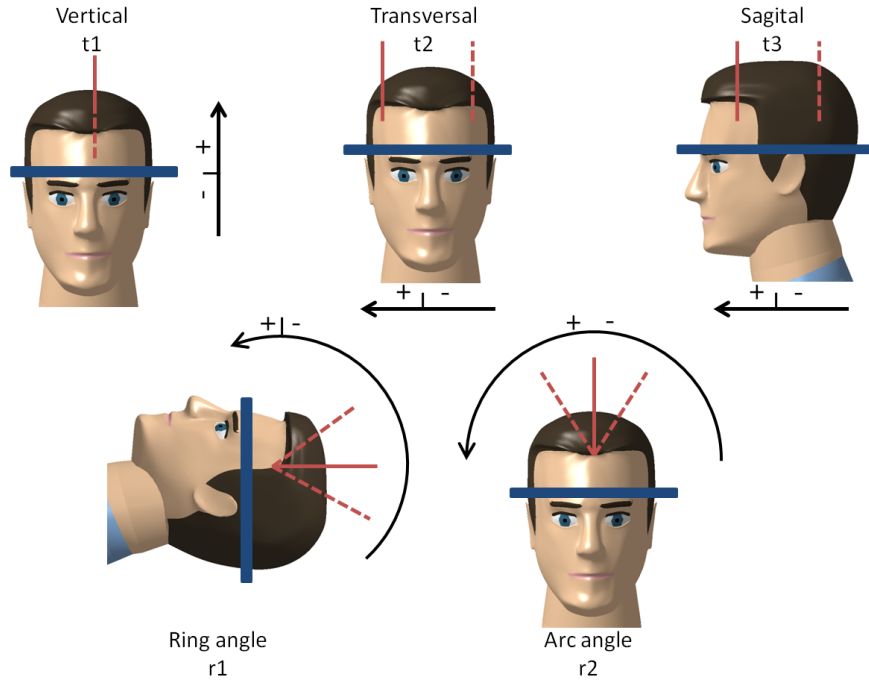
Figure 4.21: *Axes nomenclature of the MARS robot with respect to the head of the patient.*

analyzed in detail, as this is of great importance for the application of the system. At the end of the section, a calibration method based on the results of the previous analysis is presented.

4.4.1 Forward calculation

Starting with a known position of the axes, the pose of the end-effector of the robot is calculated using the forward kinematics. It is based on the Denavit-Hartenberg (DH) rules [109] and related to the calculations presented by Ramrath et al. in [110]. The DH convention allows the calculation of the end-effector pose based on the positions of the five axes (**t1, t2, t3** translational axes; **r1, r2** rotational axes). Beside these automated axes, a (manual or motorized) micro drive unit is used to feed the probe into the brain. This axis is labeled **t4**. Figure 4.22 gives an overview over the automated axes and their motion directions.

The special design of the serial kinematic chain as center of arc system allows one important simplification of the DH parameters. Usually, the base coordinate system S_0 of the serial chain aligns with the Z-axis of the first axis (here **t1**). This is not
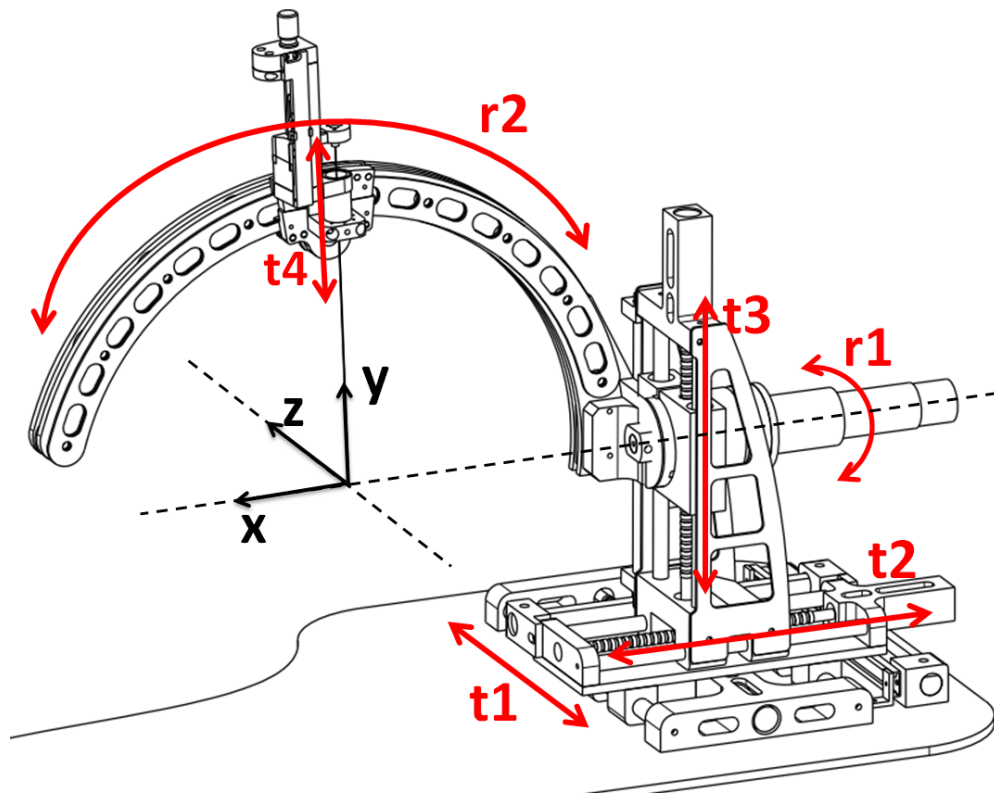
Figure 4.22: *Schematic view of the kinematic chain of the MARS. The direction of motion for the six axes is indicated with double headed red arrows. Furthermore, the origin of the robotic coordinate system is depicted.*
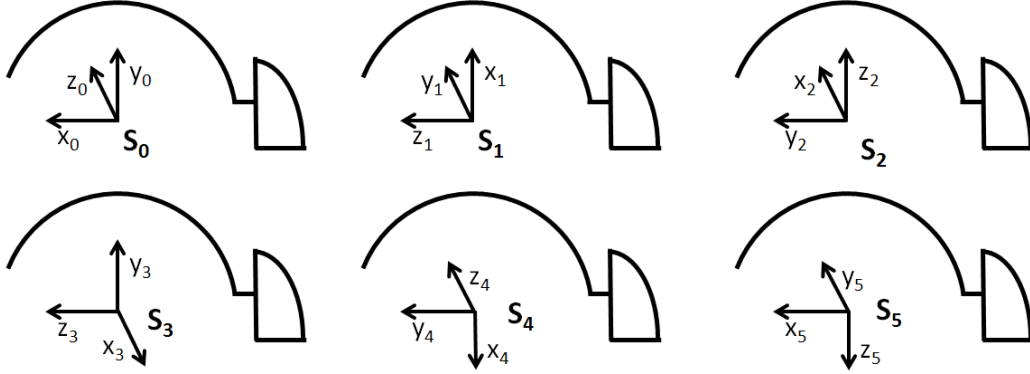
Figure 4.23: *Kinematic forward calculation: Coordinate systems of the MARS in accordance with the Denavit-Hartenberg convention.*

Table 4.5: *Denavit Hartenberg parameters for the MARS. Active joint parameters are indicated with a star (*).*

Axis	a_i	d_i	τ_i	α_i
0	0	$t1*$	0	0
1	0	$t2*$	$\frac{-\pi}{2}$	$\frac{\pi}{2}$
2	0	$t3*$	$\frac{\pi}{2}$	$\frac{\pi}{2}$
3	0	0	$r1* + \pi$	$\frac{\pi}{2}$
4	0	0	$r2*$	$\frac{-\pi}{2}$
5	0	$t4 * + l_{tooldiff}$	$\frac{\pi}{2}$	$\frac{\pi}{2}$

the case in the adapted calculations. The combination of the translational offsets introduced by the a_i and d_i parameters in the DH table equals the inverse of the initial offset between the stereotactic CoS (with corresponding origin in the center of the ring) and the base CoS of the kinematic chain. In stereotaxy, the positions are given with respect to the stereotactic CoS. Thus the offsets a_i and d_i do not need to be considered in the kinematic calculations.

The simplified parameters of the forward calculation are presented in Table 4.5. The active joint parameters are indicated with a star (*). Figure 4.23 shows the coordinate systems $\boldsymbol{S}_0 - \boldsymbol{S}_5$ used in the calculations.

Please note that all coordinate systems share the same origin. This fact is represented in Table 4.5: The translational contributions a_i and d_i equal zero except for the active translation joint parameter **t1**–**t4**.

For each axis, a homogeneous matrix describing the transition $_i^{i+1}\boldsymbol{S}$ between two con-

secutive coordinate systems is determined. The following matrix ${}_0^5\boldsymbol{S}$ gives the results for the composition of the six coordinate transformations (with s - sine, c - cosine):

$${}_0^5\boldsymbol{S} = \begin{bmatrix} s(r2) & 0 & -c(r2) & -c(r2)(t4 + l_{tooldiff}) - t2 \\ -c(r2)s(r1) & -c(r1) & -s(r1)s(r2) & -s(r1)s(r2)(t4 + l_{tooldiff}) - t3 \\ -c(r1)c(r2) & s(r1) & -c(r1)s(r2) & -c(r1)s(r2)(t4 + l_{tooldiff}) + t1 \\ 0 & 0 & 0 & 1 \end{bmatrix}$$

$$(4.11)$$

Figure 4.21 shows the movement of the five automated axes with respect to the head of the patient. It illustrates the positive and negative movement directions for each axis.

In regular operation mode, the parameter **t4** equals zero once the target pose is reached. This assumes that the tool length $\boldsymbol{l_{tool}}$ equals the working distance $\boldsymbol{l_{work}} = 190\ mm$ of the system (see 3). In that case, the offset parameter $\boldsymbol{l_{tooldiff}}$ equals zero:

$$l_{tooldiff} = l_{tool} - l_{work} = 0 \tag{4.12}$$

If $l_{tooldiff} \neq 0$, the forward kinematics can still be solved and the pose of the robot can be determined. However, $l_{tooldiff} \neq 0$ causes problems for the inverse kinematics discussed next.

4.4.2 Inverse calculation

In the inverse kinematic calculations, the parameters for the axes are derived from a desired target pose. Equation 4.11 gives the forward kinematics of the system. As the system provides only five DOF, not all poses can be reached. This limitation is visible at **S[1,2]** which is equal to zero. However, it has no effect in the application, as rotational symmetric probes are used and the missing DOF would rotate about the symmetry axis.

From the matrix ${}_0^5\boldsymbol{S}$, the parameters for the two rotational axes **r1** and **r2** can be

derived directly:

$$
\begin{aligned}
r1 &= atan2\left(\frac{{}_0^5 S[3,2]}{-{}_0^5 S[2,2]}\right)\\
r2 &= atan2\left(\frac{{}_0^5 S[1,1]}{-{}_0^5 S[1,3]}\right)
\end{aligned}
\tag{4.13}
$$

If the tool length l_{tool} differs from the working distance of the system of 190 mm, $l_{tooldiff}$ introduces a disturbance in the translational part of matrix S.

This needs to be compensated by $t4$. This fact is represented in the forth column of the matrix S: In regular operation, $l_{tooldiff}$ and $t4$ equal zero when the target is reached. If, however a probe with working distance other than 190 mm is used, $l_{tooldiff}$ changes and $t4$ needs to compensate this length difference. Note that this is the case center of arc kinematics. After compensation of the difference, the target pose S_{target} can be calculated as follows:

$$
S_{target} = \begin{bmatrix}
s(r2) & 0 & -c(r2) & -t2\\
-c(r2)s(r1) & -c(r1) & -s(r1)s(r2) & -t3\\
-c(r1)c(r2) & s(r1) & -c(r1)s(r2) & +t1\\
0 & 0 & 0 & 1
\end{bmatrix}
\tag{4.14}
$$

The parameters for the translational axes $t1$, $t2$ and $t3$ can be derived from this equation. Here, the advantage of the center of arc system becomes visible: The translational and the rotational part of the pose S_{target} are decoupled. Hence, the target position is specified only by the translational axes and the orientation by the rotational axes. The two rotational axes can be adjusted by the surgeon without changing the translational target.

Note that in center of arc kinematics, the translational part of the target pose always matches the center of arc. This enables the kinematic calculations described above. The given inverse kinematics allows for the targeting of arbitrary poses in the workspace of the robot. It is implemented in the software of the robot.

4.4.3 Referencing

As discussed in Section 2.1, the transition between the robot CoS and the stereotactic device CoS need to be determined in order to correctly position the probe. The
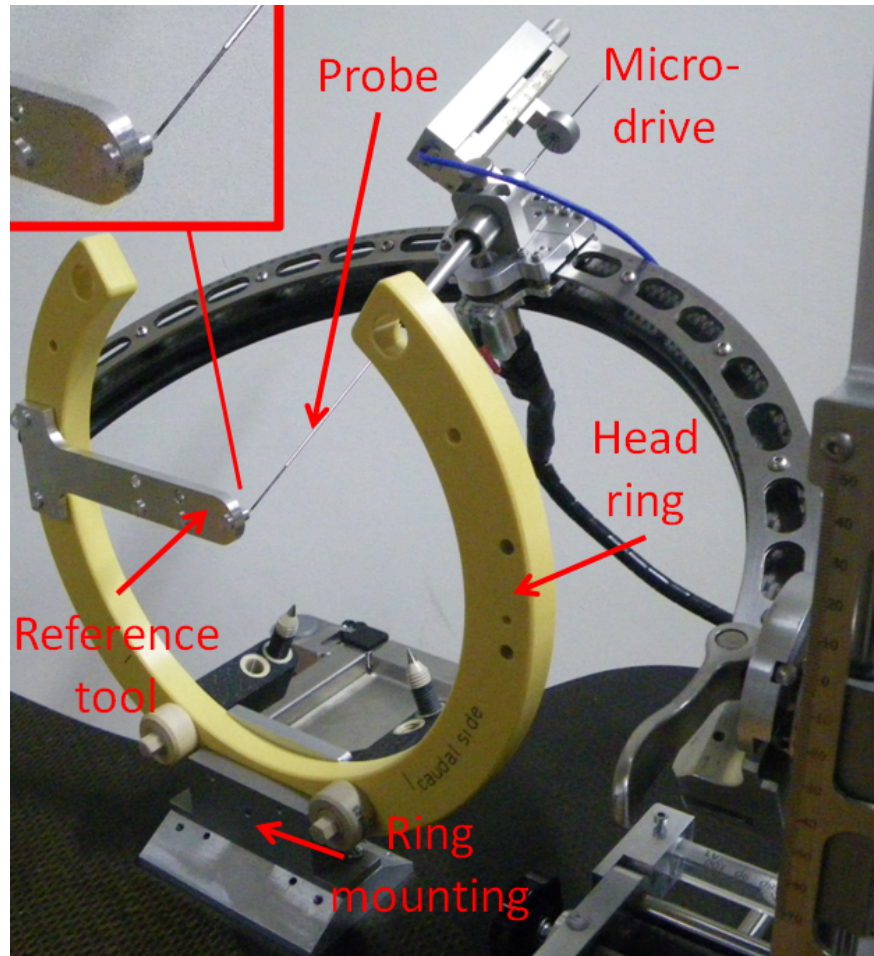
Figure 4.24: *Reference tool to determine the transition between the coordinate systems of the robot and the stereotactic base unit.*

knowledge of the kinematic calculations and the transition between the CoSs enable a positioning of the probe with respect to the stereotactic device CoS.

When a new probe or new stereotactic base unit (e.g. a head ring) is used for the first time, the user needs to define a new reference position for the robot. This position represents the origin of the robot coordinate system (see Figure 4.22). The mounting of the base unit is chosen such that the axes of the stereotactic base unit align with the translational axes of the robot. Hence, no angular correction is required.

A reference tool, compatible to the ceramic and aluminum stereotactic base unit of inomed Medizintechnik GmbH, has been designed. It indicates the origin of the base unit.

The following procedure is used to determine the transition: First, the axes of the robot are moved to their physical bounds and the relative position counter of the MCBL controllers are reset. Next, the ring is attached to the mounting and the reference tool is fixed. Then, the user moves the robot until the tool-tip matches the tip of the reference pin. Last, the traveled distance from the bounds to the tip of the reference pin is queried from the controller and saved in the configuration file of the robot (see Section 4.3). The GUI includes a panel that guides the user through the procedure step-by-step.

Figure 4.24 shows the reference tool attached to the ceramic ring. The ceramic ring in turn is attached to the mounting on the ground plate. The probe with a length equal to the working distance of the robot (190 mm) is attached to the micro drive unit. On the upper left corner, a close-up of the probe tip and the pin of the reference tool is shown.

All subsequent planning is based on this origin of the coordinate system and given with respect to this position. Thanks to the reference tool and the presented procedure, new instruments, probes and head rings can easily be integrated into the MARS.

4.4.4 Kinematic chain

The MARS is designed to be a center of the arc system. However, the actual system is subject to errors. Regarding the MARS, the most important error-source is the deflection of the arc by gravity due to movement of the rotational axes r1 and r2 with attached load (micro drive unit).

The arc (as well as other structural parts) are made of carbon-fiber reinforced plastic. It has an anisotropic Young's Modulus which causes position dependent bending of the arc [111]. A second important error source is the misalignment of the axes with respect to each other. Further minor error sources exist, e.g.: friction, temperature dependent mechanical properties or gear box elasticity [112].

In order to determine the accuracy of the robot, the two main error sources deflection and misalignment are analyzed. If the alignment of the axes to each other is mistakenly considered perpendicular, the kinematic calculations presented in Subsection 4.4.1 and 4.4.2 yield faulty results. As a consequence, the probe is not positioned correctly. The minor error sources are neglected in this first examination.

The results of this analysis present the starting point for the development of a calibration algorithm in Subsection 4.5.

For center of the arc systems it is of utmost importance that all rotational axes intersect in exactly one point. This is illustrated in Figure 4.22: The center of rotation for axis r1 and r2 (indicated with dotted lines) intersect in one point, the center or arc.

The angles for r1 and r2 are labeled α and β. The vectors **t1**, **t2**, **t3**, **t4**, **r1** and **r2** label the direction of motion for the translational axes and the center of rotation for the rotational axes, respectively.

4.4.4.1 Methods

The first goal of the analysis is to find the centers of rotation **r1** and **r2** for axes r1 and r2. Furthermore, the directions of motion **t1**, **t2** and **t3** for the translational axes t1-t3 need to be determined. Once these five vectors are known, the angles between them are calculated. This yields information about the alignment of the axes of the system. The second goal of the analysis is to determine the deflection of the arc caused by movement of the r1 and r2 axes.

An optical tracking camera is used to analyze the influence of the deflection and other error sources on the accuracy of the system. Figure 4.25 shows the experimental setup: An active marker was attached to the micro drive unit which in turn was mounted to the interface at r2. The accuTrack250 (atracsys LLC, Switzerland) tracking camera was used to log the position of the marker at 80 Hz. The accuracy of the camera is dependent on the distance between camera and marker (here under 1 m) yielding an RMS error of around 0.1 mm [113]. A control PC saves the position information from the camera and controls the robot.

The robot was moved to the start position (α= -45°, β= -45°). Three measurements labeled (A), (B) and (C) were conducted.

In measurement (A), the translational axes t1-t3 were moved subsequently from their origin to the bounds and back. The positions were logged by the tracking camera. This yields information about the relations between the translational axes.

In measurement (B), r2 was moved from β= -45° to β= +45° and then back to its initial position of β= -45°. After that, the r1 axis was moved by 10° from α= -45° to α= -35°. Next, axis r2 was again moved in the previously described manner. This was repeated until the r1 axis had reached its final position of α= +45° yielding a total of ten datasets. Figure 4.26, top, illustrates the procedure: The arrows next to r2 indicate that the axis is moved in both directions. The dotted arrow next to r1 indicates a stepwise movement in one direction only. Two arbitrary positions of r1
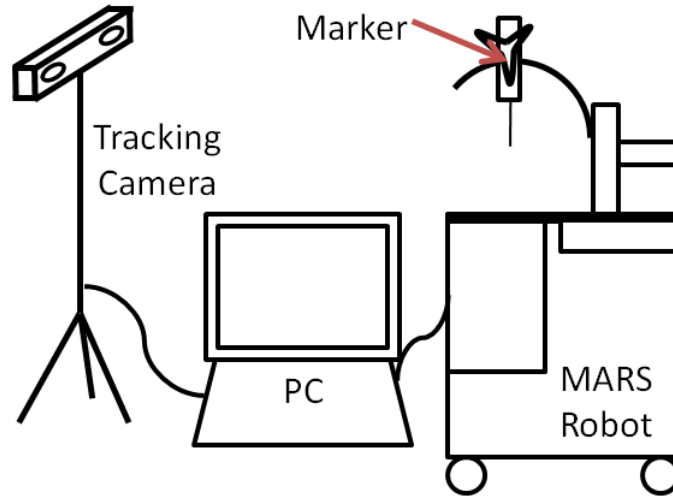
Figure 4.25: *Experimental setup to determine the accuracy of the kinematic chain of the MARS, consisting of the robot, a tracking camera, a control PC, a marker attached to the robot.*

were overlaid in the figure. This measurement yields information about the center of rotation **r2** for rotational axis r2.

Measurement (C) resembles measurement (B) but the two axes changed place. Hence, axis r1 was moved from α= -45° to α= +45° and then back to its initial position of α= -45°. In the next step axis r2 was moved by 10° from β= -45° to β= -35°. This is followed by a movement of r1 in the afore mentioned manner. These steps were repeated, until the r2 axis reached its final position of β= +45°. Again, ten datasets were recorded. Figure 4.26, bottom, illustrates the procedure: The arrows next to r1 indicate, that the axis is moved in both directions. The dotted arrow next to r2 indicates a stepwise movement in one direction only. Two arbitrary positions of r2 are shown in the figure. From the collected data, information about the center of rotation **r1** of rotational axis r1 is derived.

Data from measurement (A) was analyzed first. The corresponding points for each axis in the measurement were selected, and singular value decomposition was used on the point clouds. This yields three vectors, **t1**, **t2** and **t3**, that represent the direction of movement for each translational axis. The angles between all three pairs of vectors were calculated.

Next, the data for the measurement (B) was analyzed. It yields information about axis r1. In order to find the vector **r1** that represents the center of rotation of axis r1,
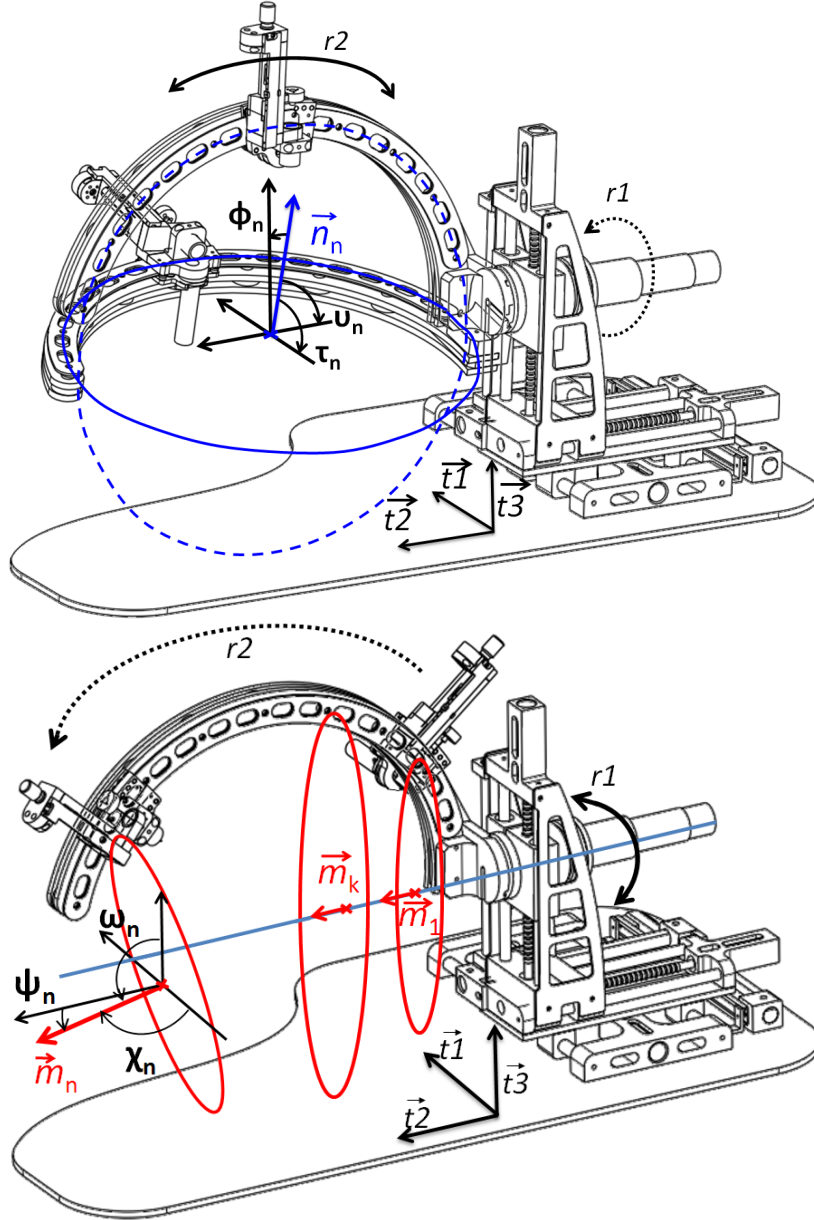
Figure 4.26: *Overview over the procedure to determine the kinematic chain of the MARS. On the top in blue measurement (B) and on the bottom in red measurement (C).*

circular fits were performed on the ten recorded datasets. The circular fit minimized a least-squares error function using the Gauss-Newton algorithm. It yields the coordinates of the center of the circle, the radius and the normal vector $\mathbf{n_n}$. The angles between $\mathbf{t_1}$-$\mathbf{t_3}$ and the ten normals $\mathbf{n_1}$-$\mathbf{n_{10}}$ were calculated. Figure 4.26, top, shows the recorded data with the corresponding circular fit in blue. Two arbitrary positions of axis r1 are overlaid. For one of the positions, the determined center point and the normal $\mathbf{n_n}$ are shown in the figure. The three angles between $\mathbf{n_n}$ and $\mathbf{t_1}$-$\mathbf{t_3}$ are labeled τ, υ and ϕ.

Data from measurement (C) (Figure 4.26, bottom) was analyzed last. It contains information about axis r2. Again, circular fits were used to obtain the center points and the normals $\mathbf{m_n}$. Next, the angles between $\mathbf{t_1}$-$\mathbf{t_3}$ and the ten normals $\mathbf{m_1}$-$\mathbf{m_{10}}$ were calculated. In Figure 4.26, bottom, the data points from the tracking camera and the corresponding circular fits are shown in red. Two positions of the carriage moving along the arc are overlaid. Each of the three depicted red circles has a corresponding normal labeled $\mathbf{m_1}$,$\mathbf{m_k}$ and $\mathbf{m_n}$. For $\mathbf{m_n}$, the angles between the normal and $\mathbf{t1}$-$\mathbf{t3}$, labeled ϕ, χ and ω, are indicated.

4.4.4.2 Results

Table 4.6 gives the angles τ, υ and ϕ for axis r1 (Figure 4.26, top) and Table 4.7 the angles χ, ψ and ω for axis r2 (Figure 4.26, bottom), respectively. Note that the marker for the tracking system was attached to the Micro-Drive unit which introduces an offset. Due to this, the angles τ and ϕ do not match α and $\alpha + 90°$. This, however, is not relevant for the data analysis.

There is a clearly visible tilting of axis r2 when $\beta > 15°$ (Table 4.7). This tilting also causes a translational deflection of the center point (Figure 4.26, bottom). In order to determine the unbiased alignment of the axis, all data for $\beta > 15°$ was neglected in the first analysis. The deviation found for $\beta > 15°$ is one of the motivations for the introduction of the calibration algorithm discussed later in this work (Subsection 4.5). Next, the angles between all five axes were determined. For t1-t3 with corresponding vectors $\mathbf{t1}$-$\mathbf{t3}$ the angles can be calculated instantaneously. The results are given in Table 4.8. For the rotational axes r1 and r2, some additional calculations are necessary. First, $\mathbf{r1}$ is determined using data from measurement (C) with the following approach: The center points and the normals for the seven remaining circular fits (Table 4.7) for axis r1 were combined in a matrix. Singular value decomposition is used on the

Table 4.6: *Measurement (B): Angles* τ, υ, ϕ *between* **t1** − **t3** *and determined normals* $\mathbf{n_{1\ldots10}}$.

Position axis r1(α)	τ	υ	ϕ
-45°	46.79°	89.96°	136.41°
-35°	36.99°	90.16°	126.61°
-25°	26.96°	90.20°	116.58°
-15°	17.04°	90.27°	106.65°
-5°	7.00°	90.31°	96.62°
5°	2.98°	90.36°	86.65°
15°	12.95°	90.40°	76.67°
25°	22.98°	90.42°	66.64°
35°	32.92°	90.45°	56.70°
45°	42.93°	90.46°	46.69°

Table 4.7: *Measurement (C): Angles* χ, ψ, ω *between* **t1** − **t3** *and determined normals* $\mathbf{m_{1\ldots10}}$.

Position axis r2(β)	χ	ψ	ω
-45°	89.97°	0.33°	89.71°
-35°	89.96°	0.32°	89.73°
-25°	89.97°	0.23°	89.83°
-15°	89.94°	0.22°	89.89°
-5°	89.95°	0.24°	89.85°
5°	89.96°	0.17°	89.99°
15°	90.02°	0.24°	89.79°
25°	92.19°	6.07°	84.31°
35°	91.92°	5.07°	85.28°
45°	90.98°	3.31°	86.81°

Table 4.8: Angles between the MARS axes **t1**, **t2**, **t3**, **r1** and **r2**.

Axis	t2	t3	r1	r2
t1	90.1299°	89.6190°	89.9671°	var.
t2		90.0059°	0.2500°	90.2982°
t3			89.8271°	var.
r1				90.0914°

matrix to determine the vector $\mathbf{r_1}$, representing the 'main' direction of the matrix. This equals the center of rotation for axis r1.

In a next step the circular fit described above is used to find a total of ten center points and normals from the data of measurement (B). The ten normals $\mathbf{n_{1...10}}$ are all roughly perpendicular to $\mathbf{r1}$. A plane is fit through the normals $\mathbf{n_{1...10}}$ and the parameters of this plane are determined. The angle between the plane and the vector $\mathbf{r1}$ is 90.09°.

Table 4.8 gives an overview over the angles between the axes. It shows that the actual values differ only marginally from the desired value of 90° and 0°. Note that no generic value can be given for the angles between $\mathbf{t1}$ and $\mathbf{r2}$ as well as $\mathbf{t3}$ and $\mathbf{r2}$. They are dependent on α and β.

Figure 4.27 illustrates the logged data from the optical tracking system which illustrates the relations between the axes r1 and r2. Data from measurement (B) as well as the corresponding normals are plotted in blue, the center points in green. Data from measurement (C) is plotted in red, as well as the corresponding normals. The center points of measurement (C) are presented in gray. The circles determined by the fitting algorithm for both measurements are black. Note that there was an offset between the marker and the interface at axis r2, hence the centers of measurement (B), indicated in green, do not match, yet the normals intersect in one point. All ten datasets from the measurement (B) and the datasets 1-7 from the measurement (C) are shown in the figure.

Figure 4.27 shows, that the normals $\mathbf{m}$ from measurement (C) (red), intersect the plane defined by the normals $\mathbf{n}$ from measurement (B) (blue), nearly perpendicular (Table 4.8). In an ideal system, all normals would intersect in one point. This is almost the case in the MARS.

In the analysis of the kinematic chain, no significant misalignment of the MARS axes was detected (Table 4.8). This allows the conclusion, that all measurable deflections are caused by the bending of the arc under load that manifests when axis r2 is moved
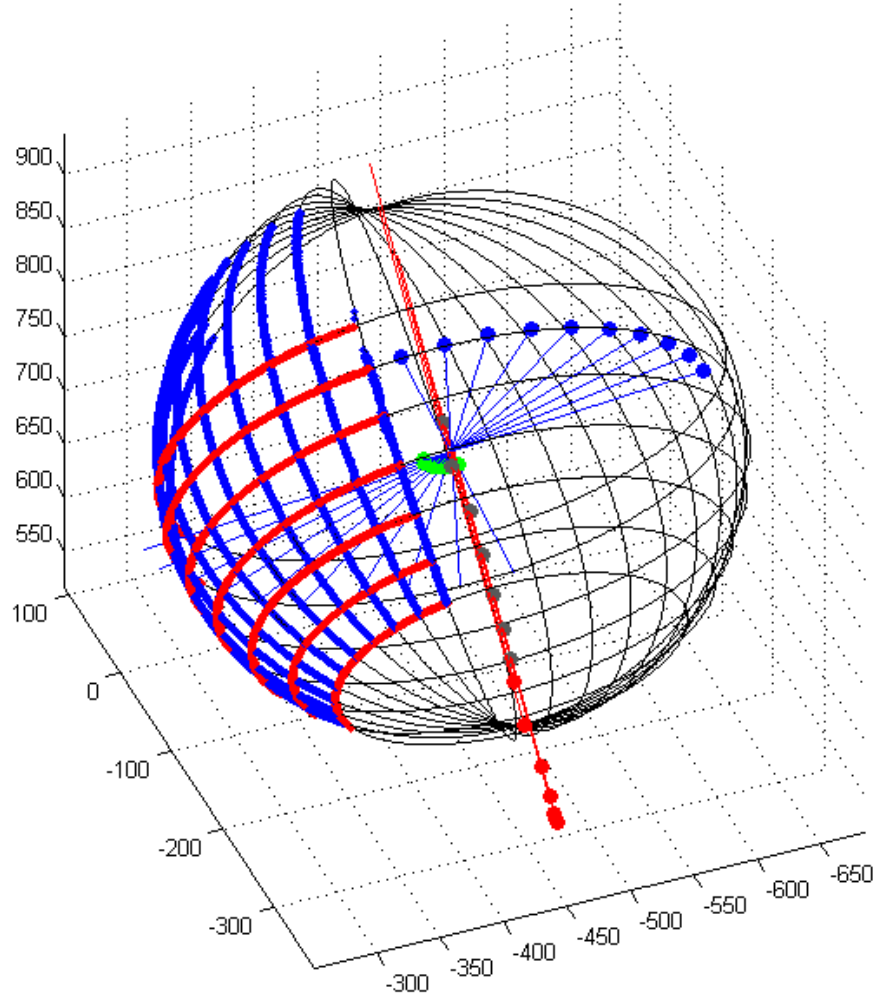
Figure 4.27: *Data from the optical tracking system illustrating the relations between rotational axes r1 and r2. The logged positions from measurement (B) and normals are shown in blue, the corresponding center points in green. The logged data from measurement (C) and normals are shown in red, the corresponding center points in gray. The circular fits for both measurements are plotted in black.*

towards the loose end (Table 4.7, $\beta > 15°$). In the next step, the impact of this error source on the accuracy at the center of the arc is analyzed and a calibration method to compensate for the error is developed.

4.5 Calibration

The analysis of the kinematic chain in Subsection 4.4.4 revealed, that there is a position dependent positioning error. To compensate for this error, a calibration method was developed and implemented. This process is described in the following.

Robot calibration methods can be categorized in two main fields: model-based and modeless methods [114]. Whereas the model-based methods involve the determination or adaptation of a kinematic model, modeless methods are based on the discretization of the work-space in small cubic cells or other points on a grid [115, 116].

The analysis in section 4.4.4 revealed that the most prominent error source is the non-linear bending of the arc under load. This bending is dependent on the positions of both rotational axes. As the structural parts of the arc are made of carbon-fiber reinforced plastic (which is an anisotropic material [111]) it is not practical to implement these findings in the kinematic calculations presented in Subsection 4.4.1. Hence, a modeless calibration method is applied.

The differences between desired and actual position are determined on a number of poses in the workspace of the robot. Based on this information, the error is compensated.

The findings from measurement (A) in section 4.4.4 indicate that the position deviations are caused by the movement of r1 and r2: The angles between t1-t3 are constant throughout the whole measurement. For this reason, the newly developed calibration algorithm is only dependent on the positions of r1 and r2.

The aim of the new calibration algorithm is to maximize the positioning accuracy at the part most relevant for the application: Instead of looking at the accuracy at the end-effector of the robot, the focus lies on the accuracy at the tip of the probe attached to it. Thereby, not only the errors introduced by the robotic system, but also the errors that are introduced by the probe itself are compensated for. This guarantees that the probes and electrodes are positioned at the preoperatively defined target.

4.5.1 Methods

Two perpendicularly mounted cameras (DFK 31AF03 TheImagingSource, Germany) with objective lenses (Edmund Optics, Germany) were used to monitor the displacement of the probe with respect to a virtual reference point with a motion resolution better than 0.01 mm. A macro-electrode (inomed Medizintechnik GmbH, Germany) was attached to the Micro-Drive unit, which in turn was connected to the interface of the robot at r2. The cameras were mounted to Manfrotto arms (Lino Manfrotto + Co., Italy) which allow flexible positioning with six degrees of freedom. The arms in turn were positioned such that the focal points of the cameras matched the probe tip. Furthermore, the direction of the camera has to match the direction of the translational axes **t1** and **t2**. This was validated by moving the robot along the axes t1 and t2 and adjusting the positions of the cameras. To calibrate the scales of the cameras to a millimeter-scale, an object with a fixed reference length was introduced to the focal areas. Its length in pixels was measured and the conversion to millimeter derived.

MATLAB was used to create a graphical user interface. Before the first movement of the robot, the user identified the position of the probe tip on both camera images. This position marked the virtual reference point.

Axes r1 and r2 were subsequently moved stepwise from $\alpha = -90°$ to $\alpha = +90°$ and $\beta = -45°$ to $\beta = +45°$, respectively. The step widths were 30° for α (r1) and 15° for β (r2). A total of 49 points was sampled.

At each point, the deviation between the virtual reference point and the probe tip was determined. Therefore, the user identified the current position of the probe tip on both camera images. The distance from the previously specified virtual reference point to the current position of the probe tip was calculated and transferred to a millimeter scale. Each camera yielded information about the displacement in two perpendicular directions. As they were mounted to match direction of movement of the robot **t1** and **t2**, respectively, redundant information existed for **t3**. The average of the two values was calculated and saved in the calibration file.

Figure 4.29 shows the measured deviations. Note that linear interpolation between the 49 original sampling points was used.

As expected, the deviation between desired and actual position grows, as the axes are moved away from their initial positions. The greatest deviation, with an Euclidean distance of 4.78 mm is found at the bound of r1 and r2 ($\alpha=90°$;$\beta=45°$).

Figure 4.28, left, depicts the deviation of the probe tip in XYZ direction. The norm

deviation is shown in Figure 4.29, left. Both figures indicate, that the deviation of the probe tip is strongly dependent on the position of the carriage moving along the arc. The deflection values are smaller when axis r2 is moved from its origin towards its suspension.

4.5.2 Results

The deviation was constant throughout multiple measurements. This leads to the conclusion that the deviation is mainly position-dependent, and that environmental influences can be neglected. The calibration algorithm can therefore be based on the previously determined deviations.

$$\mathbf{p_{cal}} = \mathbf{p} - e(\mathbf{p}) \qquad\qquad e(\mathbf{p}) = f \begin{pmatrix} \alpha \\ \beta \end{pmatrix} \qquad\qquad (4.15)$$

In Equation 4.15, the vector $\mathbf{p}$ denotes the target position of the robot before calibration and vector $\mathbf{p_{cal}}$ the target of the robot after calibration, respectively. The function $e(\mathbf{p})$ denotes the position dependent error that is corrected for by the calibration. As previously discussed, the error is only dependent on the angles α and β. The function $e(\mathbf{p})$ uses the previously determined deviation values. The deviation was measured at a discrete number of positions. In order to obtain a continuous function $e(\mathbf{p})$, bilinear interpolation between the sampled points is used.

When the user commands the robot to position $\mathbf{p}$, the system internally changes the target to $\mathbf{p_{cal}}$, thereby compensating for the previously discussed inaccuracies.

For accuracy evaluation of this approach, the same technique as described above is applied.

The 49 measured errors were Gaussian distributed. Mean deviation after calibration is 0.26 mm with a standard deviation of 0.20 mm. Maximum deviation is 0.90 mm (α=60°, β=15°). Figure 4.28, right shows the residual after the calibration for XYZ, Figure 4.29, right, depicts the norm. The presented results indicate, that a linear interpolated calibration algorithm can be used to minimize the deviation at the probe tip.

In the analysis of the mechanical accuracy of the robotic system, it was found that the translational axes are mutually perpendicular (see Table 4.8). Furthermore, it was discovered that the arc of the robot is deflected by gravity when axis r2 is moved
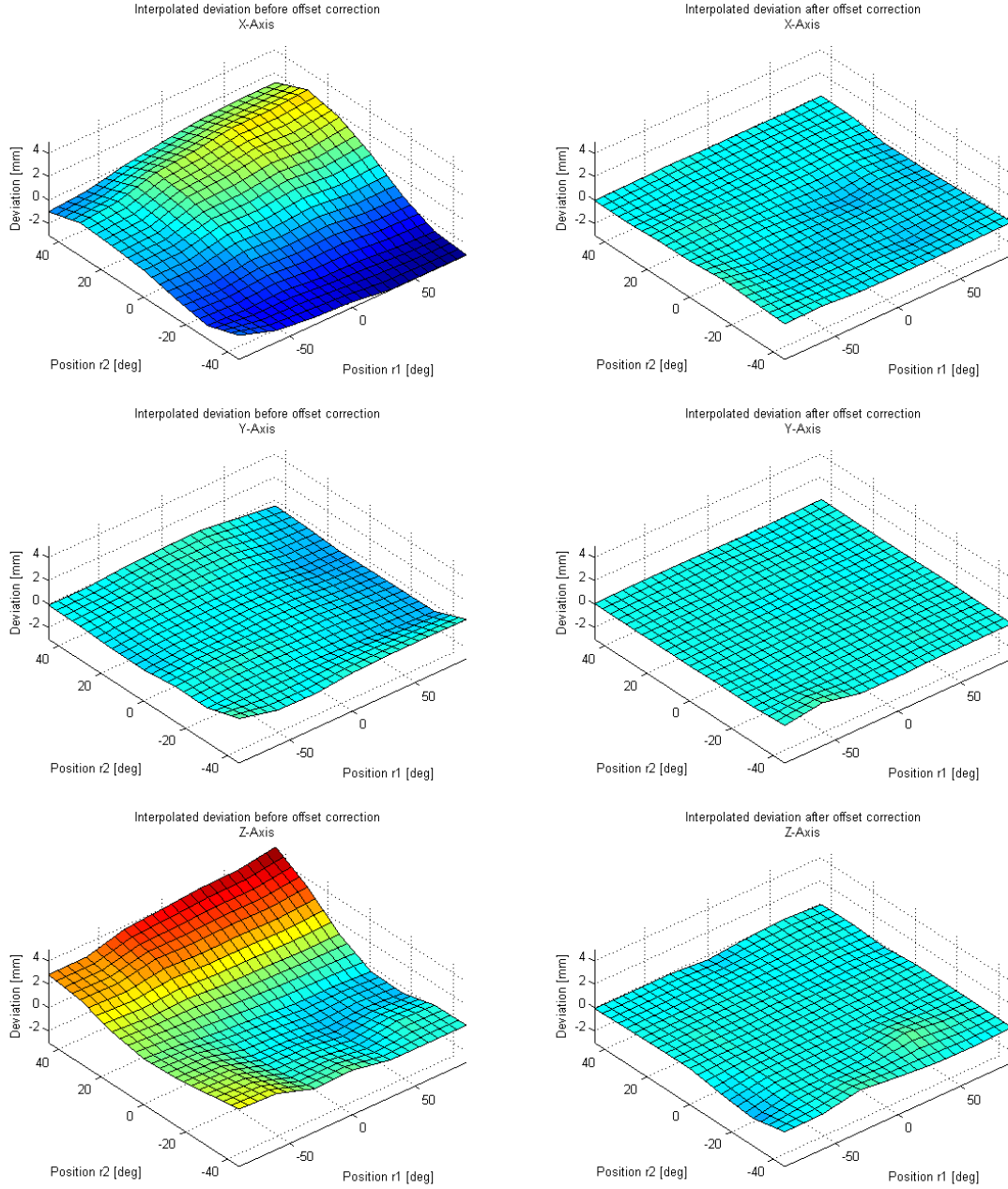
Figure 4.28: *Left: Errors before calibration. Right: After calibration. From top to bottom distance in X- Y- and Z-direction. The positions of r1 and r2 are given on the X- and Y-axis of the graphs, the corresponding offset is shown on the Z-axis.*
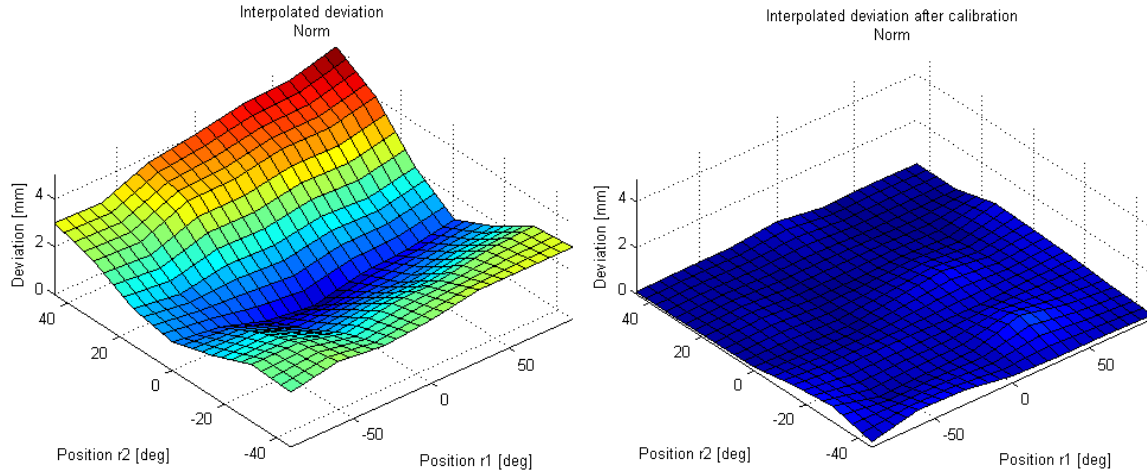
Figure 4.29: *Interpolated Euclidean distance between the actual position of the probe tip and the planned position; No calibration left, maximal deviation: 4.78 mm, minimal deviation: 0.04 mm. After calibration right, maximal deviation: 0.90 mm, minimal deviation: 0.04 mm. Strong deviation is indicated with red, weak with blue colors.*

towards its loose end. This is a consequence of the kinematic chain: The arc is suspended on one side only. Based on this analysis, a modeless calibration algorithm was developed and implemented.

The calibration of the system focuses on the accuracy at the tip of the probe attached to the end-effector of the robot. This approach allows to compensate for inaccuracies caused by the robotic system itself as well as inaccuracies caused by the probe. By using the linear compensation algorithm, the mean error after the calibration was reduced to 0.26 mm with a standard deviation of 0.20 mm and a maximal deviation of 0.90 mm.

4.5.3 Position sensitive diode

The previously described calibration method yields good results, however it is very time consuming to setup the required instruments. Furthermore, a new calibration is required if the setup is altered. A calibration tool that overcomes these limitations needs to provide the following features:

- **Accuracy:** The position deviation needs to be monitored with a resolution better than 0.1 mm.
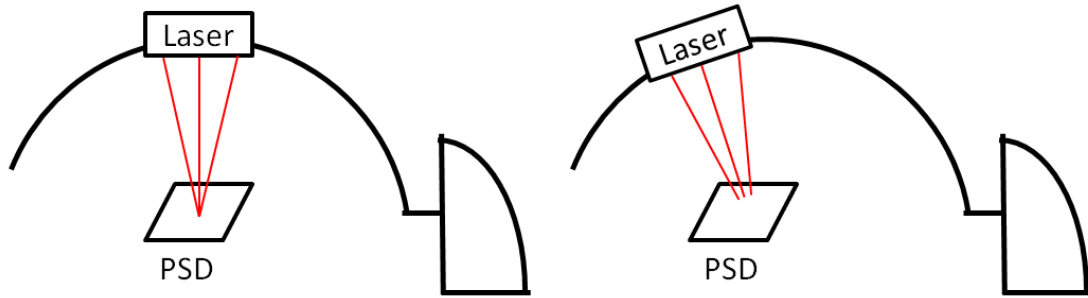
Figure 4.30: *Laser calibration functional principle. Left: PSD and MARS robot in the initial position. All three lasers hit the same point. Right: After the movement of axis r2, the lasers create three distinguishable impact points.*

- **Fast application:** The system should require very little setup time and yield reliable and reproducible results.

- **Continuous sampling:** The system should provide continuous position information.

- **Compatibility:** It should integrate into the MARS without the need for modifications.

In the scope of the thesis, a laser based calibration tool was developed. Its design, functional principle and application are presented in the following.

4.5.3.1 Functional principle

Figure 4.30 depicts the principle of this calibration method. Three laser sources are attached to the interface at r2. They are positioned in a way that the light beams intersect in the center of arc (Figure 4.30, left).

A position sensitive diode (PSD) is used to determine the impact point of the laser beams. This sensor type has been first described in the 1930s [117] and further refined in the 1970s [118, 119]. PSDs are commonly used in distance measurements based on triangulation [120, 121].

A PSD presents a solution to the above mentioned requirements. It features a very high spatial resolution of 0.3 μm and a rise time of 4.0 μs [122]. PSDs have been successfully used in the calibration of industrial robots [123]. Continuous position data is available. A PSD gives the position of the center of gravity of the laser beam that hits the active area of the PSD.

The calibration procedure with the PSD is described next. To start, the PSD is aligned with the center of arc. Then, the rotational axes of the robot are moved. In an ideal system, this does not have an effect on the points of impact of the three lasers. If there is movement in one of the translational axes, the points of impact differ from the reference. Movement in the XY-plane will cause a movement of the single impact point. Movement in Z-direction cause the appearance of two more impact points. Figure 4.30, right, illustrates the influence of movement: The light beams hit the PSD at three distinguishable impact points.

The actual calibration process is similar to the one described in Subsection 4.5.1. First, a reference point is defined. Here, the laser beams intersect on the surface of the PSD. Next, the workspace of the robot is sampled stepwise. At each position, the deviation is determined using the PSD. The robot automatically moves its translational axes according to the deviations determined by the PSD until all laser beams intersect at the reference point. The required movement of the axes presents the offset vector at the given point and is stored in the calibration table.

4.5.3.2 Hardware

In order to acquire position data from the PSD, an electric circuit was developed. The main components of this PSD system are:

- **PSD:** The duo-lateral positive intrinsic negative (PIN) diode (DL400-7 SMD, First Sensor AG, Germany) has an active area of 20×20 mm^2 and four contacts. The photons of the laser beam hitting the PSD cause a movement of charge carriers in the PSD [124]. They are distributed among the four contacts (two cathodes, two anodes) proportional to the center of gravity of the light spot that hits the surface. This causes a current at the contacts.

- **Operational amplifiers:** Four OPA131 operational amplifiers (Texas Instruments Incorporated, USA) are required for the circuit. They are operated in a current to voltage converter setup [125]. They convert the currents of the four PSD contacts to a proportional voltage. The gain is chosen such, that the resulting voltage is in the operating range of the AD converter.

- **AD converter**: The wires conducting the voltage from the four operational amplifiers are connected to the AD converter (ADS1258 Texas Instruments Incorporated, USA). Here, they are converted with a resolution of 24 bit and a

sampling rate of 23.7 kHz [126]. The AD converter is controlled by a MCU (AT90USB162, Atmel Corp., USA) via SPI.

- **Laser:** Three identical LFD650-5-3 lasers (Picotronic GmbH, Germany) are used to excite the PSD. They are attached to the interface at r2. The wavelength of the lasers is 650 nm with a power of 5 mW.

- **Bandpass filter:** Changing background illumination can interfere with the signal from the PSD or drive the PSD into saturation [121]. To block light waves with wavelength other than 650 nm, a FB650-10 bandpass filter (Thorlabs, USA) is positioned in front of the PSD.

The position of the center of gravity of the light beam hitting the PSD can be calculated based on the voltages. With x denominating the position along the first axis, and y the position along the second axis of the PSD:

$$x = k_x \cdot \frac{U_{a1} - U_{a2}}{U_{a1} + U_{a2}} \;\; and \;\; y = k_y \cdot \frac{U_{c1} - U_{c2}}{U_{c1} + U_{c2}} \tag{4.16}$$

U_a and U_c denote the voltages at the anodes and the cathodes, respectively. Two constant factors k_x and k_y need to be considered. They are dependent on the dimensions of the PSD, here 20×20 mm². To obtain a position information, the four voltages are queried from the AD converter and the position is calculated by the software.

Figure 4.31 depicts the circuit board of the PSD system. On the left, the actual PSD with its four contacts is depicted. A LED is used to indicate the status of the circuits. The right of Figure 4.31 illustrates the backside of the board with the operational amplifiers, the AD converter and the MCU. The board interfaces to a PC via a USB port. As described in Subsection 4.2.3, the MCU emulates a COM port for the communication with the circuits.

The PSD is an analog device that determines the center of gravity of all photo currents that occur. For this reason, it is important that only one laser is active at the time of the measurement. The activity of the lasers is handled by a second circuit board with a MCU. Again, the MCU emulates a COM port. The PSD system is housed in a plastic box to facilitate its application.
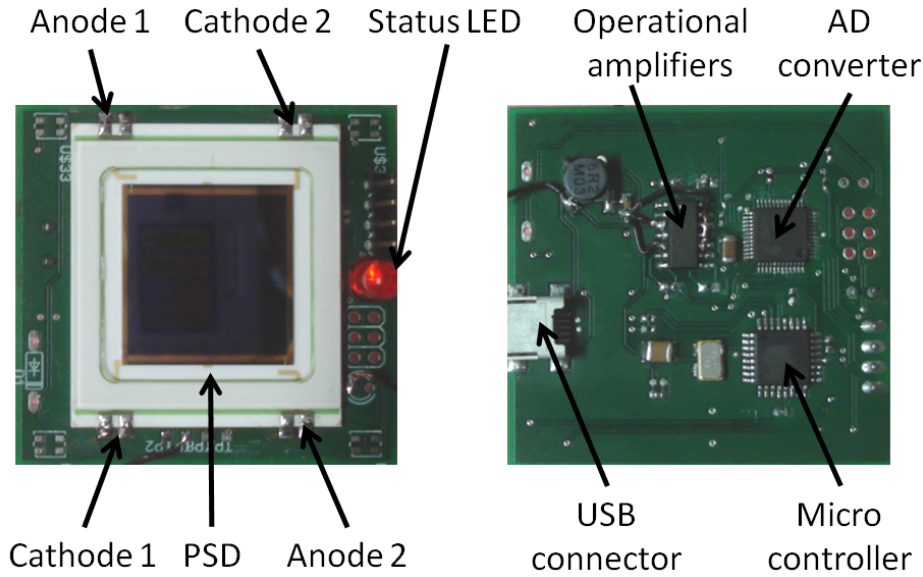
Figure 4.31: *Left: Top view of the PSD board with the actual PSD, its two cathodes and anodes and the status LED. Right: Bottom side of the PSD with the MCU, the USB connector, the operational amplifiers and the AD converter.*

4.5.3.3 Experimental validation

A mounting for the three laser sources is attached to the interface at r2. The lasers are fixed in the mounting. Figure 4.32 shows the experimental setup: The PSD system is positioned at the center of arc of the MARS robot. The red lines indicate the directions of the laser beams. The dotted white lines indicate the center of rotation for r1 and r2.

To validate if the PSD is aligned with the plane defined by **t1** and **t2**, a test measurement is conducted: The three lasers are activated and the robot moves its t1 and t2 axes. The resulting position from the PSD is monitored. If required, the alignment of the PSD is corrected.

The final calibration data resembles the data shown in Figure 4.28 and Figure 4.29. The time required to obtain the data is greatly reduced when compared to the optical calibration.

Due to the integration of the PSD into the MARS, the calibration process is simplified. This is an important point for the usability of the robot.
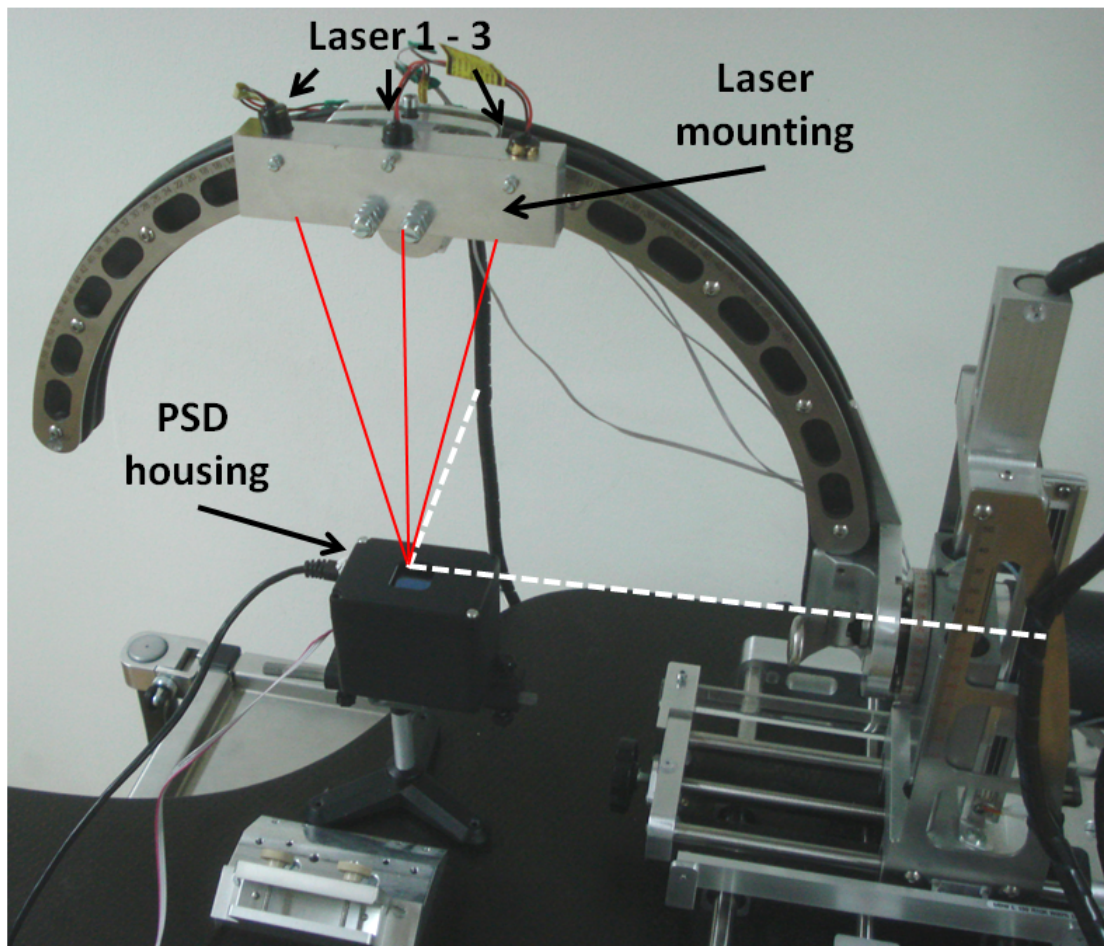
Figure 4.32: *Experimental setup for MARS calibration using the PSD. The laser mounting is attached to the interface at r2. The red arrows indicate the direction of the laser light. It hits the PSD at one point. The two dotted white lines indicate the center of rotation for r1 and r2, respectively.*

4.6 Operating modes

The MARS provides four different operating modes. The user can at all times switch among them. In the following section, first, the two basic operating modes, the manual and the automatic mode, will be explained. Next, two intelligent modes, the semi-manual and the hybrid mode, are described. The properties of each operating mode will be discussed briefly. To conclude, a comparison of the modes is given.

4.6.1 Automatic mode

In the automatic mode, the robot is connected to power and a PC is used to control the system. After defining the trajectories in the software, the robot automatically moves to the desired pose.
In this operating mode, the following features are available:

- **Redundant position monitoring:** The two encoders for each axis are continuously monitoring the position of the axis. If the difference between them exceeds a defined limit, the robot is stopped and a warning is displayed to the user.

- **Current monitoring:** The MCBL3006s controllers feature a programmable current limit (Subsection 4.2.2). This feature is used to limit the power of the axes in the first order and the robot is automatically stopped when one of the limits is exceeded.

- **Automated positioning:** The robot automatically moves to the previously defined target pose. The PID controller running on the MCBL3006s unit ensures that the position is held in case of disturbances.

- **User information:** The user is informed about the status of the robot. Various information can be displayed, e.g., current position, speed, target position, power consumption etc.

The automatic mode is similar to the operating mode of current robotic neurosurgery systems described in Section 2.3.

4.6.2 Manual mode

The manual operating mode is the second basic mode of the MARS. Here, the robot is not energized and no PC is required. The robot serves as a manual positioning aid, just like regular stereotactic frames, e.g. ZD-frame (Section 2.2). Manual scales on each axis indicate the position of the robot. The surgeon manipulates the knobs of the axes to position them according to the preoperative plan generated by the surgical planning software.

The manual operating mode resembles the use of manual stereotactic frames and does not include any additional safety features. However, the surgeon can always fall back to this operating mode, in case errors occur in the automatic mode, if there is a power outage or in other emergency situations. The surgeon can intuitively handle the MARS in the manual mode, thanks to the similarity of the kinematic chain with the ZD-frame.

To save time, interventions that do not require the highest possible accuracy, e.g. biopsies of voluminous tumors, can be executed in the manual mode without setting up the robot and its software.

4.6.3 Semi-manual mode

In the semi-manual operating mode, the robot is connected to power and its software is running. The user can now automatically position the robot using its motors. Furthermore, he can deactivate the motors and manually adjust the robot to a position using the knobs of the axes. This enables the user to course position the robot quickly and conveniently using the motors and then fine adjust the positions of the axes.

Note that the PC with the control-software is active during that time. The positions of the axes are continuously monitored by the hall-encoders as well as the secondary absolute encoders and are displayed to the user.

The user can at all times switch between the manual and the automatic mode using the software.

4.6.4 Hybrid mode

In this operating mode, the robot is running in the automatic mode. The currents of the controllers are continuously monitored. If the user wants to reposition the robot or stop its movement, he can do so by simply grabbing and holding one of the axes'
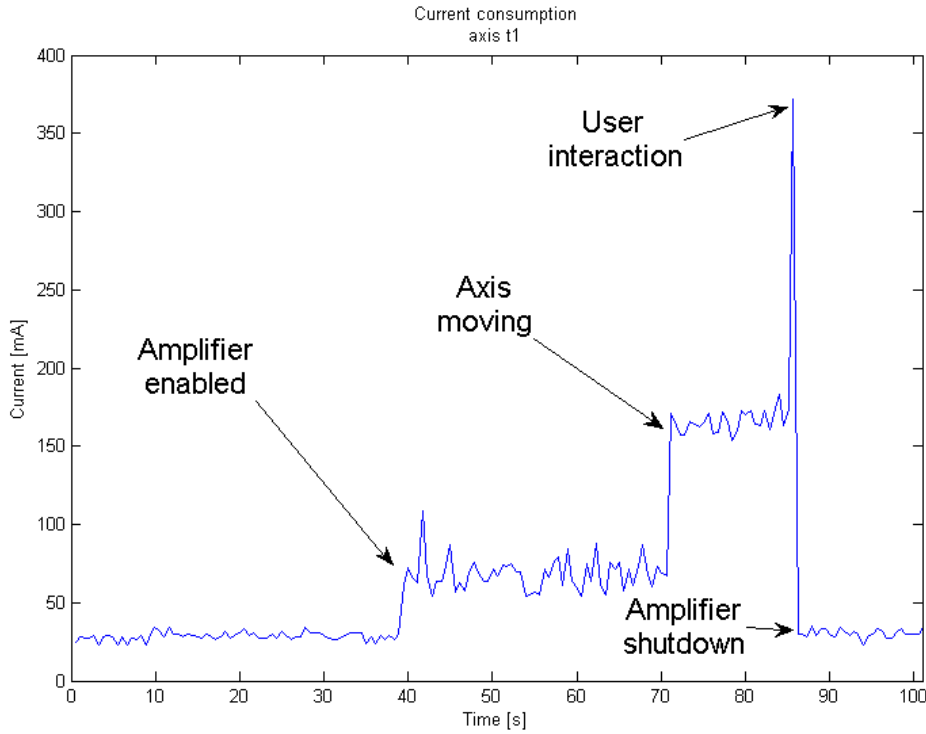
Figure 4.33: *Current consumption during hybrid operating mode. The current consumption in [mA] of the t1-axis controller is plotted over the time [s]. After activating the controller (t = 0 s) and the amplifiers (t = 40 s), the axis is moved (t = 70 s). The user interaction (t = 86 s) leads to an immediate shutdown of the amplifier.*

knobs or a moving part of the robot. This manual interaction will lead to a change in the power consumption of one or more controllers. The software automatically detects this change and deactivates the amplifiers of the controllers. The robot stops and the user can now either manually position the axes using the knobs or reactivate the amplifiers of the robot and continue in the automatic mode. Note that the position of each axis is continuously monitored by the two independent encoders.

This operating mode greatly enhances the safety of the system. User interaction or unusually high interaction forces, e.g., caused by hitting an obstacle, will lead to an immediate shut down of the amplifiers. The user is informed that the amplifiers were switched off because the current consumption limit for the hybrid mode was exceeded.

Figure 4.33 shows the current consumption of axis t1 during user interaction. The figure can be divided in five zones: First, the controller is powered but its amplifier

Table 4.9: *Properties of the four operating modes of the MARS. A property is assigned to a mode with a '•' sign; a '○' indicates partial matching.*

	Automatic mode	Manual mode	Semi-automatic mode	Hybrid mode
Position & current monitoring	•		•	•
Surgeon in charge		•	○	○
Automated axes positioning	•		○	○
Status information	•		•	•
User interaction detection				•
Log file generation	•		•	•
Offset correction	•		○	○

is disabled. This leads to low current consumption (0–40 s). In the second zone, the amplifier is enabled yielding a higher power consumption (40–70 s). Third, the axis is moving which leads to yet higher current consumption (70–86 s). While the axis is moving, the user interacts with it by grabbing its knob. This leads to a steep increase of the current intake at around 86 s. The software detects that the consumption is above the set limit of 200 mA and immediately shuts down the amplifiers of the controller.

The mechanism was explained for axis t1 exemplary, the same principle is used for the other axes. After the shutdown of the amplifiers, the user can remove the obstacle and continue either in an automatic mode by reactivating the amplifiers or in a manual mode by manipulating the knobs of the axes.

4.6.5 Summary

Table 4.9 summarizes the properties of the four operating modes. Note that 'smart' features, e.g., automatic position and current monitoring require a PC and a power connection of the robot. Some features are only available when the amplifiers of the robot are activated. Depending on the current state, this is not always the case in the semi-automatic and the hybrid mode.

Thanks to the implementation of the hybrid mode, the usability of the system is

greatly improved. This feature distinguishes the robot from previous robotic systems. The intuitive and safe switching between various operating modes leads to increased security and high acceptance by the surgeons. The possibility to always fall-back to the manual mode completes the safety strategy of the MARS.

The description of the operating modes concludes the chapter about the Motor Assisted Stereotaxy System. So far, the design of the system, its hardware and control framework as well as its kinematics and operating modes were described. In Chapter 6, the application of the system will be covered.

5 Magnetic probe localization

So far, the robotic positioning of probes and instruments was covered. Beside the positioning, also the localization of the probe inside the brain is of great importance for the application. Various error sources, e.g. probe tissue interaction, can cause a deviation of the probe from the planned trajectory (see Section 2.5). Continuous monitoring of the probe position is therefore desirable.

Small NdFeB permanent magnets can easily be integrated in neurosurgical tools, e.g. biopsy needles. The magnetic signal generation is an intrinsic property of the magnet and hence fail-safe. Especially in medical applications, this is of great importance. In contrast to active magnetic tracking, no wires or field generators are required. The surgeons can continue to use their conventional instruments.

In the scope of this thesis, the localization based on static magnetic fields is adapted to the field of stereotactic neurosurgery. First, the localization algorithms are described, then the hardware used in the final setup is presented. The choice and alignment of the sensors is discussed and the interface with the MARS is explained.

5.1 Localization algorithms

In previous publications, the localization of the magnetic flux source was based on the dipole model assumption (see Subsection 2.5.4). The main reasoning for its application is, that it only requires little information about the properties of the magnet. Furthermore, the inverse problem can be solved numerically. Also, high temporal resolution is achievable. As this method presents a standard for localization systems, its implementation is presented first.

On the other hand, this model based localization has its limitations: First of all, some applications in neurosurgery require an accuracy greater than what has been published in the literature so far (see Table 2.5).

The dipole assumption is only valid when the distances between the magnet and the sensors are great. This is not always the case for the application in stereotactic neu-

rosurgery. If the magnet is too close to the sensors, its shape has an influence on the measured magnetic flux.

Due to manufacturing tolerances not all sensors are equally sensitive to changes in the magnetic flux. This could have negative influence on the results of the localization algorithm. The model based approach is further limited by this fact.

Special attention needs to be paid when mounting the sensors to their ground plate. Problems arise if their actual position with respect to an origin differ from the assumed. Furthermore, the localization algorithm is limited to dipoles. Other objects that generate a magnetic flux, e.g. surgical instruments, cannot be detected as their magnetic field is not known a priori.

With the focus on the application of static magnetic field tracking in stereotactic neurosurgery, further conditions apply. The movement of the magnetic source in the brain can be considered quasi-static. The insertation speeds are commonly very slow. In conventional stereotactic interventions, only straight probe trajectories need to be considered. The probe is surrounded by delicate tissue and a change of orientation after the insertion is not possible.

The connection of stereotaxy with a robotic system allows new localization approaches. In previous work at the institute, the use of lookup tables for magnetic probe localization has been studied [127, 128]. The magnetic probe is attached to the robot and the workspace of the robot is sampled stepwise. After each step, the current flux at the sensors is saved along with the position of the robot. In the actual localization, the magnetic flux at the sensor is compared to the data from the lookup table. A nearest neighbor approach is used to identify the corresponding node in the table. The position of the magnet is derived from the node. This method can be used to track arbitrary geometries and is not limited to point-shaped dipole sources.

Although highly accurate localization is possible using lookup tables, their use has several disadvantages. First, the generation of lookup tables is very time consuming. Depending on the required workspace, several thousand points need to be sampled. As it is not practical to sample on a sub-millimeter level, interpolation is used. This further increases the search-space for the localization task and localization in real time is not possible. More importantly, there are practical limitations. Small changes in the sensor setup require the generation of a new lookup table. These changes can be caused by the reassembly of the setup or other common work on the system.

As both, the numerical solution and the lookup table based approach, have their limitations, a new localization algorithm was developed. It is designed specifically for

the application in stereotactic neurosurgery. The so called 'mini lookup table' approach is related to the regular lookup table algorithm. Its fundamentals and implementation are discussed after the numerical solution.

To conclude, the magnetic flux sensors used in the scope of this work are described. The design and implementation of the sensor hardware is discussed and the properties of the sensors are evaluated.

5.2 Numerical solution

The numerical solution of the localization problem is based on the assumption, that the magnetic flux source is an ideal dipole, i.e. that it has no spatial extent. The magnetic flux $\mathbf{B}(\mathbf{r}, \mathbf{m})$ generated by a dipole can be calculated as follows [77]:

$$\mathbf{B}(\mathbf{r}, \mathbf{m}) = \frac{\mu_0 \mu_r}{4\pi} \left(\frac{3\mathbf{r}(\mathbf{m} \cdot \mathbf{r})}{r^5} - \frac{\mathbf{m}}{r^3} \right) \tag{5.1}$$

$\mathbf{B}$ denotes the magnetic flux, $\mathbf{r}$ the position and $\mathbf{m}$ the magnetic moment of the magnet. The magnetic permeability is given by μ_0. As the system is operated in air, the magnetic permeability $\mu_0 = 4\pi \times 10^{-7} T \cdot m/A$ and $\mu_r = 1$. Note that the introduction of steel or other material with a magnetic permeability other than 1 introduces disturbances in the magnetic field. The theoretical field given in Equation 5.1 is used for the numerical solution.

The theoretical magnetic flux at an initial position is calculated for all sensors of the setup. Next, these values are compared to the actual measured values and the quality of the solution is evaluated. In order to quantify the quality of the current values for $\mathbf{r}$ and $\mathbf{m}$, the following quality function is used:

$$E = \sum_{n=1}^{N} \sqrt{\left[\mathbf{B}(\mathbf{r}, \mathbf{m})_{\mathbf{meas\ n}} - \mathbf{B}(\mathbf{r}, \mathbf{m})_{\mathbf{calc\ n}} \right]^2} \tag{5.2}$$

With n being the number of the current sensor and N the total number of sensors. $\mathbf{B}(\mathbf{r}, \mathbf{m})_{\mathbf{meas\ n}}$ denotes the measured magnetic flux at the sensor n and $\mathbf{B}(\mathbf{r}, \mathbf{m})_{\mathbf{calc\ n}}$ the theoretical flux. Note that information from all the sensors is used in one quality function.

The magnetic flux values are given with respect to the coordinate system of the sensors. Before further processing, they are transformed to the reference coordinate system (see Figure 5.1)
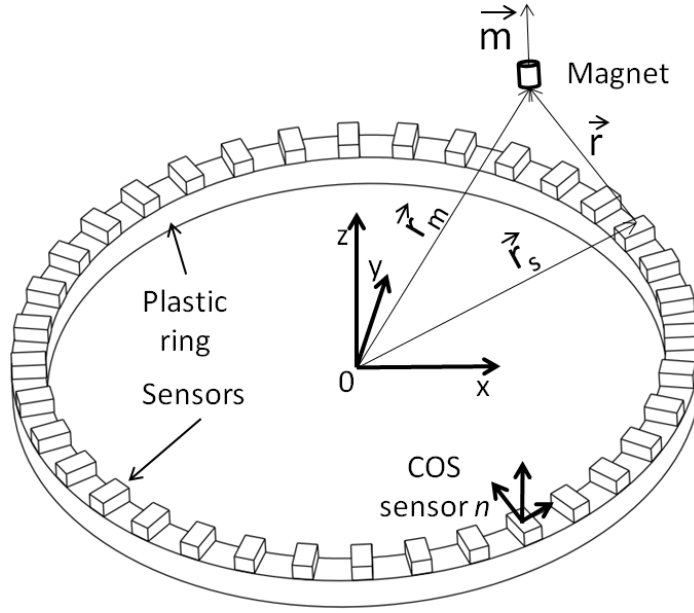
Figure 5.1: *Functional principle of the localization based on the dipole model. The magnetic flux generated by the permanent magnet is measured with various sensors.*

In the next step, the values for $\mathbf{r}$ and $\mathbf{m}$ are altered before the next calculation of the theoretical flux. Then, flux is calculated and the new error is accessed using the quality function. These steps are repeated until a minimum is found. The Levenberg-Marquardt algorithm [79, 80] presents a powerful tool for the numerical solution. It is used to solve this minimization problem.

Note that a great variety of quality functions exits. In [76, 81] only the magnetic flux in one axis is considered. It can be beneficial to neglect data from one or more axes, when it was wrongly assumed, that the magnetic flux is measured at exactly one point in the sensors. This is never the case for real sensor systems.

Figure 5.1 shows the functional principle of the dipole model based localization. A number of sensors (here 36) are aligned in a defined way (here circular, distance 10°). The middle of the plastic ring defines the origin for the setup. In the figure, the vectors involved for one of the 36 sensors are depicted. Four vectors are of interest for the localization: $\mathbf{r_s}$ is defined by the distance between the origin and the sensor, $\mathbf{r_m}$ gives the distance of the magnet with respect to the origin. The vector $\mathbf{r}$ is defined by the distance between the sensor and the magnet and $\mathbf{m}$ indicates the strength and orientation of the magnetic moment of the magnet. The aim of the algorithm is to determine $\mathbf{r_m}$, the position and $\mathbf{m}$, the orientation of the magnet with respect to the

origin.

Before the actual experiments, the magnetic moment **m** of a cylindrical permanent magnet with $\varnothing 3 \times 6$ mm is measured. This magnet is used in all subsequent experiments. Therefore, the magnet is fixed to a plastic rod. The plastic rod in turn is mounted to the interface at the MARS with a distance of 50 mm to one of the magnetic flux sensors. It is positioned in the XY-plane in a way, that the measured flux is predominant in the Z-axis of the sensor. At this point, the magnet aligns with the Z-axis of the sensor.

The magnetic flux at the sensor is measured and saved along with the position of the magnet. Next, MARS moves stepwise along the Z-axis. A total of N=10 steps with a step width of 5 mm is sampled. At each position, the magnetic flux is saved.

From the acquired data, the magnetic moment **m** of the permanent magnet is calculated. Therefore, **m** is altered until the minimum of the following error function is found:

$$E = \sum_{n=1}^{N} \sqrt{\left[\mathbf{B_{meas\ n}} - \mathbf{B}(\mathbf{r_{init}} + \mathbf{n} \cdot \begin{pmatrix} 0 \\ 0 \\ s \end{pmatrix}, \mathbf{m})_{\mathbf{calc}} \right]^2} \qquad (5.3)$$

The Levenberg-Marquardt algorithm is used to minimize the function. **n** denotes the number of the current measurement, from 1 to N. $\mathbf{B_{meas}}$ labels the measured value at the n-th point and $\mathbf{B_{calc}}$ the calculated theoretical field. $\mathbf{r_{init}}$ indicates the initial position of the magnet with respect to the sensor. **s** stands for the step width of the measurement.

Note that the movement of the MARS was along the Z-axis of the sensor. This fact is represented in Equation 5.3: The X- and Y-components of the step width vector equal zero.

With the given algorithm, a magnetic moment **m** of 0.0575 Am^2 was found. This fact is used for the localization algorithm described by Equation 5.2. The magnitude of the vector **m** is now known which simplifies the localization problem.

The experiments and results using the localization algorithm are presented in Section 6.6.

5.3 Mini lookup table

The mini lookup table algorithm is related to the lookup table based localization briefly described before. Instead of a complete table, a miniature table is recorded just before the intervention. This approach requires less time than the generation of a complete lookup table. Furthermore, it is specific to the probe used in the setup. This enhances the resolution of the localization.

For the algorithm, the following steps are necessary: The robot is attached to the operating table. Before the actual intervention, the magnetic sensor setup is positioned on the mounting of the ground plate of the MARS. Next, the axes are aligned with the entry point defined in the surgical planning software.

Still preoperatively, the probe is forwarded stepwise until the target point is reached. During this forwarding, multiple magnetic flux measurements are conducted. The current position of the probe is saved along with the magnetic flux data. This way, a first mini lookup table is generated. Next, the probe is removed and again, the magnetic flux is measured at each step. This yields a second mini lookup table.

The average of the two tables is later used for the actual localization and the difference between the them quantifies the sensor noise. For each position of the probe, an expected noise level is calculated.

The beginning of the surgical procedure follows the pattern described in Section 1.1 and will not be discussed here. The probe is positioned at the previously defined entry point. Next, it is forwarded into the tissue. After each step, the magnetic flux is measured and compared to the data of the averaged mini lookup table.

If the difference between the measurement and the lookup table is bigger than the expected noise level, the probe deviates from the planned path. The difference in the magnetic flux is an indicator on how strong the deviation is. However, it does not indicate in which direction the probe deviates.

The recorded data is specific for the situation in the OT. It takes into account that two magnetic field sources are never equal, due to manufacturing tolerances and slightly different material properties. The possibly negative effects on the localization are suppressed.

Beside the variability in the instruments, other disturbances can influence the magnetic flux. The most prominent disturbance sources are ferromagnetic objects, e.g. steel, in proximity to the setup. In the OT, the presence of ferromagnetic objects cannot be ruled out. The trajectory definition approach yields correct results even in the

presence of ferromagnetic objects, as long as their position is not changed during the time of the intervention.

In the mini lookup table approach, the distances between two neighboring nodes are small. This is possible, as only a fraction of the work space of the robot is sampled. Hence, there is no need to use interpolation to enhance the accuracy which can introduce errors.

As the search space is reduced, the algorithm is much faster than the conventional lookup table based approach and the numerical solution. The results of the application of the mini lookup table algorithm are presented in Section 6.6.

5.4 Hardware

The sensor setup developed in the scope of this thesis is based on the iM3501 motion senor (amotech Inc., Korea) which includes a compass module. It measures the magnetic flux at the sensor with a resolution of 10×10^{-9}T or 10 nT [129]. Hence, its resolution is in the same order of magnitude as the senors discussed in Section 2.5, except for the SQUID sensors.

The dimensions of the sensor are only $5.0 \times 5.0 \times 1.2$ mm^3. Especially when multiple sensors are used, this small footprint is a major benefit. In contrast to the sensors used in [83] and others, no external hardware, e.g. amplifiers or ADC are required.

Multiple sensors can be queried using serial peripheral interface (SPI). Each sensor is connected to four common channels: Master Out Slave In (MOSI), Master In Slave Out (MISO), Clock (CLK) , Reset. Furthermore, one Slave Select (SS) channel per sensor is required. Its small footprint and the communication via SPI make the iM3501 an ideal sensor for the application.

A Seeeduino Mega board (Seeed Studio, China) is used to control the sensors. It is compatible to the arduino Mega and can be programmed with the Arduino 1.0 open-source environment. The software is written in the arduino language. The Seeeduino Mega board features an ATmega1280 (Atmel, USA) MCU. It can be connected to the PC via USB, the communication is handled by a virtual COM port. As mentioned in Subsection 4.2.2, one USB port remains idle in the control box of the MARS. It can be used for the Seeeduino board.

To minimize magnetic interferences, a plastic ring is used as ground plate for the sensor setup. The compatibility requirement (see Chapter 3) also applies to the sensor setup.
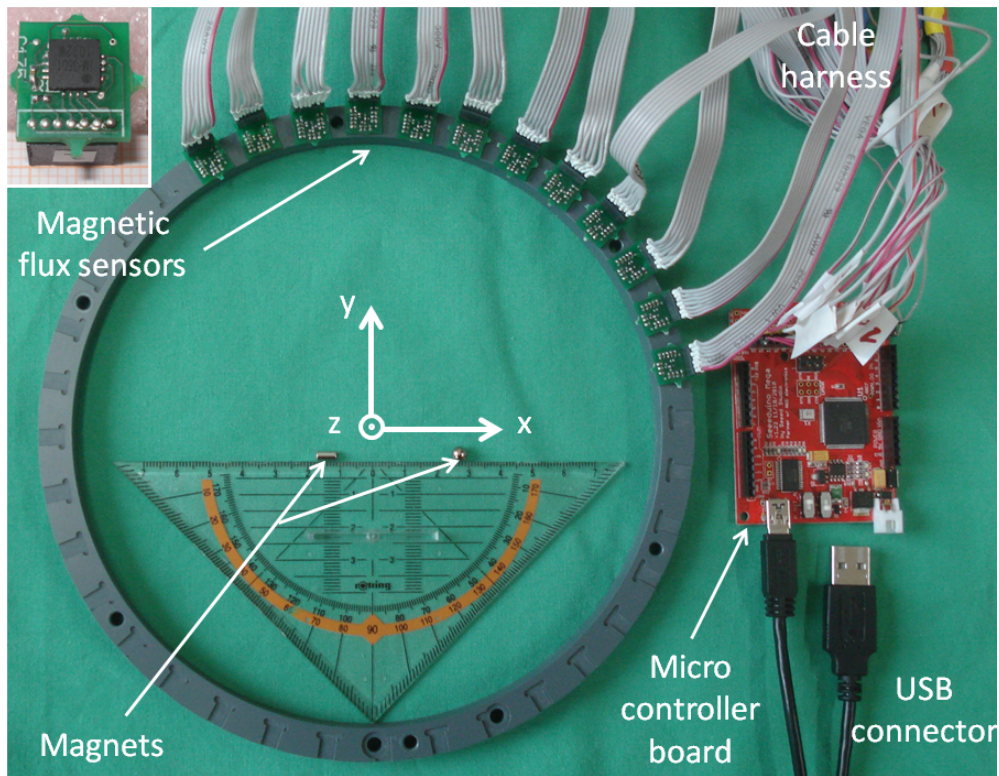
Figure 5.2: *Sensor setup MARS magnetic localization. Twelve iM3501 magnetic flux sensors are mounted to the circular base ring. The ring can be fixed to the ground plate of the MARS. On the top left, one iM3501 sensor with PCB is shown.*

Therefore, the plastic ring can be attached to the ground plate of the MARS or to the stereotactic base unit of the industrial collaborator inomed Medizintechnik GmbH.

The sensor mountings are alinged on the ring with a distance of 10°, hence and a total of 36 sensors can be used. To fix the sensors, they are glued in their mountings. Figure 5.2 depicts the setup with twelve iM3501 sensors attached to the ring. On the top left corner, one single iM3501 sensor with its PCB is shown. A cable harness provides the four SPI wires and the SS channel for each sensor. The origin of the coordinate system and its three perpendicular axes are shown in white. Note that the axes align with the coordinate system of the MARS (Figure 4.22). Furthermore, two magnets are depicted for size comparison.

A set of Helmholtz coils is used to validate the properties of the sensors before the actual measurements. Helmholtz coils are can provide a uniform magnetic fields. Its strength $\mathbf{B}$ (in Tesla [T]) near the center of the setup can be approximated as follows [130]:

$$B = 4 \cdot \pi \cdot 10^{-7} \frac{8 \cdot I \cdot N}{\sqrt{125 \cdot R}} \tag{5.4}$$

$\mathbf{I}$ denotes the current running through the coils in Ampere, $\mathbf{N}$ the number of wire loops in one coil and $\mathbf{R}$ the coil radius in meter. In the experiments, a Helmholtz coil with $\mathbf{N} = 154$ and $\mathbf{R} = 200$ mm was used (PHYWE Systeme GmbH und Co. KG, Germany). The remaining free variable is the current $\mathbf{I}$ that is passed through the coils.

To validate the linearity and sensitivity of the sensors, the following experiment was conducted. The sensors were positioned in between the two coils (see Figure 5.3, left). Then, the magnetic background was determined. Superposition can be applied to magnetic fields [131, 132], hence the background can be corrected for by subtracting the measured vector from the data acquired in the following. Next, a current was passed through the coils and the magnetic flux at the sensors was measured. In the next step, the current was raised by a defined value and another measurement was conducted.

Figure 5.3, right, shows the results of the experiment. The theoretical field is shown in blue and the actual measured field is plotted in green. As expected, the measured magnetic flux raises linearly with the raising current. However, it was found that the slope of the sensors is steeper than predicted by Equation 5.4. Note that there is a difference of 10% between the two lines. This discovery is of great importance for
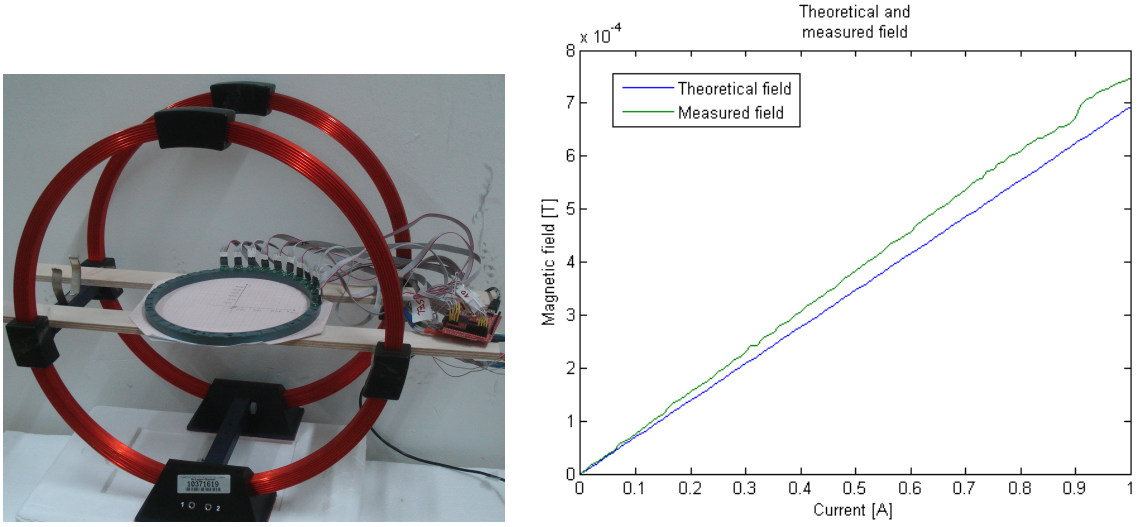
Figure 5.3: *Left: Sensor setup between two Helmholtz coils. Right: Measured and calculated magnetic flux at the sensors between the Helmholtz coils.*

the dipol model based localization and enhances the accuracy of this approach. It is considered in all following calculations.

A welcome side-effect of the experiment is the validation of the rotations of the sensors mentioned earlier. If all sensors are in between the two coils, as shown in Figure 5.3, a similar magnetic field should be measured. If this is not the case, the rotations are not calculated correctly.

The presented sensor setup is used for both, the numerical and the mini lookup table based approach. The conducted experiments and the obtained results are presented in Section 6.6

6 Experimental applications

Various experiments were conducted to evaluate the performance of the MARS (Chapter 4) and the magnetic probe localization (Chapter 5). They will be discussed in this Chapter. First, two general robotic parameters are determined: The absolute accuracy and the repeatability. After that, a detailed analysis of the influence of the MARS on micro-electrode recording equipment is conducted, as electromagnetic compliance is of great importance in the application scenario. Next, an in-vitro analysis of the accuracy of the system in the clinical environment is presented.

Special focus is given to the first clinical application of the MARS. The preparations of the intervention and the safety strategy are explained. Then, the actual surgery is described and the outcome is discussed.

After that, the experiments and results of the magnetic probe localization are described. Note that parts of this Chapter were published in [128, 133, 134, 135, 136].

6.1 Absolute accuracy

Accuracy is one key requirement for the success of neurosurgical interventions (see Chapter 3). The ZD frame from the industrial collaborator inomed Medizintechnik GmbH presents a reliable and approved medical device (see Section 2.2). In the following, an experiment to compare the absolute accuracy of the MARS with the ZD system will be described. The motivation for this comparison is the following: If the MARS outperforms the clinically approved ZD frame, its absolute accuracy is sufficiently high for neurosurgical interventions.

In the actual experiment, the absolute accuracy was determined using an industrial robot (viper s850, Adept Technology Inc., USA) with two perpendicularly oriented video cameras (SPC900, Royal Philips Electronics N.V., Netherlands) attached to its end effector. The position of the industrial robot is used as ground truth for the evaluation of the two systems.

Table 6.1: *Absolute accuracy ZD frame and MARS System*

ZD frame	mean (mm)	std (mm)	max. dev. (mm)
X	0.663	0.217	0.975
Y	-0.117	0.126	0.300
Z	0.773	0.458	1.516
Norm	1.082	0.386	1.801

MARS	mean (mm)	std (mm)	max. dev. (mm)
X	0.077	0.049	0.269
Y	0.140	0.064	0.161
Z	0.141	0.086	0.290
Norm	0.231	0.076	0.334

First, the ZD frame is evaluated. Therefore, the frame is attached to the head ring. Then, the probe is attached to the micro drive unit mounted on the frame. A reference pin is aligned with the intersection of the focal planes of the two cameras. The industrial robot is positioned in a way, that the tip of the probe matches the tip of the reference pin. Figure 6.1 shows the experimental setup.

A cubic workspace with edge length 40 mm is sampled with a total of 27 measurements. On the initial position, image data from the two cameras is saved. After that, the frame is moved manually 20 mm along its first axis. Next, the industrial robot is moved 20 mm along the same axis. Another set of image data is saved and the frame is moved to the next position. This procedure is repeated until the whole cubic workspace is sampled. The same experiment is repeated for the MARS. Note that the MARS is repositioned automatically and that the same points in space were approached by the ZD frame and the MARS.

In the data analysis, the deviation was determined based on the image data. Deviation in X- and Y-axis are directly calculated based on the number of pixels between reference pin and the tip of the probe. The average of the two available values of the Z-axis is calculated. A reference tool with a fixed length is used to determine the conversion between pixels and millimeter.

Table 6.1 shows the mean values and the standard deviation for the ZD and the MARS. Also, the maximal deviation (max. dev.) is listed. The norm or Euclidean distances of the deviations are presented in the last row. In the measurements of the ZD frame,
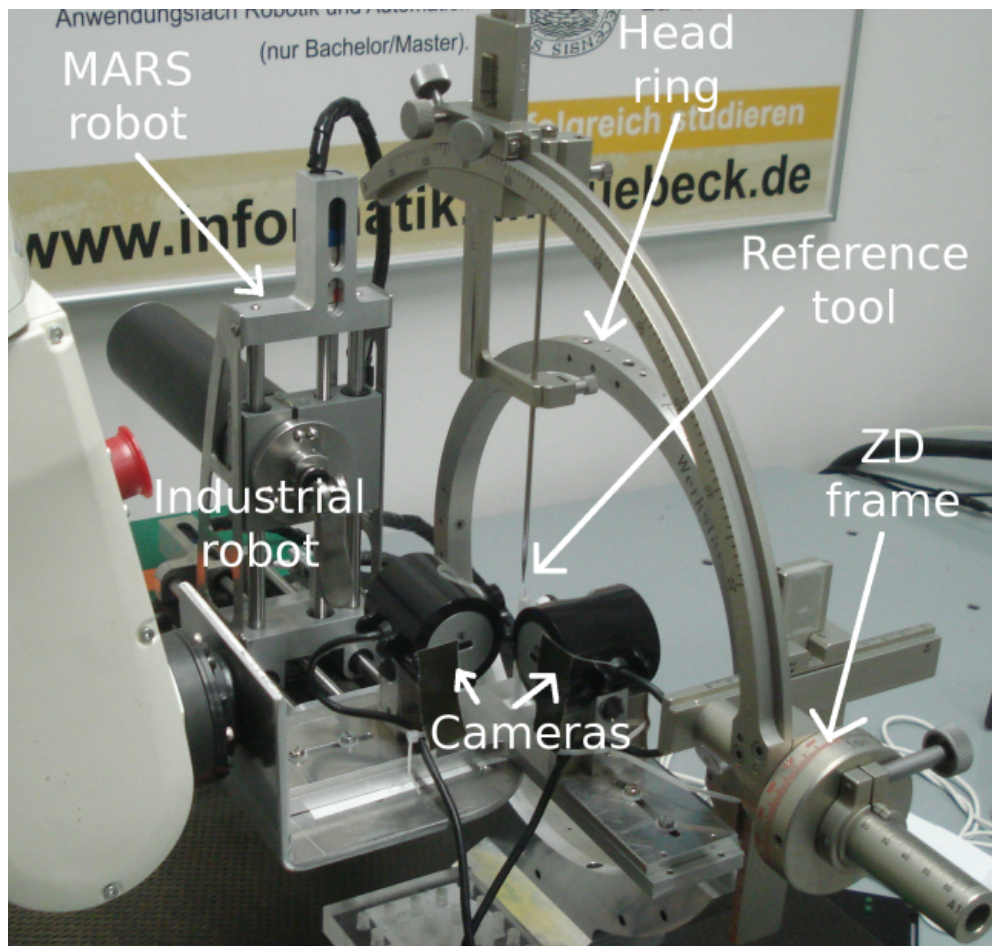
Figure 6.1: *Experimental setup for evaluation of absolute accuracy of the MARS in comparison to the ZD frame. On the left, the industrial robot with cameras attached to its end effector is shown. The head ring is mounted to the ground plate of the MARS. The ZD frame is fixed to the head ring.*

inaccuracies may arise from the manual repositioning after each step.

For the application, two parameters are of great importance: The mean norm error and the maximal norm deviation. For the ZD frame, a mean norm error of 1.1 mm and a maximal error of 1.8 mm was measured. The MARS outperforms the ZD frame substantially: The mean norm error is 0.2 mm and the maximal norm error is 0.3 mm. The presented results allow the conclusion, that the absolute accuracy of the MARS is sufficiently high for the application. Beside the absolute accuracy, the repeatability plays an important role for the clinical application of the system. It is analyzed next.

6.2 Repeatability

For the experiment, the MARS is equipped with a micro drive unit and a micro-electrode is attached to it (both inomed Medizintechnik GmbH, Germany). To measure the repeatability, two DFK31AF03 high-resolution cameras (The Imaging Source Europe GmbH, Germany) are used. They are equipped with objectives (Edmund Optics, USA) and are aligned perpendicular to each other. The foci of both cameras are adjusted to match the tip of the micro-electrode. The diameter of its tip is approximately 0.02 mm. Next, the camera setup is fixed on the ground plate of the robot.

The actual experiment proceeds as follows: On the images of the two cameras, the probe tip is identified with a cross-hair and its position is saved. Two points with a fixed distance of 0.65 mm, the diameter of the shaft of the electrode, are used to calculate the conversion between camera pixel and millimeter. Note that the theoretical resolution of the system is 0.002 mm or 2 μm: 220 pixels correspond to 0.65 mm.

Next, each axis of the robot was randomly moved in the range of -1.5 mm to +1.5 mm and -1.5° to +1.5°, respectively. After that, the robot was commanded to moved back to its initial position. Again, the position of the probe tip was identified on the two camera images using the cross hair. The deviation to the previously identified position was saved. The described procedure was repeated 50 times.

A Lillifors test [137] was used to confirm the Gaussian distribution of the norm error. The mean error was 0.055 mm with a standard deviation of 0.014 mm, a minimal error of 0.029 mm and a maximal error of 0.11 mm were recorded. Table 6.2 gives and overview over the achieved results.

The data was further analyzed. Figure 6.2 depicts the error in millimeter for each of the 50 data points. The errors in XYZ are shown in blue, green and red, respectively.

Table 6.2: *Repeatability of the MARS; Mean, minimal and maximal error are calculated for all items. Standard deviation is only given for normally distributed errors.*

	Mean error	Standard deviation	Minimal error	Maximal error
Norm	0.0551 mm	0.0136 mm	0.0285 mm	0.1062 mm
X	-0.0210 mm		-0.0555 mm	0.0348 mm
Y	0.0043 mm		-0.0500 mm	0.1000 mm
Z	-0.0120 mm		-0.0254 mm	-0.0020 mm
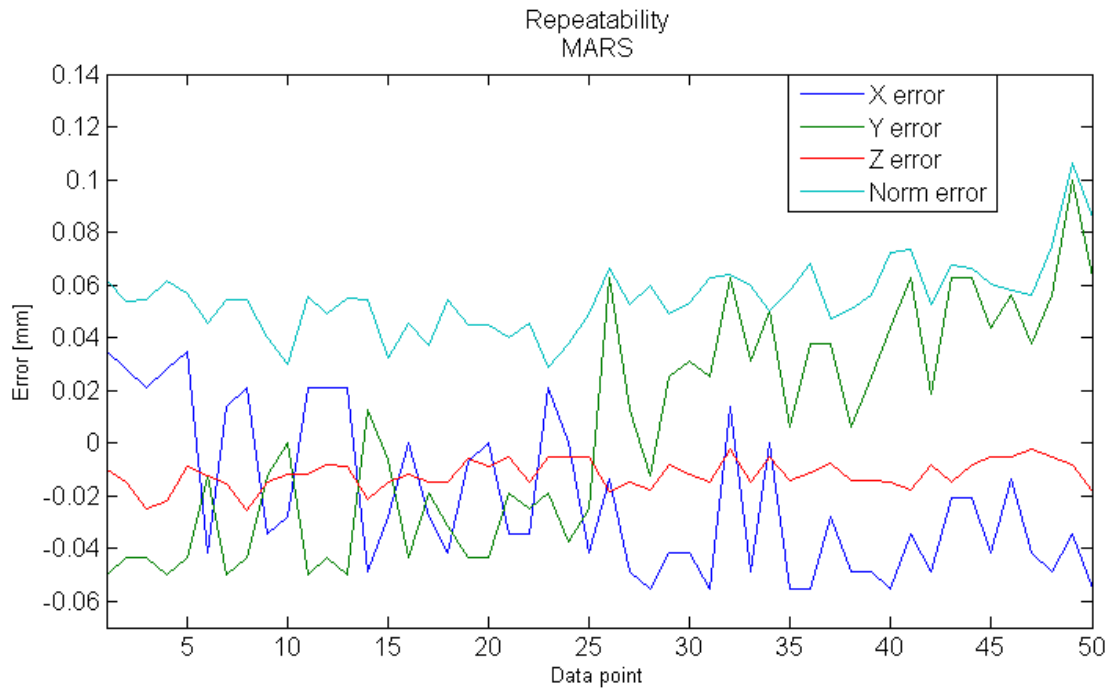
Figure 6.2: *Repeatability of the MARS. Blue: Error in X-axis, green: Error in Y-axis, red: Error in Z-axis, cyan: Norm error.*

The norm error is plotted in cyan.

The norm error and the error in the Z-axis are constant throughout the measurement. However this is not the case for the X- and Y-axis. Instead, the error is alternating most likely due to the backlash of the translational axes drive trains, e.g. clutches or gears. The backlash is suppressed for the Z-axis as it is under constant strain by gravitation forces. Although this backlash is undesirable, it does not cause any problems as the error caused by the backlash is in the scope of 0.01 mm. It can be neglected for the application.

It is not possible to give reliable data for the repeatability of manual stereotactic devices because the manual adjustment is the greatest error source and would corrupt the measurements. For this reason, the performance of the MARS is compared to industrial robots. The unidirectional repeatability of an IRB 1600 industrial robot (ABB Ltd., Switzerland) is better than 27 μm [138]. The numbers for the viper s850 (Adept Technology Inc., USA) are in the same order of magnitude: $\pm$ 20μm. The system A73 presents a medical robot for neurosurgery that is based on an industrial robot. Its repeatability is 60 μm [139].

For the MARS, a repeatability of 55 μm was determined. The achieved repeatability is in the same order of magnitude as for industrial robots and better than the repeatability of the medical robot system A73.

6.3 Electromagnetic compatibility

In the treatment of Parkinson's disease, DBS electrodes are implanted in the brain of the patient (see Subsection 1.2). It is of utmost importance, that the electro-magnetic noise of the MARS does not interfere with these electrodes or the equipment used during their implantation. To evaluate this, the following experiment was conducted. A commercially available micro electrode recording system (ISIS MER), in combination with a micro-macro electrode (both Inomed Medizintechnik GmbH, Germany) was used to measure the noise generated by the MARS. Figure 6.3 depicts the experimental setup. The micro-macro electrode is connected to the ISIS MER system and attached to the motorized micro drive unit (see Subsection 4.2.6). The motorized micro drive unit is mounted to the r2 axis. The MARS and the micro drive are controlled via PC. To simulate the conductivity of brain tissue, the tip of the electrode was immersed in physiological saline. The saline was positioned on the ground plate of the MARS. The position is identical to that of the patient's head in an actual intervention.
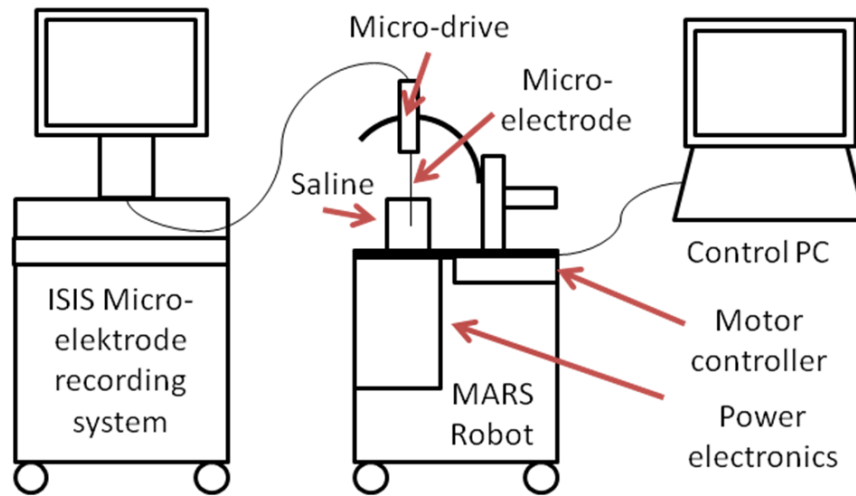
Figure 6.3: *Schematic of the experimental setup; left: ISIS MER (Micro electrode Recording) system; center: the MARS robot with saline solution, micro electrode and micro-drive; right: MARS control PC.*

With this experimental setup, a total of five measurements was conducted. For all measurements, the sampling frequency was 25 kHz. The measurement time was between 30-140 s.

First, the background noise generated by electronic equipment in the room not involved in the experiment was determined. Therefore, the AC/DC power converters of the robot, its controllers and motors, as well as the control computer were not powered.

Second, the AC/DC converter and the control PC were connected to power. The controllers and motors were activated and a second noise measurement was conducted.

Third, all five motors of the MARS robot were activated, and the robot was moving during the data acquisition.

Forth, the influence of the motorized micro drive unit on the micro electrode was evaluated. This is of special interest, as the motorized micro drive unit is closest to the micro electrodes. Note that the motors of the MARS robot were activated, and that the robot was not moving during the measurements. The motorized micro drive, however, was moving at a constant speed.

Fifth, the motors of the micro drive as well as the motors of the MARS were activated, but they were not moving. Stimulation pulses from the ISIS MER system were delivered to the saline via the micro electrode (4 mA). This measurement was done to determine the influence of the current of the micro-electrodes on the motors, encoders
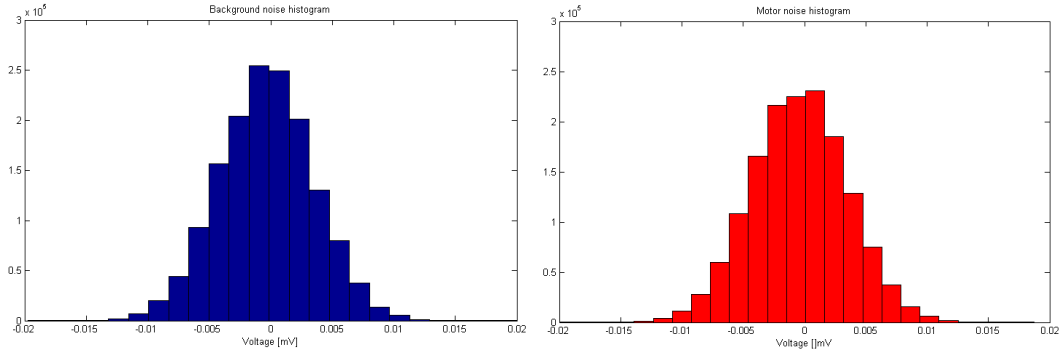
Figure 6.4: *Electro-magnetic interference caused by the MARS. Left: Background noise. Right: Noise generated by the robot.*

Table 6.3: *Electromagnetic noise of the MARS robot*

Description	Mean [mV]	Std. [mV]	Max. [mV]	Min. [mV]
Background	-0.000360	0.0038	0.0211	-0.0197
AC/DC	-0.000399	0.0039	0.0212	-0.0203
Movement	-0.000416	0.0039	0.0175	-0.0183
Micro-drive	-0.000422	0.0039	0.0179	-0.0196
Stimulation	-0.000415	0.0039	0.0176	-0.0184

and controllers of the MARS robot during stimulation.

Figure 6.4 shows two histograms of the recorded voltages. On the left the results from the background measurement are depicted and on the left those of the motorized micro drive unit measurement. Analysis of the histogram data shows a normally distributed signal. The applied Fourier transformation revealed no distinguishable peaks in the frequency spectrum. Note that the same was found for the remaining three measurements. Hence, the measured noise can be classified as Gaussian normal distributed white noise.

Table 6.3 summarized the results from the five measurements. The first column provides the name of the measurement. Then, the mean value and standard deviation of the measured electric signal in mV are presented. The two last columns give the maximal and minimal measure voltage (also in mV).

Table 6.3 shows, that the standard deviation for all five measurements is the same (0.0038 mV). The biggest mean difference between the background measurement and the other four is found for the motorized micro drive measurement. The absolute difference here is 0.000062 mV or 0.062 μV. The maximal and minimal measured
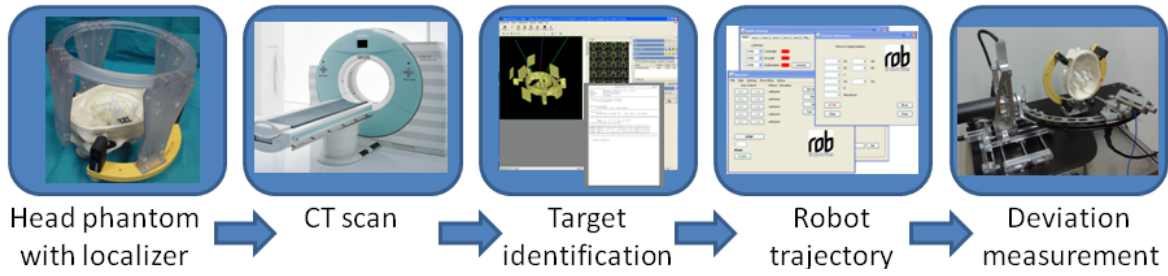
Figure 6.5: *Sequence for the experiment to determine the application accuracy of the MARS (left to right): Head phantom with target pins and attached localizer; CT scan of the head phantom; Target identification with PraezisPlus surgical planning software (TatraMed spol. s r.o., Slovakia); Calculation of the trajectory of the robot; Measurement of the position deviation after robot positioning*

value also change slightly, when compared to the background.

However, these changes are marginal when considered in the context of the application. Depending on the brain-area, patient and electrode, the signal amplitude is approximately 0.1 mV with a firing rate of up to 80 Hz [140]. Hence, the difference in signal voltage caused by the MARS of 0.062 μV can be neglected. In the analysis of measurement five, no influence of the ISIS MER system on the MARS was found.

The presented data allows the conclusion that the MARS does not interfere with the ISIS micro electrode recording device and vice versa. The MARS is therefore suitable for micro electrode recordings.

6.4 Application Accuracy

The application accuracy presents a mean to compare various neurosurgery systems with each other. It is a measure of how well the systems work in the daily clinical use. The measurement of the application accuracy considers all error sources that may lead to faulty positioning of the probe in the brain of the patient.

It follows a common pattern depicted in Figure 6.5: A phantom is equipped with artificial targets. A stereotactic base unit (e.g. a head ring) is fixed to it. A localizer unit is fastened to the base unit. Next, a 3D image of the phantom is acquired. After that, a surgical planning software is used to identify the targets and to plan the corresponding trajectories. Then, the stereotactic device is positioned to match the targets. In the end, the deviation between the probe tip and the targets is measured.

One limitation of the application accuracy is the resolution of the imaging modality. When the first application accuracy measurements were published in the 1990's [36], the resolution of both MRT and CT scanners were much lower than today. This leads to much higher accuracy in the later published studies, including this work. This fact needs to be considered in the following.

6.4.1 Experimental setup

The experiment comprises five steps. First, a commercially available head phantom was equipped with six sharp tipped plastic rods, representing the targets. A ceramic head ring (inomed Medizintechnik GmbH, Germany) was fixed to the phantom using four pins. Next, a CT localizer was fastened to the ceramic ring. The localizer is needed by the surgical planning software to identify the transformation between the head and the stereotactic aiming device (see Subsection 2.1).

Second, a CT scan of the phantom head was acquired using a Siemens Somatosom scanner with a slice thickness of 0.40 mm and an uniform in-plane pixel distance of 0.5625 mm.

Third, the targets were identified using the PraezisPlus 3.1 (TatraMed spol. s r.o., Slovakia) surgical planning software. The registration between stereotactic ring and patient was calculated by the software. After that, the six target points were identified on the corresponding CT slices and the stereotactic coordinates of the target points were calculated by the software.

In the forth step, the target trajectories for the MARS were determined. Based on the position of the six target pins, a total of 54 trajectories was calculated. For each of the two rotational axes three different angles were approached: -15°, 0°, +15°. This results in nine different poses per pin. After the target and trajectory planning, the head phantom was attached to the ring fixture on the ground plate of the robot. Note that no further registration, e.g., by using a tracking system, is required.

In the fifth and last step, the deviation between the probe tip and the target was measured. Therefore, a micro drive unit with a macro electrode was attached to the interface at the r2 axis of the robot. The tip of the probe was monitored with two perpendicularly oriented cameras. Then, the robot was commanded to move to the first target. Once it came to a hold, its position was saved. Next, the amplifiers of the robot were disabled and it was manually moved until the tip of the probe aligned with the target. Once the tips were aligned, the new position of the robot was queried
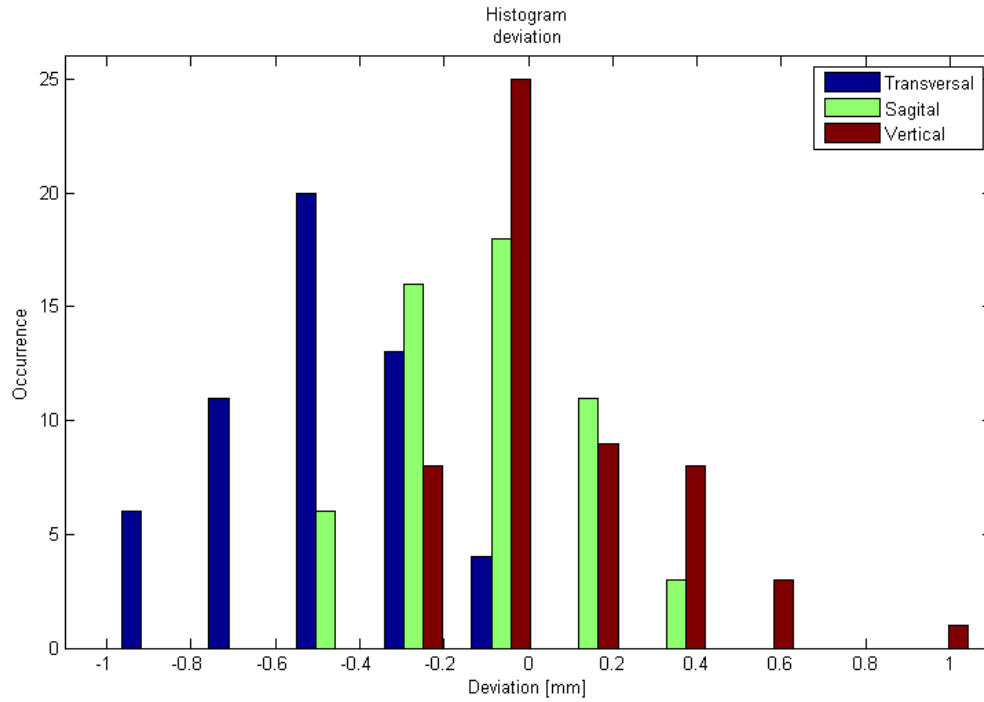
Figure 6.6: *Histogram of the 54 deviation vectors. The deviation in transversal direction is plotted in blue, sagital in green and vertical in red.*

and compared to the previously saved position. The deviation vector is calculated by subtracting the two positions and the results are saved.

The measurement was repeated five times, resulting in a total of 270 trajectories. To compensate for measurement inaccuracies, the average values for the 54 different trajectories were calculated.

6.4.2 Results

The distance vectors between the desired and actual positions of the 54 trajectories were calculated. The histogram plot in Figure 6.6 shows the distribution for the transversal axis in blue, for the sagital axis in green and for the vertical axis in red. Next the mean values and the standard deviations for all axes were determined. Table 6.4 gives an overview of the determined parameters. Note that a Lilliefors test [137] was performed to confirm the Gaussian distribution for the three axes at a significance level of 95%.

A mean norm error of 0.60 mm was found. The transversal direction showed the

Table 6.4: *Measured position deviations of the MARS robot. Mean value (mean), standard deviation (std.), minimal deviation (min.) and maximal deviation (max.).*

	Mean	Std.	Min.	Max.
Transversal [mm]	-0.49	0.23	0.02	1.00
Sagital [mm]	-0.10	0.20	0.00	0.52
Vertical [mm]	0.07	0.26	0.01	1.08
Norm [mm]	0.60		0.07	1.09

greatest absolute mean error with 0.49 mm. In vertical direction, the smallest mean error was found with 0.07 mm. The standard deviation is around 0.22 mm for all directions. Note that no standard deviation can be calculated for the norm values, as it is not Gaussian distributed. Instead, the error for the 68.27th and 95.45th percentile was determined: 0.43 mm and 0.65 mm, respectively. They correspond to $\pm\sigma$ and $\pm2\sigma$ intervals in Gaussian distributions.

Figure 6.7 shows the position deviations for transversal, sagital and vertical axis and the norm deviation. Note that there is a periodicity in the three perpendicular axes. The reason for this might be small errors in the calibration.
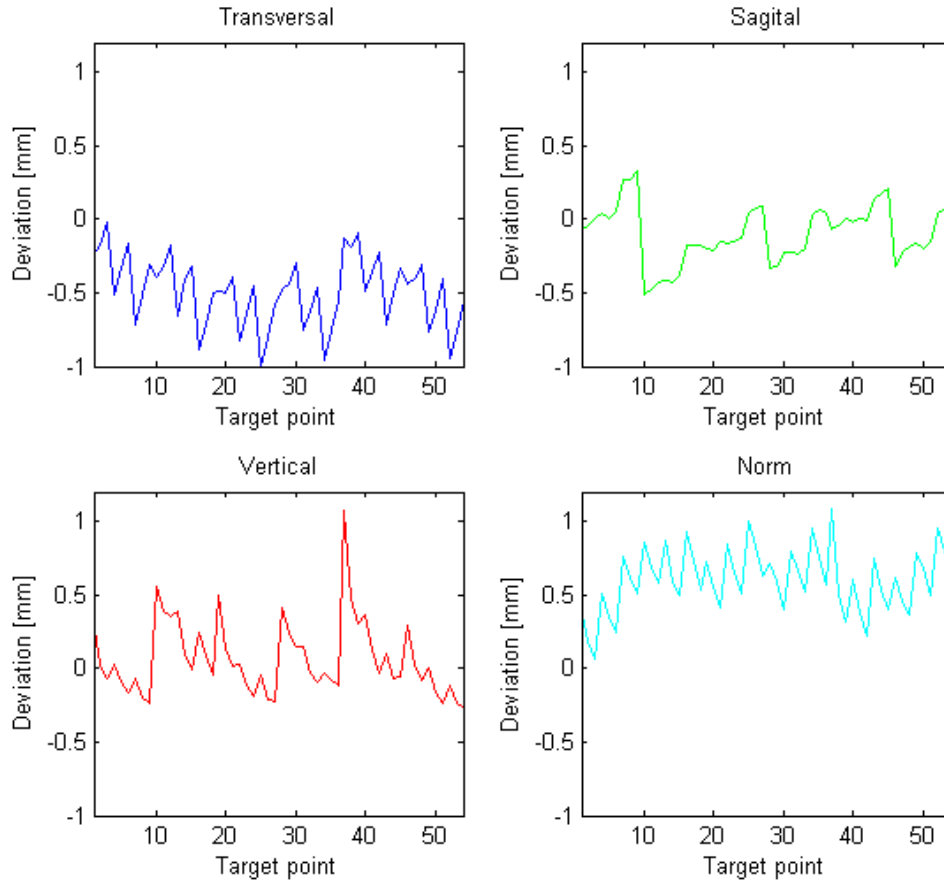
Figure 6.7: *Deviations for XYZ-axis and norm deviation. The position is given on the X-Axis, the deviation on the Y-Axis. The transversal deviation is plotted in blue, the sagital in green and the vertical in red. The norm or Euclidean deviation is plotted in cyan.*

6.5 Clinical evaluation

After the thorough validation of the accuracy and the compliance of the MARS with OT equipment, the robot is clinically evaluated. Tumor biopsies present the simplest stereotactic intervention, as the required accuracy is low when compared to DBS (see Chapter 1). For this reason, the performance of the MARS in an actual intervention is evaluated in a tumor biopsy. The intervention was performed at the UKSH clinic of neurosurgery in Lübeck.

6.5.1 Safety

As the first clinical application of a robotic system entails risks for the patient, a number of preparatory steps was taken to minimize the risk. In close collaboration with inomed Medizintechnik GmbH and the neurosurgeons, the following measures were realized.

In the intervention, the ceramic head ring from inomed Medizintechnik GmbH was used. A ZD stereotaxy system was held available as backup system (see Section 2.2). It is fully compatible to the ceramic ring used in the intervention. If the robotic intervention was not possible or needed to be aborted, the manual system could be used. In this way, the surgeon could always finish the intervention. To provide additional safety in case of the manual intervention, a target point simulator for the ZD system was available. Its axes can be adjust to match the target point. The ZD system can be attached to the target point simulator and its assembly and settings can be validated. A stereotaxy expert from inomed Medizintechnik GmbH attended the intervention and its preparation. He is trained in the handling of the surgical planning software and the manual backup equipment. If the intended use of the software or the equipment should be unclear, he could always assist the surgeons.

The functionality of the MARS and its software was carefully evaluated days before the surgery. The patient agreed in writing on the use of a non-certified medical robot for the intervention.

6.5.2 Preoperative preparations

The software for the MARS was installed on a notebook PC. The following calibration steps were performed on that PC: First, the initial position of the system was determined with the tool described in Subsection 4.4. Second, the manual scales were
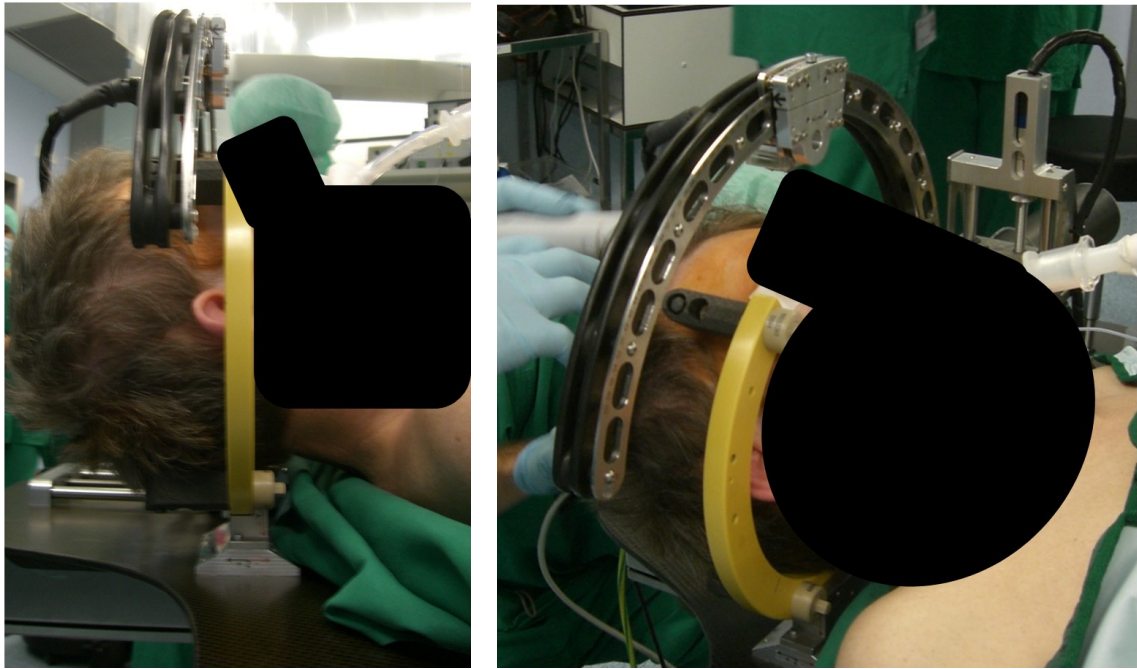
Figure 6.8: *Fixation of the ceramic head ring to the MARS ground plate.*

adjusted to match this initial position. Third, the calibration of the robot was validated using the target point simulator (see Subsection 4.2) and the actual instruments for the intervention.

The day before the intervention, the MARS was attached to an operating table in the OT preparation room. The stability of the connection was controlled carefully. Next, the robot was activated and moved to its initial position. This was validated with the manual scales. The instruments and all other equipment in direct contact with the patient were sterilized.

The surgical intervention followed the generic workflow described in Section 1.1. In preparation of the surgery, the patient was first anesthetized. Next, the ceramic head ring was fixed to the skull using four pins. The pins were carefully selected such, that they do not exceed the outer diameter of the ceramic head ring. This is to prevent the head ring from jamming in the MR head coil.

All pins were tightened with a torque wrench to guarantee a rigid connection between skull and head ring. Next, the localizer was mounted to the ring and the MR head coil was positioned over the head and localizer. A Philips Achieva 1.5 T (Royal Philips Electronics N.V., Netherlands) scanner was used to acquire a 3D MR image. The slice distance was set to 1.0 mm. The image data was transferred to the Picture Archiving

and Communication System (PACS) of the hospital.

After the imaging procedure, the patient was transported to the OT. There, he was transferred to the operating table on which the MARS had been installed. Next, the head ring was fixed to the ground plate of the MARS using the ring mounting. Figure 6.8 depicts this process. The ring was aligned with the mounting and the screws that fixate the position of the ring were tightened. The rigidity of the connection between the ring and the MARS was validated.

Next, the MARS was covered with sterile material. A camera drape was positioned over the arc. Then, various sterile covers were attached to the main structure of the robot. A window was cut into the camera drape at the location of the interface of rotational axis r2.

The target point for the biopsy was planned next. Therefore, the imaging data was loaded from the PACS into the PraezisPlus 3.1 software. The software automatically determined the transformation between the imaging and the stereotactic coordinate system. After that, the surgeon selected the target location on the slice images. The software calculated the coordinates of the target in the stereotactic coordinate system. The target coordinates were manually transferred to the software of the MARS. Then the robot was activated and moved to the planned position.

Next, the probe feeder was mounted to the interface of rotational axis r2. The feeder was moved to its initial position and a guiding tube was attached to it. It pointed to the location of the trepanation (Figure 6.9, top). This position on the skull was marked and the robot was moved out of the way of the surgeon.

6.5.3 Operation

The surgeon opened the skull bone with a surgical drill at the previously marked location. Next, the robot was moved back to the target position. The longitudinal axis of the probe feeder pointed towards the trepanation (Figure 6.9, bottom).

First, the guiding tube with mandrin was fed into the brain. Once it had reached its final position it was fixed by tightening a screw on the probe feeder (Figure 6.10, top). Second, the mandrin was removed and the biopsy instrument was inserted. Here, alligator forceps from inomed Medizintechnik GmbH were used. Third, the specimen was collected (Figure 6.10, bottom).

Multiple samples were collected at the target location. To compensate for brain shift or misalignment, further samples in proximity to the target were collected. Therefore,
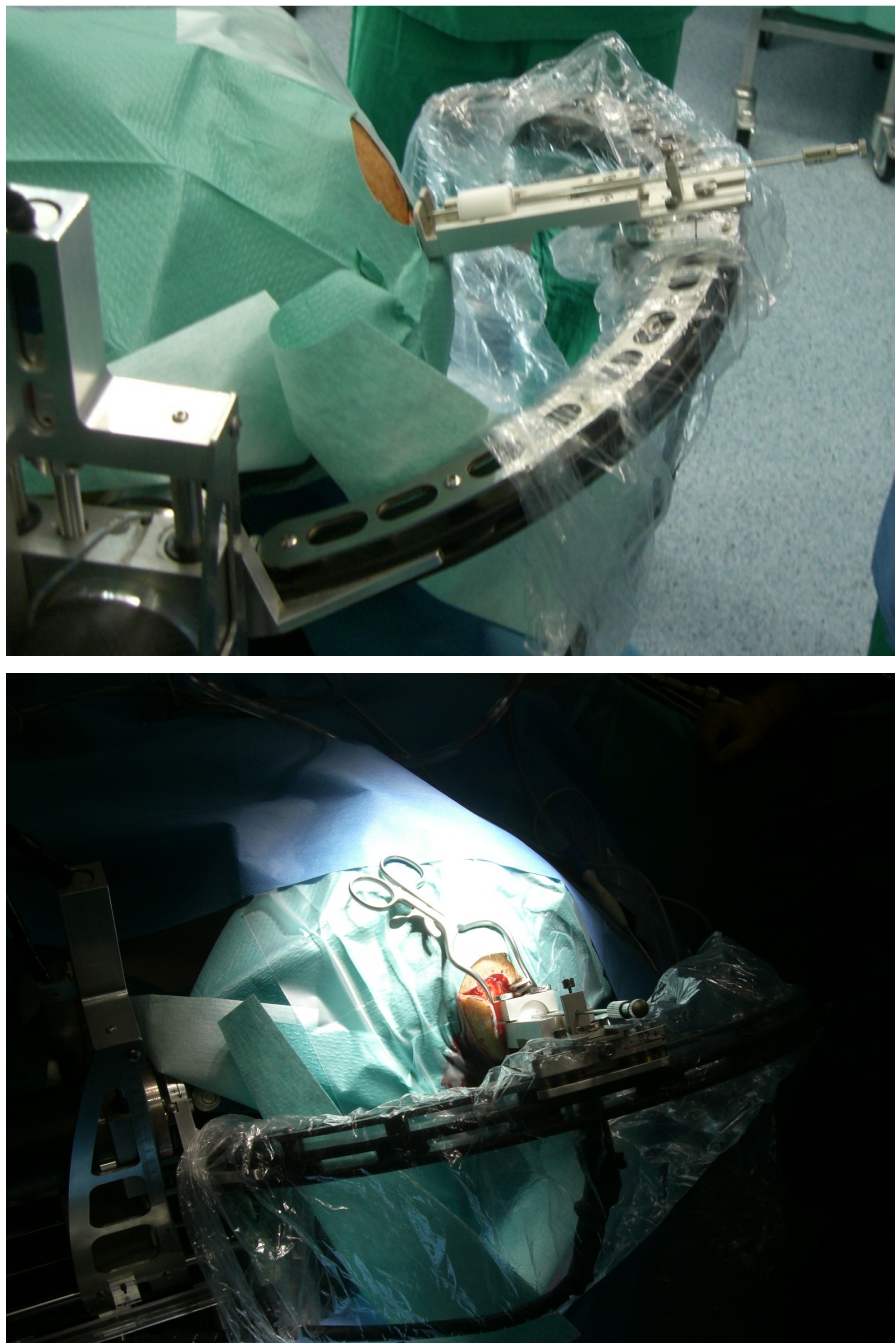
Figure 6.9: *Top: MARS sterile covered with probe feeder attached. The guiding tube points towards the location of the trepanation. Bottom: Skull bone opened and MARS in position for the insertion of the guiding tube.*
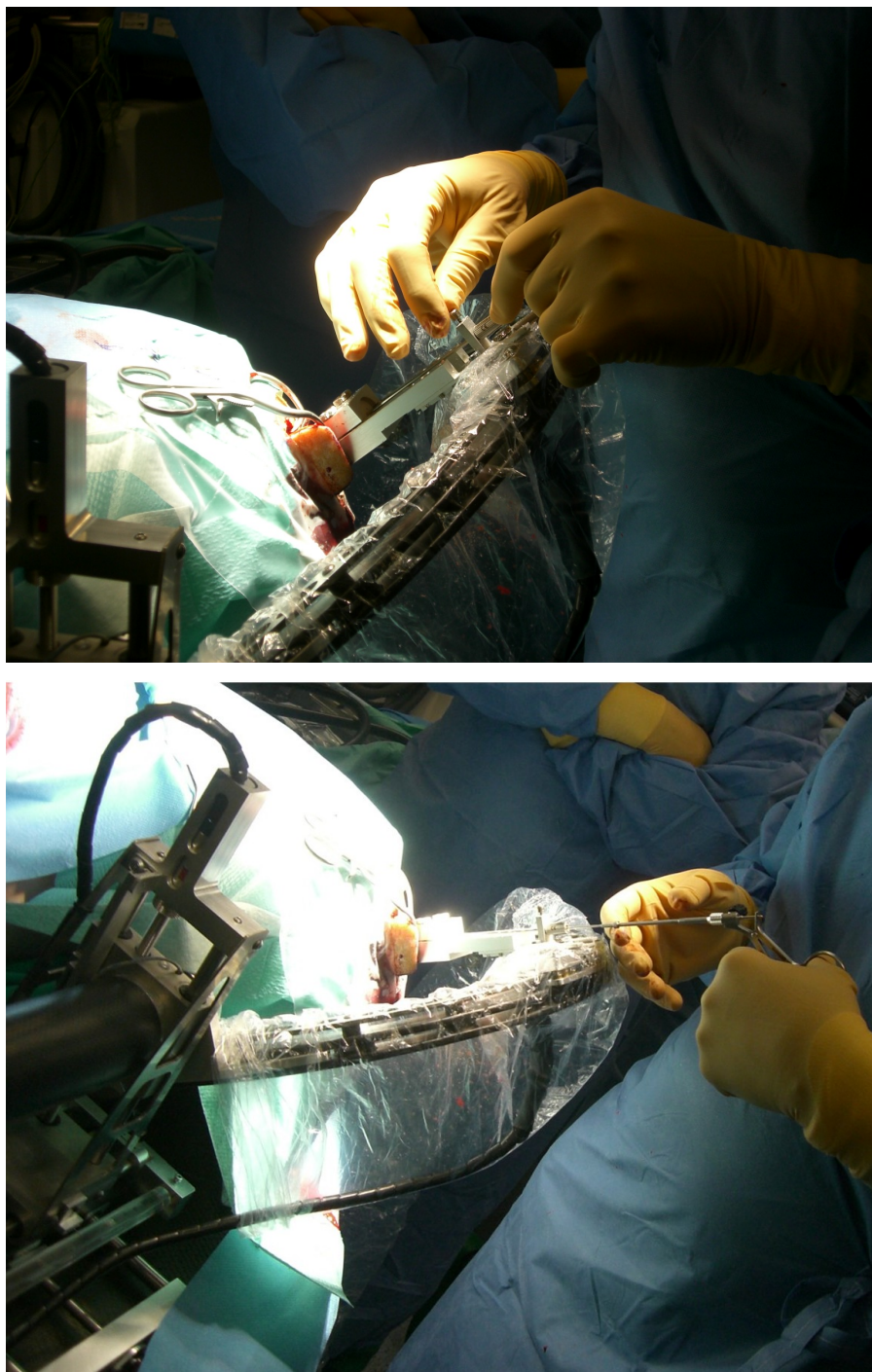
Figure 6.10: *Top: Insertation of the guiding tube with mandrin. Bottom: Collection of the first specimen using alligator forceps.*

the instrument was fed stepwise 1 mm further into the tissue. After each step, a specimen was collected.

6.5.4 Postoperative steps

After the collection of the last sample, the guiding tube was removed from the patient's brain. Next, the robot was repositioned such that it would not interfere with the wound treatment. The trepanation was closed and the skin was sutured. In the next step, the pins were removed from the stereotactic ring. Then, a post-operative cranial CT scan was performed. It was without additional pathological findings and indicated, that the biopsy was collected at the previously planned location. Then, the patient was transferred to the intensive care unit. Five days after the intervention, he was released from hospital.

To conclude, the MARS was successfully employed to collect multiple biopsy samples from the brain of the patient. It was integrated into the surgical workflow without difficulties. However, this first application identified some points for further improvement. They are discussed the next chapter.

6.6 Magnetic probe localization

This section describes the experiments and corresponding results for the two localization algorithms introduced in Chapter 5. The last part summarizes the properties of the methods.

6.6.1 Numerical solution

The numerical solution algorithm is used to localize a small ($\varnothing 3 \times 6$ mm) permanent magnet. The experimental setup is similar to the one shown in Figure 6.11, instead of the macro electrode a permanent magnet was attached to the MARS.

A number of experiments were conducted to evaluate the accuracy and other parameters for the localization algorithm. Therefore, a cubic workspace with edge length 50 mm was sampled stepwise by the MARS. The step width was 10 mm for all axes resulting in $6^3 = 216$ nodes per cube. At each node, the magnetic flux was saved along with the position of the robot. This information is later used as ground truth data to determine the deviation of the algorithm.

Table 6.5: *Position deviations for various distances from the origin. The dimensions of the workspaces are $50 \times 50 \times 50$ mm^3 for all distances. Magnet aligned with Z-axis*

Start pos. [mm]		68.27th perc. [mm]	95.27th perc. [mm]	Max. error [mm]
[0 0 0]	X	3.2	5.6	5.4
	Y	2.1	4.3	5.7
	Z	3.3	5.4	6.4
	Norm	5.4	7.4	9.8
[0 0 25]	X	1.6	3.1	4.5
	Y	1.7	3.4	4.7
	Z	2.9	5.1	5.6
	Norm	4.0	5.9	9.6
[0 0 50]	X	2.3	4.0	5.6
	Y	2.1	3.6	5.0
	Z	2.8	5.5	9.4
	Norm	4.4	6.3	9.6
[0 0 75]	X	3.0	5.6	8.2
	Y	1.7	3.7	6.2
	Z	3.1	6.4	10.9
	Norm	4.8	7.6	11.4

Two sets of experiments were conducted, they differed only in the orientation of the magnet. In the first set, the magnet was aligned with the Z-axis of the magnetic sensor setup. Four cubes were sampled. The starting position for each cube was different, as indicated in the first column of Table 6.5 and Table 6.6. To evaluate the influence of orientation changes on the algorithm, the magnet was rotated by 45° in the second set of experiments. A total of 1 728 localization tasks was performed to evaluate the algorithm.

Note that there is a trade-off between strong sensor signals and accuracy of the dipole model. In order to obtain strong signals, the magnet needs to be in proximity to the sensors. As it is not a point-shaped dipole but has spatial extend, the model fails to predict the correct magnetic flux. This can cause faulty localization results.

Table 6.5 gives the results for the first set of experiments and Table 6.6 for the second.

Table 6.6: *Position deviations for various distances from the origin. The dimensions of the workspaces are $50 \times 50 \times 50 \ mm^3$ for all distances. Magnet rotated 45° about the X-axis.*

Start pos. [mm]		68.27th perc. [mm]	95.27th perc. [mm]	Max. error [mm]
[0 0 0]	X	2.6	6.0	6.0
	Y	2.7	6.1	11.4
	Z	4.1	8.8	13.1
	Norm	6.0	12.2	16.8
[0 0 25]	X	2.8	5.2	6.8
	Y	4.1	9.1	8.2
	Z	7.1	13.5	11.7
	Norm	9.1	14.5	20.2
[0 0 50]	X	2.3	8.5	16.9
	Y	3.4	10.0	16.1
	Z	5.0	8.2	11.7
	Norm	6.6	13.7	21.2
[0 0 75]	X	2.1	4.8	8.1
	Y	4.0	8.0	13.4
	Z	5.3	9.0	9.4
	Norm	7.4	11.3	17.5

The start position with respect to the origin indicated in Figure 5.1 is shown in the first column. Note that the position error is not Gaussian distributed. This was validated using the Lilliefors-test [137]. For this reason, no standard deviation and mean value are calculated. Instead, two percentile values are given: 68.27 and 95.45. They correspond to the 1-sigma and 2-sigma interval in Gaussian distributions. The position deviation is given for the XYZ-axis, also the norm deviation is calculated. The last column indicates the maximal error.

The highest accuracy was found for the second cube of the first set (starting position [0 0 25]) with 68% of the error below 4.0 mm and 95% below 5.9 mm (Table 6.5). The second cube of the second set shows the highest deviations with 68% below 9.1 mm and 95% below 14.5 mm (Table 6.6). The localization error is smaller for the first set of experiments. The achieved results will be discussed in Chapter 7.

Note that the change of orientation of the magnet was limited to $\pm 5°$ in the algorithm which facilitates the localization task. This is in accordance with the application as fast changes of the instrument direction are unlikely in the surgical intervention.

The numerical solution is implemented in MATLAB (The MathWorks Inc., USA). A GUI handles the interaction with the user. The user can connect to the hardware, measure the background and the actual magnetic flux at the sensors. Furthermore, he can can specify which error function to use in the minimization. Also, he can give the start values for the numerical solver. The GUI is used if a small number of localization tasks are performed.

It furthermore includes a simulation tool which calculates the expected magnetic flux at the sensors based on the dipole model given in Equation 5.2. The user has the opportunity to add noise to the sensor values and study the influence on the localization results. A visualization tool shows the expected and measured flux at each sensor. Based on the sensor values, the algorithm determines the position and orientation of the simulated and actual magnet. This localization tool can be used in a surgical intervention or to validate the performance of the system.

6.6.2 Mini lookup table

In contrast to the numerical solution described before, the mini lookup table based approach is not limited to dipole sources, as no analytic description of the magnetic field is required. It can localize arbitrary objects, as long as they generate a magnetic field. In the following experiments, a macro electrode (inomed Medizintechnik GmbH,
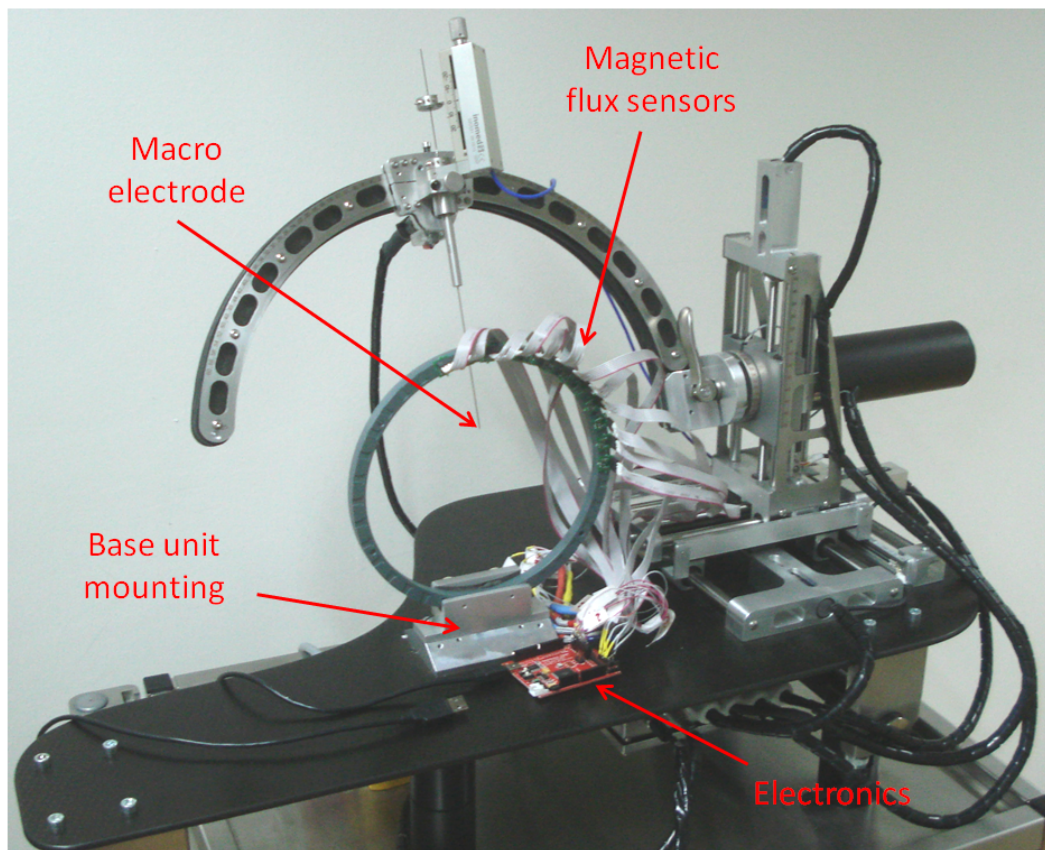
Figure 6.11: *Experimental setup for the magnetic field localization. The sensors are attached to the ground plate of the MARS.*

Germany) was localized. No changes to the electrode were necessary. Instead, the localization is based merely on the intrinsic static magnetic field generated by the probe.

The experimental setup is shown in Figure 6.11. To enhance the magnetic flux generated by the probe, it was magnetized using a NdFeB permanent magnet. Magnetization is achieved by repetitive sweeping of a permanent magnet over the probe. Next, the electrode was attached to the micro drive unit which in turn was mounted to the MARS.

The sensitivity of this localization approach is evaluated first. Therefore, the electrode was moved along the same trajectory ten times. The magnetic flux was recoded and the resulting tables were compared. The travel range of the electrode was from -20 mm to +20 mm with respect to the center of arc and the step width was 0.5 mm. A total of 81 points was recorded. The target point was X=40 mm, Y=30 mm and Z=20 mm with respect to the center of the plastic ring and rotational axis r1 was set to 45°.

In the next experiment, the probe was shifted along the t1 axis by 1 mm and two lookup table were recorded. This was repeated until the probe was shifted by 4 mm from its initial position. The resulting tables were compared to each other and the previously generated ten tables.

The accuracy of the algorithm is evaluated first. Therefore, the data from the ten lookup tables recoded in the first experiment are analyzed. Each table is compared to all others resulting in a total of $45 \times 81 = 3\,645$ localization tasks. The euclidean distance between the 36 dimensional magnetic flux data is used as error metric. A mean error of 0.0269 mm with a standard deviation of 0.365 mm was found. These results proof, that the algorithm can localize probes with very high accuracy.

The mean error and the standard deviation of the error metric contains information for the following analysis. The error is Gaussian distributed, and a mean error of 47.755 nT with a standard deviation of 5.6928 nT was found. Note that especially the mean error is important here. It contains information about the expected noise level of the sensor data.

To validate the performance of the algorithm when confronted with faulty positioned probes, data from the shifted measurements was evaluated next. The original (i.e. not shifted) dataset was used as lookup table. The algorithm was used to localize the points from the shifted measurements in the original table.

The box plots in Figure 6.12 depict the results, the measurements are labeled 1-5. On the left, the error of the localization is given in [mm]. The right graph shows the
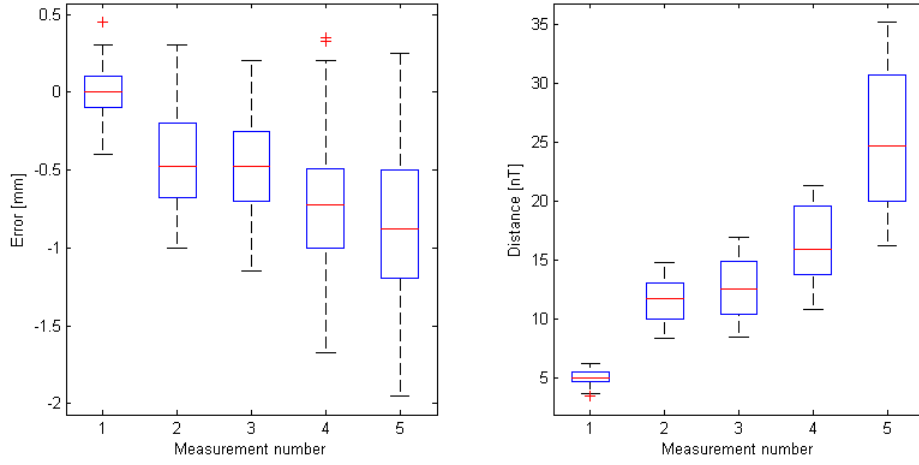
Figure 6.12: *Boxplot of the distances with shifted and non-shifted probe. Measurement 1 shows original data, measurement 2-5 show data for probe shifts of 1-4 mm.*

Table 6.7: *Statistic parameters mini lookup table method. All measurements are compared to the original dataset. m1 is not shifted, m2-m5 are shifted 1-4 mm from the original trajectory.*

	m1	m2	m3	m4	m5
Mean [mm]	0.004	-0.440	-0.469	-0.725	-0.842
Std. [mm]	0.155	0.303	0.314	0.411	0.526
Mean [nT]	49.95	115.32	126.31	164.03	254.98
Std. [nT]	5.69	20.65	26.27	33.59	59.81

residual error in nano Tesla [nT].

Measurement 1 shows the data from one exemplary dataset from the previous experiment (note that data for the other 44 tasks looks similar). Measurement 2-5 show data from the shifted probe experiments (1-4 mm).

Note that the algorithm will always find a nearest neighbor, even if this point is 'far' away. This results in a relatively small mean error and standard deviation (Table 6.7, line 1 and 2) even for data from the shifted measurements. At the same time, the error (given in [nT]) between the measurement and the lookup table data is increasing (Table 6.7, line 3 and 4). To evaluate if the results of the algorithm are correct, this error needs to be considered. It is smallest for the correct table with 49.95 nT and

Table 6.8: *Properties of the magnetic localization algorithms*

	Dipole model	Trajectory definition
Set up time	++	-
Localization accuracy	-	++
Workspace	++	–
Robust against disturbtion	-	-
Computational costs	+	++

increases with the distance to a maximal value of 254.98 nT.

It is clearly visible, that the standard deviation as well as the mean error is smallest for the original data. Both mean error and standard deviation are growing with the distance.

The shown data allows the conclusion, that the algorithm can determine the position of a probe with high accuracy. It furthmore detects the shifting of the probe with great sensitivity. The localization algorithm is very fast, as only a limited number of distance calculations needs to be performed. The presented results proof that the intrinsic magnetic field of a ferromagnetic object provides sufficient information for localization with sub-milimeter accuracy.

6.6.3 Summary

Table 6.8 gives a short summary of the properties of the two localization algorithms. The dipole model based localization does not require any type of calibration or lookup table recordings. Therefore, it is most suitable if the set up time is crucial. Note that the time needed to set up the mini-lookup table algorithm is highly dependent on the number of points.

The accuracy is best for the trajectory definition algorithm. This is not surprising, as the search space is very limited here. One drawback of this method is that deviations can only be described qualitatively, not quantitatively. The accuracy of the dipole model based algorithm depends on the distance to the sensors and the orientation of the magnet. Generally, it is poorer than for the mini lookup table algorithm.

Both algorithms are prone to the introduction of disturbing magnetic fields. If the

disturbance is introduced during the intervention, the algorithms will yield faulty results.

The computational costs are lowest for the mini lookup table algorithm. Here, only a number of possibilities (typically <100) needs to be considered for the localization. One drawback of this is that the algorithm will always give a nearest neighbor, even if the probe is far away from the planned trajectory. The user needs to consider this in the application.

Both algorithms have their advantages and drawbacks and the selection of the best algorithm is strongly dependent on the context in which the system is used.

This concludes the experimental applications of the MARS and the magnetic probe localization. In the following chapter, the properties of the robot and the magnetic localization are discussed.

7 Discussion

In this Chapter the presented work is critically reviewed. It comprises the analyses of firstly, the robotic system and secondly, the properties of the magnetic tracking.

7.1 MARS

First, the design of the system will be covered. After that, the hardware used in the system is critically analyzed. Next, the handling of the robot with the focus on the clinical application is discussed. Then, the accuracy of the MARS is compared to manual and robotic stereotaxy systems. To conclude, the performance of the robot in the clinical evaluation is discussed.

7.1.1 Design

In the design phase, most of the future properties of the system are defined. The MARS presents a hybrid between manual and robotic stereotaxy systems. Some of its properties resemble the manual systems, e.g. kinematic chain, others the robotic devices, e.g. automated positioning. The goal of the MARS development was to combine the advantages of both while avoiding their limitations. With this design paradigm, the robot differs significantly from current robotic and manual systems: No bulky stand as in other robotic systems is required. At the same time, automatic positioning of the probe with high accuracy is possible. In contrast to most of the other robotic systems, the transport of the MARS is simple and can be performed by one single person without difficulties.

The design of the kinematic chain as center of arc affects the performance of the robot, e.g. in terms of accuracy, workspace, etc. As shown in Section 2.2, a great variety of kinematic chains is used in stereotaxy. Although the design of a center of arc kinematic is more challenging than other serial kinematics, it has some advantages. The following two factors were decisive: First, the acceptance of this kinematic chain in the

neurosurgical community is very high. It resembles the manual ZD stereotaxy system (see Subsection 2.2.2) and its handling is intuitive. Second, the ingenious simplicity of the mechanism is convincing. The decoupling of translational and rotational parts of the pose results in a great flexibility of the system. Furthermore, the kinematic calculations and the trajectory planning are facilitated.

Technical difficulties were one major problem during surgery with ROBODOC [88]. To prevent similar problems in the MARS, simplicity in handling and operation were design paradigm. The MARS can always be operated manualy, if the surgeon is unable to cope with the user interface or if errors occur. This is a major advantage when compared to other neurosurgery robots, e.g. NeuroMate or ROSA (see Section 2.3). Here, the intervention needs to be aborted in case of malfunction of the robot.

7.1.2 Hard- and Software

The following list gives an overview over the requirements presented in Chapter 3 and how they are fulfilled:

- **Probe positioning:** The robot is built of a serial kinematic chain with three translational and two rotational axes which results in a total of five degrees of freedom. As rotational symmetric probes are used, arbitrary positioning of the probe in the workspace of the robot is possible.

- **Workspace:** The workspace provided by the system is smaller than for other robotic systems. Nevertheless, it is sufficient for most stereotactic interventions, as it is in the same scope as the workspace of manual systems (see Table 4.3). This comparatively small workspace allows for a compact and highly mobile robot.

- **Accuracy:** High accuracy is one core argument for the use of robotic systems in stereotaxy. In the MARS it is realized by using ball screw systems in the drive trains of the translational axes. Its combination with brushless DC motors with integrated Hall sensors enables a highly accurate positioning of the axes. The resolution of all axes is higher than demanded in the requirements (see Table 4.1 and Table 4.2).

- **Electromagnetic interference (EMI):** MARS is designed to position electrodes in the brain of the patient. It is hence necessary that the robot does not

influence the electrode measurements. This is the case for the MARS: It was validated in an experiment using a micro electrode recording device. No influence of the robot on the equipment was detected (see Table 6.3). Two points are important in this context: First, brushless DC motors exhibit less electromagnetic noise when compared to standard DC motors. Second, only low currents are required to power the motors when compared to other robotic systems as a light-weight kinematic chain was designed. Both facts limit the EMI of the MARS. Hence the robot qualifies for functional neurosurgery, e.g. DBS.

- **Safety:** The probability of faulty positioning of the MARS needs to be minimized. Therefore, two independent position encoders are installed at each axis. In the software, the consistency of their values is validated and the robot is stopped if errors occur. In case of emergency the surgeon needs to access the operation situs as fast as possible. Therefore, he can rapidly remove the arc by opening the quick release fitting. The fast mounting and unmounting of the arc provides an additional safety feature. Furthermore, the power of the axes is limited by the controllers. They cannot overpower the surgeon and he can always stop the movement of the robot manually.

- **Compatibility:** The MARS is compatible to surgical instruments from the industrial partner inomed Medizintechnik GmbH. This reduces the overall costs of the system, as surgeons can continue to use electrodes and probes of the manual systems. The MARS software provides a TCP interface which facilitates the integration in third party software frameworks, e.g. the PraezisPlus (TatraMed spol. s r.o., Slovakia) surgical planning software.

- **Control:** All axes are both, self locking and manually adjustable. These features provide the fundamentals for the hybrid character of the MARS. They allow manual operation without damage to the drive train.

A software with graphical user interface was programmed. It implements the kinematic calculations, safety features, operating modes and other features. To conclude, all requirements specified in Chapter 3 are met by the current system.

7.1.3 Handling

When robotic systems are introduced into the OT, they usually require a safety zone. The zone defines an area which can be reached by the robot and where no equipment or staff reside. For the MARS, an application specific kinematic chain was designed and implemented. As the motion ranges of the axes are adapted to the workspace requirements of stereotaxy, no safety zone around the robot is necessary. This allows the integration of the robot in standard OTs.

The handling of the MARS is further improved by the implementation of the hybrid operating mode. It detects interactions of the user with the system and stops the robot, if necessary. The surgeon can continue in an automatic mode or switch to manual operation. An overview of the properties of the operating modes is given in Table 4.9. Some surgeons miss the tactile feedback when they are using a surgical robot. In surgical interventions with the MARS, the same hardware to open the skull and to forward the probe as in manual stereotaxy is used. They provide the same feedback to the surgeon as in manual interventions. For surgeons who prefer the robot to insert the probe automatically, a motorized micro drive unit was developed (see Section 4.2).

MARS provides various operating modes and the surgeon can switch between the modes via software. If he thinks that the robot is not moving correctly, or if an unexpected obstacle is in the way of the robot, he can stop it. In all cases, the surgeon can continue the intervention in the manual mode.

The MARS is transported on a modified instrument table. This allows for quick and easy relocation of the system. For the intervention, it is attached to a standard operating table. A specially designed mechanism interfaces with the side rails of the table. Thanks to this approach, no rigid and bulky stand is required.

7.1.4 Repeatability and application accuracy

Note that the application accuracy depends on the resolution of the 3D imaging. The enhanced accuracy in recently published studies is partially due to the higher resolution of new scanners.

In the measurement of the application accuracy of the MARS, a mean position deviation of 0.60 mm was found. The 68.27th (0.43 mm) and the 95.45th (0.65 mm) percentile were determined. They correspond to $\pm\sigma$ and $\pm2\sigma$ intervals in Gaussian distributions. The maximal occurring error was 1.09 mm.

Table 7.1: *Repeatability and application accuracy of various neurosurgical tools*

Device	Repeatability	Mean error	Minimal error	Maximal error
MARS	0.06 mm	0.60 mm	0.07 mm	1.09 mm
PathFinder	0.40 mm	2.70 mm	1.80 mm	3.20 mm
NeuroMate		0.86 mm		
ZD system		1.08 mm		1.80 mm
RM system		0.60 mm		
System A73	0.06 mm	0.82 mm	0.40 mm	1.43 mm
Nexframe		1.25 mm		

Manual stereotactic frames show a mean norm error between 1.2 mm and 1.9 mm [36]. In [61], the application accuracy of the NeuroMate stereotaxy robot is analyzed. For the frame based configuration, a mean error of 0.86 mm with a standard deviation of 0.32 mm was found. In the same study, the accuracy of the manual ZD frame was analyzed. A mean error of 1.17 mm with a standard deviation of 0.25 mm was reported. This finding corresponds to the measurements conducted in the scope of this work given in Table 6.1. A mean error of 1.082 mm and a maximal error of 1.8 mm was measured.

In [141] the accuracy of the RM manual stereotactic frame was analyzed. The target planning was based on a CT scan with 2 mm slice distance. A mean error of 0.6 mm was found. The application accuracy of the PathFinder neurosurgical robot is measured in [63]. Its repeatability is 0.4 mm, the mean positioning error is 2.7 mm ranging from 1.8 mm to 3.2 mm. Rachinger et al. [139] analyze the accuracy of the system A73, a robot for stereotactic neurosurgery. It is based on a RV1a industrial robot (Mitsubishi Electric, Japan). In a phantom trial, its accuracy was found to be 0.816 mm (ranging from 0.40 mm–1.43 mm). The repeatability of the robot is 0.06 mm. The application accuracy of the frameless stereotaxy system Nexframe (Medtronic Inc., USA) is discussed in [44]. The mean localization error is 1.25 mm with a standard deviation of 0.57 mm.

Table 7.1 summarizes the repeatability and the absolute accuracy of various neurosurgical systems. Note that not all data is available for all systems. The first column gives the repeatability of the system, the three remaining columns indicate the parameters for the application accuracy.

The MARS is on a par with or superior to its peer group in all mentioned criteria.

This allows the conclusion, that the overall accuracy of the MARS is sufficiently high for neurosurgical interventions.

7.1.5 Clinical evaluation

In the clinical evaluation of the system, a tumor biopsy was performed. The results of the intervention are discussed on the basis of the following aspects: Mechanical setup and connections, sterility, planning, robot positioning, workspace, probe feeding.

The MARS was installed on the operation table without difficulties. It did not interfere with the handling of the table. The connection between the MARS and the side rails of the table was stable. The fixation of the head ring on the ground plate of the robot was challenging because the head of the patient covered the fixation screws. They were hence not easy to reach and tighten. Furthermore, the current system only provides one mounting angle for the ring. Depending on the fixation of the ring on the head, this can be unergonomic for the patient. A possibility to adjust the angle needs to be integrated in a future version of the mounting. Furthermore, a new mechanism to fix the ring needs to be desinged.

Sterility was provided by draping the main part of the robot. Additionally, a plastic cover was installed over the arc of the robot. This proved to be challenging, as the cables for rotational axis r2 need to be covered, too. They are bendable only to a certain degree which causes problems in the covering. As a consequence, a new cable guiding for this axis needs to be designed and implemented.

The planning of the target point and the trajectory in the surgical planning software worked trouble free. The manual transfer of the target coordinates to the software of the robot generally presents a potential error source. It is therefore desirable to integrate the MARS further into the planning software. Therefore, a TCP interface is integrated in the software of the system.

The positioning of the MARS was too slow in the eyes of the surgeons. Higher speeds are possible with the current hardware. However, they present a potential threat to the patient. A compromise between speed and safety needs to be found in collaboration with the surgeons.

The workspace of the MARS is not equal to the workspace of the ZD system. Hence, not all configurations of the ZD can be transferred to the MARS. This is a limitation, especially for targets situated at the outer end of the brain. In a future version, the workspace needs to be enlarged to match the manual ZD system.

The mounting of the probe feeder to the MARS worked without trouble, however one limitation became visible. The clearance between the skull and the probe feeder was very small (see Figure 6.9). This is a problem, especially for targets deeper inside the brain as the clearance would reduce further or the target might even not be reachable. As a consequence, a new probe feeder needs to be designed. The interaction with the surgical tools (guiding tube, crocodile forceps) worked as planned. The specimens were collected without difficulties.

Several points to further improve the MARS were detected in the scope of the clinical evaluation. Their implementation is ongoing work at the institute. Beside these mentioned drawbacks, the surgical intervention with the MARS was a success.

7.2 Magnetic probe localization

The localization of probes based on their static magnetic field presents a promising new method for intracranial probe monitoring. The introduction of this technique to the field of stereotactic neurosurgery is one major contribution of this thesis. No ionizing radiation or active electronics are required. Instead, the signal generation is a physical property of the probe, and hence fail-safe. The simplicity of the idea yields various medical applications, e.g. motion tracking or instrument monitoring.

In the scope of this work, two localization algorithms were implemented:

- **Numerical solution:** The model based approach assumes, that the magnetic source is a punctual dipole. Hence, the numerical solution can only be used to track small permanent magnets. The dipole assumption bears limitations in accuracy, as the actual source has a spatial extent. Furthermore, the material properties and the surface of the magnet include imperfections which are not considered in the model. The differences between an ideal dipole and the actual magnet leads to inaccuracies in the localization. On the pro side, the algorithm requires little information. Only a starting point for the numeric solver is required, all other information is provided by the model. This makes the model based localization the fastest to set up.

- **Mini lookup table:** For the application in stereotactic neurosurgery, the mini lookup table based approach yields the best results: It combines high accuracy with fast setup. One drawback is, that the direction of the deviation cannot be specified. There is no need to modify the probes, e.g. by integration of a

permanent magnet. Instead, the algorithm works with the magnetic field generated by the ferromagnetic material. Future applications, both in the medical and non-medical fields are possible with this approach. One could for example monitor the position of a robotic arm used for micro-assembly tasks with great accuracy and without the need for further devices. Other applications are the monitoring of scalpels, screw-drivers, endoscopes or needles.

Both methods share the following points: Ferromagnetic objects or strong electric currents in proximity to the sensors can cause interferences with the signal. This can result in a faulty localization of the probe. Note that the currents required to power the axes of the MARS do not influence the measurements.

In a real neurosurgical setup, the problem hardly exists. Quick changes in the position of the probe do not occur during surgery. Hence, the expected magnetic flux changes are small. If, however, they should exceed a threshold, the user is warned that an external flux source was introduced.

Due to manufacturing tolerances, there is a variability in the sensitivity of the magnetic flux sensors. This sensor noise results in inaccuracies in the localization.

The selection of the appropriate localization method depends on the application and the context. Table 6.8 summarizes the properties of the two presented algorithms.

Some limitations need to be considered when comparing to the systems described in Section 2.5. The work space of the systems is not uniform, neither are the permanent magnets. The results obtained with the numerical solution in this work are in the same range as for the presented systems (see Table 2.5 and Table 6.5). The mini lookup table algorithm outperforms the other systems by far. However, the work space used in the algorithm is very limited.

The integration of the magnetic probe localization into the MARS greatly enhances the system. With this magnetic tracking, the positioning of instruments and probes can be monitored intraoperatively. The workspace of stereotaxy is small compared to other surgical interventions. This is beneficial for the magnetic probe localization, as the signal decays rapidly with distance. The magnetic probe localization is a handy tool for stereotactic interventions as it does not require great changes in the instruments and the surgical procedure. At the same time, highly accurate monitoring of the position of the probe is possible.

8 Summary and future challenges

This work consists of two major parts: The design and evaluation of the Motor Assisted Robotic Stereotaxy system (MARS) and the adaptation of a new localization method based on static magnetic fields for stereotactic neurosurgery. Both are briefly summarized and future challenges are discussed.

8.1 Summary MARS

In the scope of this thesis, a robotic system for stereotactic neurosurgery was designed and evaluated.

The center of arc kinematic chain of the robot consists of five fully automated axes. They allow for highly accurate positioning of probes in the brain of the patient. The kinematic chain is derived from the manual ZD stereotaxy system. Two points are crucial in this context: First, the use of a known kinematic chain aims for higher acceptance among neurosurgeons. Second, the decoupling of translational and rotational parts of the end-effector pose allows for intuitive handling and simplifies the kinematic calculations.

Each axis is equipped with two position encoders, one of them being an absolute encoder. This significantly reduces the risk of faulty positioning of the probe. Furthermore, manual scales indicate the positions of the axes. No safety zone is required, as an application specific kinematic chain was designed for the MARS. The surgeon can switch between automatic and manual positioning, which further enhances the range of applications.

The MARS can easily be transported on its modified instrument table. As it mounts to the side rails of operating tables, it can be used in standard operating theaters. Both features allow for easy integration of the MARS into the surgical workflow. Furthermore, it is compatible to standard equipment of the industrial partner inomed Medizintechnik GmbH.

Experiments to specify the properties of the MARS were conducted. The aim was to demonstrate that the system qualifies for clinical use. First, its absolute accuracy (mean deviation 0.23 mm) and repeatability (mean error 0.06 mm) were evaluated. Second, the electromagnetic compliance of the system with micro electrode recording (MER) equipment was shown. Third, the accuracy of the tool chain involved in stereotactic neurosurgery was evaluated by measuring the application accuracy of the system. With a mean error of 0.60 mm, the application accuracy of MARS is superior to other robotic and manual stereotactic devices.

After successfully passing these tests, the MARS was evaluated in a clinical trial. MARS was integrated into the surgical workflow for a tumor biopsy without difficulties. Its probe was positioned according to the preoperative plan and a number of specimens was collected. During and after the surgery, no complications occurred.

All in all, the Motor Assisted Robotic Stereotaxy system presents a highly accurate, save and mobile tool for stereotactic neurosurgery. Due to its hybrid character, the system qualifies for a great variety of surgical procedures. The presented results and successful clinical evaluation of the robot indicate that the developed system meets the requirements for stereotactic neurosurgery.

8.2 Summary magnetic probe localization

The design and implementation of the new probe localization methods presents the second pillar of this work. It is merely based on the static magnetic field inherently generated by ferromagnetic probes, e.g. macro electrodes or small permanent magnets. Existing instruments can be equipped with small permanent magnets or can be magnetized themselves. There is no need for further changes to instruments or additional hardware. This qualifies the magnetic probe localization method for use in stereotactic neurosurgery.

This work spans from first proof of concept experiments, via the selection of magnetic field sensors and the electric design, to the implementation of the localization algorithm.

Additionally, the integration into the MARS was covered. Two localization algorithms were implemented and experiments were conducted to quantify their accuracy. The results indicate that highly accurate tracking of probes inside the human brain based on their inherent static magnetic field is possible. The integration of this new localization approach into the MARS further enhances the safety of the system. Furthermore, it

is the first step towards closed-loop control over the probe position in the brain of the patient.

8.3 Future challenges MARS

The MARS is a prototype and potential for further improvement was identified. A more rigid structure for the arc is desirable. As discussed in Section 4.4, the bending of the arc under load necessitates a calibration. With a more rigid structure, this could be avoided. Beside the rigidity, also the workspace of the robot needs to be adapted to match the manual ZD frame. At the same time the overall weight of the system should not be enlarged. This presents a challenge for the future design.

The application accuracy of the MARS was studied in Section 6.4. One limitation of the presented study is the missing probe-tissue interaction. The probe could deflect which would reduce the overall accuracy. A study should be conducted, that includes probe-tissue interaction.

The implementation of a frame-less mode would further improve the system. No stereotactic base unit would be required to fix the patient's head. A head holder on the MARS could limit the movement of the skull in first order. A laser scanning system could track the head and register it to the coordinate system of the robot. This approach would greatly reduce the burden of the patient as no ring or other frame would be fixed to his head. A research group at this institute is working on the development of such a head tracking system.

The compatibility to other existing systems, e.g. Leksell frame, presents another challenge for future development. In this scope, also the integration into the OT needs to be considered. Integrated OTs, e.g. NavSuite (Stryker Corporation, USA) [142] or OR1Neo (Karl Storz GmbH & Co. KG, Germany) [143], are a new development in the field of operating theaters. The idea is to control all equipment of the OT with one single user interface. The surgeon only needs to learn the handling of one software to control all surgical equipment. This concept could be extended to medical robots such as the MARS.

8.4 Future challenges magnetic probe localization

Current model based approaches are limited to magnetic dipoles. This limits the number of instruments that qualify for the localization technique. They need to be made of non-magnetic material and incorporate a small permanent magnet, which is not always possible. The use of a finite element method (FEM) simulation software could help to overcome the problem.

The geometry of the object, e.g. scalpel, could be modeled in CAD or recorded by a 3D scanner. Furthermore, the material and magnetic properties would be assigned to the object. Then, the magnetic flux could be calculated by the software. This theoretical magnetic flux data could be used for the localization of the object. A numerical solver could be used to minimize the difference between the measured magnetic flux and the flux predicted by the FEM model.

The presented magnetic probe localization is used to monitor the position of instruments inside the brain. So far, there are no means to change the orientation of the probe once inside the brain. The generation of a system for closed-loop control of the position of the probe is highly desirable. Faulty positioning of the probe could be corrected during the intervention. One of the following two options could be implemented in the MARS: First, external magnetic fields can be used to alter the position or orientation of probes in the patient (e.g. Niobe System, Stereotaxis Inc., USA [144]). Here, the magnet would present the signal source for the localization and also the instrument to manipulate the position of the probe. The second option is the combination of the MARS with conventional needle-steering methods, e.g. duty-cycled spinning [145] or pre-bent cannulas [146]. The magnet would be incorporated in the tip of the probe. The realization of such a system is ongoing work at the institute.

List of Figures

List of Tables

Bibliography

[1] Joachim Kraus and J. Volkmann. *Tiefe Hirnstimulation*. Steinkopff Verlag Darmstadt, 2004.

[2] Andres A. Lozano, Phillip L. Gildenberg, and R. Tasker. *Textbook of Stereotactic and Functional Neurosurgery*. Springer-Verlag, Berlin Heidelberg, 2nd. edition, 2009.

[3] Patrick Kelly. *Tumor stereotaxis*. W.B. Saunders Company, Philadelphia, PA 19106, USA, 1. edition, 1991.

[4] Moskopp and Wassmann. *Neurochirurgie*. Schattauer GmbH, Stuttgart 70174, Germany, 1. edition, 2005.

[5] R. L. Nussbaum and C. E. Ellis. Alzheimer's disease and Parkinson's disease. *N. Engl. J. Med.*, 348(14):1356–1364, Apr 2003.

[6] L.J. Findley. The economic impact of parkinson's disease. *Parkinsonism & Related Disorders*, 13:S8–S12, 2007.

[7] Berufsverbandes Deutscher Neurologen (BDN) Deutsche Gesellschaft für Neurologie DGN. Patienten-leitlinie des berufsverbandes deutscher neurologen (bdn) und der deutschen gesellschaft für neurologie (dgn). Patienten Leitlinie, 2008.

[8] M. Schirmer. *Neurochirurgie*. Elsevier GmbH, Urban & Fischer Verlag, 80333 München, Karlstrasse 45, 10th edition, 2005.

[9] Wassilios Meissner, Doreen Schreiter, Jens Volkmann, Thomas Trottenberg, Gerd-Helge Schneider, Volker Sturm, Guenther Deuschl, and Andreas Kupsch. Deep brain stimulation in late stage parkinson's disease: a retrospective cost analysis in germany. *Journal of Neurology*, 252:218–223, 2005. 10.1007/s00415-005-0640-3.

[10] M. Krause, W. Fogel, A. Heck, W. Hacke, M. Bonsanto, C. Trenkwalder, and V. Tronnier. Deep brain stimulation for the treatment of parkinson's disease: subthalamic nucleus versus globus pallidus internus. *Journal of Neurology, Neurosurgery & Psychiatry*, 70(4):464, 2001.

[11] R. Levy, JO Dostrovsky, AE Lang, E. Sime, WD Hutchison, and AM Lozano. Effects of apomorphine on subthalamic nucleus and globus pallidus internus neurons in patients with parkinson's disease. *Journal of neurophysiology*, 86(1):249–260, 2001.

[12] P. Krack, P. Pollak, P. Limousin, D. Hoffmann, J. Xie, A. Benazzouz, and AL Benabid. Subthalamic nucleus or internal pallidal stimulation in young onset parkinson's disease. *Brain*, 121(3):451, 1998.

[13] A. Peppe, M. Pierantozzi, A. Bassi, M.G. Altibrandi, L. Brusa, A. Stefani, P. Stanzione, and P. Mazzone. Stimulation of the subthalamic nucleus compared with the globus pallidus internus in patients with parkinson disease. *Journal of neurosurgery*, 101(2):195–200, 2004.

[14] P. Pollak, V. Fraix, P. Krack, E. Moro, A. Mendes, S. Chabardes, A. Koudsie, and A. L. Benabid. Treatment results: Parkinson's disease. *Movement disorders*, 17(S3):S75–S83, 2002.

[15] G. Schaltenbrand and W. Wahren. *Atlas for stereotaxy of the human brain.* Thieme Stuttgart, 1977.

[16] P. Talairach and J. Tournoux. A stereotactic coplanar atlas of the human brain, 1988.

[17] J. Voges, J. Volkmann, N. Allert, R. Lehrke, A. Koulousakis, H.J. Freund, and V. Sturm. Bilateral high-frequency stimulation in the subthalamic nucleus for the treatment of parkinson disease: correlation of therapeutic effect with anatomical electrode position. *Journal of neurosurgery*, 96(2):269–279, 2002.

[18] J.H. Lee. *Meningiomas: diagnosis, treatment, and outcome.* Springer Verlag, 2009.

[19] Zentrum für Krebsregisterdaten. *Krebs in Deutschland 2007/2008*, volume 8. Robert Koch Institut, 2012.

[20] William A. Friedman, James D. Jr. Sceats, Blake R. Nestok, and William E. Jr. Ballinger. The incidence of unexpected pathological findings in an image-guided biopsy series: A review of 100 consecutive cases. *Neurosurgery*, 2 25:180–184, 1989.

[21] Corinne Bouvier, Patrice Roll, Benoit Quilichini, Philippe Metellus, Arlette Calisti, Sophie Gilles, Olivier Chinot, Frederic Fina, Pierre Martin, and Dominique Figarella-Branger. Deletions of chromosomes 1p and 19q are detectable on frozen smears of gliomas by fish: Usefulness for stereotactic biopsies. *Journal of Neuro-Oncology*, 68:141–149, 2004. 10.1023/B:NEON.0000027758.10286.c1.

[22] E. M. Housepian and J. L. Pool. The accuracy of human stereo- encephalotomy as judged by histological confirmation of roentgenographic localization. *The Journal of Nervous and Mental Disease*, 130:520–525, 1960.

[23] S. Kalyanaraman and F. J. Gillingham. Stereotaxic biopsy. *Journal of neurosurgery*, 21:854, 1964.

[24] M. Bergstrom and T. Greitz. Stereotaxic computed tomography. *American Journal of Roentgenology*, 127:167–170, 1976.

[25] L. D. Lunsford, R. J. Coffey, T. Cojocaru, and D. Leksell. Image-guided stereotactic surgery: A 10-year evolutionary experience. *Stereotactic and Functional Neurosurgery, Stereotact Funct Neurosurg*, 54(1-8):375–387, 1990.

[26] X. Yu, Z. Liu, Z. Tian, S. Li, H. Huang, B. Xiu, Q Zhao, L. Liu, and W. Jing. Stereotactic biopsy for intracranial space-occupying lesions: Clinical analysis of 550 cases. *Stereotactic and Functional Neurosurgery, Stereotact Funct Neurosurg*, 75(2-3):103–108, 2000.

[27] Sedan R., Peragut J.C., and Vallincioni P. Prèsentation d'un appareillage original pour biopsie cèrèbrale et tumorale en condition stèrèotactiques. *Communication à la Societè de Neurochirurgie de Langue Francaise*, 1975.

[28] C.R. Wirtz, M.M. Bonsanto, M. Knauth, V.M. Tronnier, F.K. Albert, A. Staubert, and S. Kunze. Intraoperative magnetic resonance imaging to update interactive navigation in neurosurgery: Method and preliminary experience. *Computer Aided Surgery*, 2(3-4):172–179, 1997.

[29] W.E.L. Grimson, GJ Ettinger, SJ White, T. Lozano-Perez, WM Wells Iii, and R. Kikinis. An automatic registration method for frameless stereotaxy, image guided surgery, and enhanced reality visualization. *Medical Imaging, IEEE Transactions on*, 15(2):129–140, 1996.

[30] R.R. Shamir, L. Joskowicz, S. Spektor, and Y. Shoshan. Localization and registration accuracy in image guided neurosurgery: a clinical study. *International journal of computer assisted radiology and surgery*, 4(1):45–52, 2009.

[31] L.G. Brown. A survey of image registration techniques. *ACM computing surveys (CSUR)*, 24(4):325–376, 1992.

[32] E.I. Kandel and Y.V. Schavinsky. Stereotaxic apparatus and operations in russia in the 19th century. *Journal of neurosurgery*, 37(4):407–411, 1972.

[33] Claude Picard, Andre Olivier, and Gilles Bertrand. The first human stereotaxic apparatus. *Journal of Neurosurgery*, 59(4):673–676, 1983. PMID: 6350539.

[34] Spiegel E.A., Wycis H.T., Marks M., and Lee A.S. Stereotaxic apparatus for operations on the human brain. *Science*, 106:349–350, 1947.

[35] Michael Schulder, editor. *Handbook of stereotactic and functional neurosurgery*. Marcel Dekker Inc, New York, Basel, 270 Madison Avenue, New York, 2003.

[36] Robert J. Maciunas, Robert L. Galloway, and Jim W. Latimer. The application accuracy of stereotactic frames. *Neurosurgery*, 35(4):682–695, 1994.

[37] Riechert T. and F. Mundinger. Beschreibung und Anwendung eines Zielgerätes für stereotaktische Hirnoperationen (ii. Modell)). *Acta Neurochir*, Suppl. 3:308–337, 1955.

[38] Talairach J., David M., and Tournoux P. *Exploration chirurgicale stereotaxique du lobe temporal*. Manon et Cie, Paris, 1985.

[39] L. Leksell. A stereotaxic apparatus for intracerebral surgery. *Acta Chir Scand*, 99:229–233, 1949.

[40] M. F. Pell and D. G. Thomas. The initial experience with the Cosman-Roberts-Wells stereotactic system. *Br J Neurosurg*, 5:123–128, 1991.

[41] L. Zamorano, M. Kadi, Z. Jiang, and F. Diaz. Zamorano-Dujovny multipurpose neurosurgical image-guided localizing unit: experience in 866 consecutive cases of 'open stereotaxis'. *Stereotact Funct Neurosurg*, 63:45–51, 1994.

[42] G. M. Austin, A. S. Lee, and F. C. Grant. A new type of locally applied stereotaxic instrument. *Journal of American Medical Association*, 161:147–148, 1956.

[43] Carol M. A true "advanced imaging assisted" skull-mounted stereotactic system. *Appl Neurophysiol*, 48:69–72, 1985.

[44] Jaimie M. Henderson, Kathryn L. Holloway, Steven E. Gaede, and Joshua M. Rosenow. The application accuracy of a skull-mounted trajectory guide system for image-guided functional neurosurgery. *Computer Aided Surgery*, 9(4):155–160, 2004.

[45] Riechert T. and Wolff M. Über ein neues Zielgerät zur intrakraniellen elektrischen Ableitung und Ausschaltung. *Arch Psychiat Z Neurol*, 186:225–230, 1951.

[46] J. K. Kraus. The Riechert/Mundinger Stereotactic Apparatus. In *Textbook of Stereotactic and Functional Neurosurgery*, chapter 31, pages 487–494. Springer-Verlag, 2nd. edition, 2009.

[47] W. J. Levy. Simple plastic stereotactic unit for use in the computed tomographic scanner. *Neurosurgery*, 13:182–185, Aug 1983.

[48] A. A. Patil. Compute tomography-oriented stereotactic system (comment). *Neurosurgery*, 10:370–374, Mar 1982.

[49] Graeme F Woodworth, Matthew J McGirt, Amer Samdani, Ira Garonzik, Alessandro Olivi, and Jon D Weingart. Frameless image-guided stereotactic brain biopsy procedure: diagnostic yield, surgical morbidity, and comparison with the frame-based technique. *Journal Of Neurosurgery*, 104(2):233–237, 2006.

[50] Graeme Woodworth, Matthew J McGirt, Amer Samdani, Ira Garonzik, Alessandro Olivi, and Jon D Weingart. Accuracy of frameless and frame-based image-guided stereotactic brain biopsy in the diagnosis of glioma: comparison of biopsy and open resection specimen. *Neurological Research*, 27(4):358–362, 2005.

[51] Roy A. E. Barkay. *Movement Disorder Surgery: The Essentials*. Thieme Medical Publishers, Inc, New York, 2008.

[52] Medtronic. Nexframe stereotactic system manual. Technical report, Medtronic Inc Minneapolis USA, October 2010. Available online at http://professional.medtronic.com/; accessed 04/2012.

[53] T. M. Soo, M. Bernstein, J. Provias, R. Tasker, A. Lozano, and A. Guha. Failed stereotactic biopsy in a series of 518 cases. *Stereotactic and Functional Neurosurgery*, 64:183–196, 1995.

[54] AL Benabid, P. Cinquin, S. Lavalle, JF Le Bas, J. Demongeot, and J. De Rougemont. Computer-driven robot for stereotactic surgery connected to ct scan and magnetic resonance imaging. *Stereotactic and Functional Neurosurgery*, 50(1-6):153–154, 1987.

[55] Y. S. Kwoh, J. Hou, EA Jonckheere, and S. Hayati. A robot with improved absolute positioning accuracy for ct guided stereotactic brain surgery. *Biomedical Engineering, IEEE Transactions on*, 35(2):153–160, February 1988.

[56] J. M. Drake, M. Joy, A. Goldenberg, and D. Kreindler. Computer-and robot-assisted resection of thalamic astrocytomas in children. *Neurosurgery*, 29(1):27, 1991.

[57] Russel A. Faust. *Robotics in surgery: history, current and future applications.* Nova Science Pub Inc, 1. edition, August 2006.

[58] Chris Karas and Antonio Chiocca. Neurosurgical robotics: a review of brain and spine applications. *Journal of Robotic Surgery*, 1(1):39–43, February 2007.

[59] MS Eljamel. Robotic neurological surgery applications: accuracy and consistency or pure fantasy. *Stereotact Funct Neurosurg*, 87(2):88–93, 2009.

[60] A. L. Benabid, P. Cinquin, S. Lavalle, J. F. Le Bas, J. Demongeot, and J. de Rougemont. Computer-driven robot for stereotactic surgery connected to CT scan and magnetic resonance imaging. Technological design and preliminary results. *Appl Neurophysiol*, 50:153–154, 1987.

[61] Q. H. Li, L. Zamorano, A. Pandya, R. Perez, J. Gong, and F. Diaz. The application accuracy of the neuromate robot-a quantitative comparison with frameless and frame-based surgical localization systems. *Computer Aided Surgery*, 7(2):90–98, 2002.

[62] P.A. Finlay. Pathfinder: a new image guided robot for neurosurgery. *Technology and Health Care*, 9(1-2):160–161, 2001.

[63] P. S. Morgan, T. Carter, S. Davis, A. Sepehri, J. Punt, P. Byrne, A. Moody, and P. Finlay. The application accuracy of the pathfinder neurosurgical robot. *International Congress Series CARS 2003. Computer Assisted Radiology and Surgery. Proceedings of the 17th International Congress and Exhibition*, pages 561–567, 2003.

[64] Medtech. Rosa neurosurgery robot. Technical report, Medtech SAS Montpellier France, November 2011. Available online at http://www.medtechsurgical. com/Products/ROSA; accessed 04/2012.

[65] Arata Jumpei, Ikemoto Junichi, Sakaguchi Masamichi, and Fujimoto Hideo. Development of the surgical motion base system using a parallel link mechanism. *Proceedings of the Asian Conf. on Computer Aided Surgery (ACCAS)*, page 110076, 2007.

[66] J. Arata, Y. Tada, H. Kozuka, T. Wada, Y. Saito, N. Ikedo, Y. Hayashi, M. Fujii, Y. Kajita, M. Mizuno, et al. Neurosurgical robotic system for brain tumor removal. *International journal of computer assisted radiology and surgery*, 6(3):375–385, 2011.

[67] M. Haun. *Handbuch Robotik, Programmieren und Einsatz intelligenter Roboter*. Springer, Heidelberg, xviii edition, 2007.

[68] C. Nimsky, O. Ganslandt, P. Hastreiter, and R. Fahlbusch. Intraoperative compensation for brain shift. *Surgical neurology*, 56(6):357–364, 2001.

[69] D. W. Roberts, A. Hartov, F. E. Kennedy, M. I. Miga, and K. D. Paulsen. Intraoperative brain shift and deformation: a quantitative analysis of cortical displacement in 28 cases. *Neurosurgery*, 43(4):749–758, Oct 1998.

[70] Richard Bucholz, David Yeh, Jason Trobaugh, Leslie McDurmont, Christopher Sturm, Carol Baumann, Jaimie Henderson, Ari Levy, and Paul Kessman. The correction of stereotactic inaccuracy caused by brain shift using an intraoperative ultrasound device. In Jocelyne Troccaz, Eric Grimson, and Ralph Mösges, editors, *CVRMed-MRCAS'97*, volume 1205 of *Lecture Notes in Computer Science*, pages 459–466. Springer Berlin / Heidelberg, 1997. 10.1007/BFb0029268.

[71] N. Abolhassani and R. V. Patel. Deflection of a flexible needle during insertion into soft tissue. *Conf Proc IEEE Eng Med Biol Soc*, 1:3858–3861, 2006.

[72] S. Misra, K.B. Reed, A.S. Douglas, KT Ramesh, and A.M. Okamura. Needle-tissue interaction forces for bevel-tip steerable needles. In *Biomedical Robotics and Biomechatronics, 2008. BioRob 2008. 2nd IEEE RAS & EMBS International Conference on*, pages 224–231. IEEE, 2008.

[73] O. Dössel. *Bildgebende Verfahren in der Medizin - von der Technik zur medizinischen Anwendung.* Springer Verlag, Berlin-Heidelberg, 2000.

[74] Northern Digital Inc. Canada. The Aurora Electromagnetic Measurement System, 2011. Available online at http://www.ndigital.com/medical/aurora-techspecs.php; accessed 04/2011.

[75] E.C. Parker and P.J. Kelly. Engineering aspects of electromagnetic localization in image guided surgery. In *Textbook of Stereotactic and Functional Neurosurgery*, chapter 35, pages 535–541. Springer-Verlag, 2nd. edition, 2009.

[76] Werner Weitschies, Olaf Kosch, Hubert Mönnikes, and Lutz Trahms. Magnetic marker monitoring: An application of biomagnetic measurement instrumentation and principles for the determination of the gastrointestinal behavior of magnetically marked solid dosage forms. *Advanced Drug Delivery Reviews*, 57(8):1210 – 1222, 2005.

[77] Helmut Kronmüller and Stuart Parkin. *Handbook of Magnetism and Advanced Magnetic Materials.* Wiley, 2007.

[78] R. Model and L. Trahms. An inverse problem of magnetic source localization. *Numerical Algorithms*, 5:603–610, 1993. 10.1007/BF02221587.

[79] K. Levenberg. A method for the solution of certain problems in least squares. *Quart. Appl. Math.*, 2:164–168, 1944.

[80] D. Marquardt. An algorithm for least-squares estimation of nonlinear parameters. *SIAM J. Appl. Math.*, 11:431–441, 1963.

[81] V. Schlageter, P.-A. Besse, R.S. Popovic, and P. Kucera. Tracking system with five degrees of freedom using a 2d-array of hall sensors and a permanent magnet. *Sensors and Actuators A: Physical*, 92(1):37–42, 2001.

[82] Chao Hu, Mao Li, Shuang Song, Wan'an Yang, Rui Zhang, and M.Q.-H. Meng. A cubic 3-axis magnetic sensor array for wirelessly tracking magnet position and orientation. *Sensors Journal, IEEE*, 10(5):903 –913, may 2010.

[83] C. Hu, M.Q.H. Meng, M. Mandal, and X. Wang. 3-Axis Magnetic Sensor Array System for Tracking Magnet's Position and Orientation. *The Sixth World Congress on Intelligent Control and Automation WCICA 2006*, 2:5304–5308, 2006.

[84] Werner Weitschies, Michael Karaus, Dino Cordini, Lutz Trahms, Jörg Breitkreutz, and Wolfhard Semmler. Magnetic marker monitoring of disintegrating capsules. *European Journal of Pharmaceutical Sciences*, 13(4):411 – 416, 2001.

[85] Wilfried Andrae, Matthias E Bellemann, M. Brand, J. Haueisen, H. Lausch, Pieter Saupe, and C.Werner. Magnetic marker monitoring using a permanent magnetic sphere oriented by a rotating magnetic field. *Proceedings of 4th European Conference of the International Federation for Medical and Biological Engineering IFMBE*, 22:1137–1140, 2008.

[86] B. Davies. A review of robotics in surgery. *Proceedings of the Institution of Mechanical Engineers, Part H: Journal of Engineering in Medicine*, 214(1):129, 2000.

[87] J. Pransky. Robodoc-surgical robot success story. *Industrial Robot: An International Journal*, 24(3):231–233, 1997.

[88] W.L. Bargar, A. Bauer, and M. Börner. Primary and revision total hip replacement using the robodoc (r) system. *Clinical orthopaedics and related research*, 354:82, 1998.

[89] Arndt P. Schulz, Klaus Seide, Christian Queitsch, Andrea von Haugwitz, Jan Meiners, Benjamin Kienast, Mohamad Tarabolsi, Michael Kammal, and Christian Jürgens. Results of total hip replacement using the robodoc surgical assistant system: clinical outcome and evaluation of complications for 97 procedures. *The International Journal of Medical Robotics and Computer Assisted Surgery*, 3(4):301–306, 2007.

[90] Michael Nogler, Anne Polikeit, Cornelius Wimmer, Andreas Brückner, Stephen J Ferguson, and Martin Krismer. Primary stability of a robodoc® implanted

anatomical stem versus manual implantation. *Clinical Biomechanics*, 19(2):123–129, 2004.

[91] NN. Robodoc-Fall Risiken neuer Operationsmethoden müssen klar sein. *Frankfurter Allgemeine Zeitung*, 2006.

[92] NN. Robodoc-Verfahren. *Bundesinstitut für Arzneimittel und Medizinprodukte*, 2004. ID:921/0504.

[93] Peter Schräder and Harald Sieber. Roboterunterstützte Fräsverfahren am coxalen Femur bei Hüftgelenkstotalendoprothesenimplantation Methodenbewertung am Beispiel Robodoc. *Gutachten Medizinischer Dienst der Spitzenverbände der Krankenkassen e.V.*, 2004.

[94] K. Cleary, A. Kinsella, and S.K. Mun. Or 2020 workshop report: operating room of the future. In *International Congress Series*, volume 1281, pages 832–838. Elsevier, 2005.

[95] D.B. Camarillo, T.M. Krummel, J.K. Salisbury, et al. Robotic technology in surgery: past, present, and future. *The American Journal of Surgery*, 188:2–15, 2004.

[96] Charles F. Dalziel. Dangerous electric currents. *American Institute of Electrical Engineers, Transactions of the*, 65(8):579 –585, aug. 1946.

[97] J. M. Bronstein, M. Tagliati, R. L. Alterman, A. M. Lozano, J. Volkmann, A. Stefani, F. B. Horak, M. S. Okun, K. D. Foote, P. Krack, et al. Deep brain stimulation for parkinson disease: An expert consensus and review of key issues. *Archives of Neurology*, page online, 2010.

[98] Jorge Cham. *Piled Higher and Deeper*. The Stanford Daily Newspaper, 2006.

[99] Austin Hughes. *Electric Motors and Drives - Fundamentals, Types and Applications*. Elsevier, Linarce House, Jordan Hill, Oxford, 3 edition, 2006.

[100] P. Yedamale. Brushless dc (bldc) motor fundamentals. *Microchip Application Note: AN885,[Online]. Available: http://www.microchip.com/*, 2003.

[101] Dr. Fritz Faulhaber GmbH & Co. KG, Daimlerstr. 23 / 25, 71101 Schönaich, Germany. *Bedienungsanleitung Motion Controller Serie MCBL 3003/3006 S*, 4 edition, 2009.

[102] Dr. Fritz Faulhaber GmbH & Co. KG, Daimlerstr. 23 / 25, 71101 Schönaich, Germany. *Antriebssysteme*, 2011. Spezifikation Planetengetriebe Serie 16/7.

[103] Harmonic Drive AG. *Montage- und Wartungsanleitung Einbausätze Baureihe HFUC-2A-(G)R*. Harmonic Drive AG, Hoenbergstraße 14, 65555 Limburg/Lahn Germany, 2003.

[104] Megatron Elektronik AG & Co. Serie MBW / potentiometrisch. Technical datasheet, Hermann-Oberth-Str. 7, D-85640 Putzbrunn/München, 2011.

[105] H-TRONIC GmbH. Hb 627 – 8-kanaliges 12bit USB Datenerfassungsmodul. Technical datasheet, Industriegebiet Dienhof 11, D-92242 Hirschau, 2011.

[106] VTI Technologies Oy. The SCA100T dual axis inclinometer series. Technical datasheet, Myllynkivenkuja 6, P.O. Box 27, Vantaa FI-01621, 2011. Doc. Nr. 8261800, Rev. A.

[107] Alpha Omega Co USA Inc. NeuroNav drive, 2012. Available online at http://www.alphaomega-eng.com; accessed 02/2012.

[108] L. Richter, F. Ernst, V. Martens, L. Matthaeus, and A. Schweikard. Client/server framework for robot control in medical assistance systems. In *Proceedings of the 24th International Congress and Exhibition on Computer Assisted Radiology and Surgery (CARS'10)*, volume 5 of *International Journal of Computer Assisted Radiology and Surgery*, pages 306–307, June 2010.

[109] J. Denavit and R. S. Hartenberg. A kinematic notation for lower-pair mechanisms based on matrices. *Trans. of the ASME. Journal of Applied Mechanics*, 22:215–221, 1955.

[110] Lukas Ramrath, Achim Schweikard, and Ulrich G. Hofmann. Spherical assistant for stereotactic surgery. In *IROS 2007*, pages 859 – 864, October 2007.

[111] M. Neitzel, P. Mitschang, and G. Beresheim. *Handbuch Verbundwerkstoffe: Werkstoffe, Verarbeitung, Anwendung*. Hanser, Munich, 2004.

[112] K. Kozlowski. *Modelling and Identification in Robotics.* Springer, London, 1998.

[113] atracsys. Accutrack 250, 2011. Available online at http://atracsys.com/products/trackingsystems.php; accessed 08/2011.

[114] Benjamin Mooring, Morris Driels, and Zvi Roth. *Fundamentals of Manipulator Calibration.* John Wiley & Sons, Inc., New York, NY, USA, 1991.

[115] Ying Bai. On the comparison of model-based and modeless robotic calibration based on a fuzzy interpolation method. *The International Journal of Advanced Manufacturing Technology*, 31:1243–1250, 2007.

[116] L.K. Huat. *Industrial Robotics, Programming, Simulation, and Application.* Pro Literatur Verlag, Germany, 2006.

[117] W. Schottky. On the origins of photoelectrons in cu2 o-cu photocells. *Phys. Z.*, 31:913–925, 1930.

[118] H.J. Woltring. Single- and dual-axis lateral photodetectors of rectangular shape. *Electron Devices, IEEE Transactions on*, 22(8):581 – 590, aug 1975.

[119] G.P. Petersson and L.-E. Lindholm. Position sensitive light detectors with high linearity. *Solid-State Circuits, IEEE Journal of*, 13(3):392 – 399, jun 1978.

[120] I. Edwards. Using photodetectors for position sensing. *Sensor Magazine*, dec 1988.

[121] Anssi Maekynen. *Position-Sensitive Devices and Sensor Systems for optical Tracking and Displacement Sensing Application.* PhD thesis, University of Oulu, Department of electrical engineering, 2000.

[122] First Sensor AG Germany. *DL400-7SMD*, 2011.

[123] R. Bernhardt and S. Albright. *Robot Calibration.* Chapman & Hall, London, 1994.

[124] Henrik Andersson. *Position Sensitive Detectors - Device Technology and Applications in Spectroscopy.* PhD thesis, Electronics Design Division, in the Department of Information Technology and Media Mid Sweden University, SE-851 70 Sundsvall, Sweden, 2008.

[125] A. Agarwal and J. Lang. *Foundations of Analog and Digital Electronic Circuits.* Denise E. M. Penrose, 2005.

[126] Texas Instruments Incorporated USA. *16-Channel, 24 Bit Analog-to-digital converter ADS1258*, 2011.

[127] M. Heinig, R. Bruder, A. Schlaefer, and A. Schweikard. 3d localization of a thin steel rod using magnetic field sensors: Feasibility and preliminary results. In *Bioinformatics and Biomedical Engineering (iCBBE), 2010 4th International Conference on*, pages 1 –4, june 2010.

[128] Max Heinig, A. Schlaefer, and Achim Schweikard. 3d localization of ferromagnetic probes for small animal neurosurgery. In *Engineering in Medicine and Biology Society (EMBC), 2010 Annual International Conference of the IEEE*, pages 2321 –2324, 31 2010-sept. 4 2010.

[129] Amotech Inc Corea. *iM - 3501 Motion Sensor DAta Sheet V1.1*, 2009.

[130] E. Huber, M. Urban, and Forschungszentrum Karlsruhe. Technik und Umwelt. *Helmholtzspulen zur Kalibrierung von Magnetfeldsensoren.* FZKA–5643. Forschungszentrum Karlsruhe, 1995.

[131] M. Marinescu. *Elektrische und Magnetische Felder.* Springer-Verlag, Berlin, Heidelberg, New York, 2009.

[132] G. Lehner. *Elektromagnetische Feldtheorie fuer Ingenieure und Physiker.* Springer-Verlag Berlin Heidelberg New York, 2004.

[133] Maria Fernanda Govela, Jorge Martínez, and Max Heinig. Mars robot. In *XII Simposio Mexicano en Cirugía Asistida por Computadora y Procesamiento de Imágenes Médicas MEXCAS 2011*, September 2011.

[134] Max Heinig, Maria Fernanda Govela, Fernando Gasca, Christian Dold, Ulrich G. Hofmann, Volker Tronnier, Alexander Schlaefer, and Achim Schweikard. Mars - motor assisted robotic stereotaxy system. In *Proceedings of the 5th International IEEE EMBS Conference on Neural Engineering*, pages 334 – 337, May 2011.

[135] Max Heinig, Olaf Christ, Volker Tronnier, Ulrich G. Hofmann, Alexander Schlaefer, and Achim Schweikard. Electromagnetic noise measurement of the motor

assisted robotic stereotaxy system (mars). In Guang-Zhong Yang and Ara Darzi, editors, *Proceedings of the 4th Hamlyn Symposium on Medical Robotics*, volume 4, pages 63–64, June 2011.

[136] Max Heinig, Ulrich G. Hofmann, and Alexander Schlaefer. Calibration of the motor assisted robotic stereotaxy system: Mars. *International Journal of Computer Assisted Radiology and Surgery*, accepted for publication, 2012.

[137] H.W. Lilliefors. On the kolmogorov-smirnov test for the exponential distribution with mean unknown. *Journal of the American Statistical Association*, 64:387–389, 1969.

[138] Mohamed Slamani, Albert Nubiola, and Ilian Bonev. Assessment of the positioning performance of an industrial robot. *Industrial Robot: An International Journal*, 39(1):57–68, 2012.

[139] J. Rachinger, K. Bumm, J. Wurm, C. Bohr, U. Nissen, T. Dannenmann, M. Buchfelder, H. Iro, and C. Nimsky. A new mechatronic assistance system for the neurosurgical operating theatre: Implementation, assessment of accuracy and application concepts. *Stereotactic and Functional Neurosurgery, Stereotact Funct Neurosurg*, 85(5):249–255, 2007.

[140] C. Moll, A. Struppler, and Engel A. K. Intraoperative mikroelektrodenableitung in den basalganglien des menschen. *Neuroforum*, 2005.

[141] J. Voges, R. Schröder, H. Treuer, O. Pastyr, W. Schlegel, W. J. Lorenz, and V. Sturm. Ct-guided and computer assisted stereotactic biopsy. *Acta Neurochirurgica*, 125:142–149, 1993. 10.1007/BF01401842.

[142] Stryker Corporation. Stryker navsuite. Website, 2012. Available online at http://www.stryker.com/en-us/Solutions/iSuiteIntegratedOR/NavSuite/index.htm; accessed 05/2012.

[143] Karl Storz GmbH & Co. KG. Karl storz or1. Website, 2012. Available online at http://www.karlstorz.de/cps/rde/xchg/SID-C02542BA-1B7B9DA2/karlstorz/hs.xsl/522.htm; accessed 05/2012.

[144] Stereotaxis Inc. Stereotaxis Niobe System. Website, 2012. Available online at http://www.stereotaxis.com/niobe.html; accessed 06/2012.

[145] Johnathan A Engh, Gregg Podnar, Si Yi Khoo, and Cameron Riviere. Flexible needle steering system for percutaneous access to deep zones of the brain. In *Proceedings of the IEEE 32nd Annual Northeast Bioengineering Conference*, pages 103 – 104, April 2006.

[146] S. Okazawa, R. Ebrahimi, J. Chuang, S.E. Salcudean, and R. Rohling. Hand-held steerable needle device. *Mechatronics, IEEE/ASME Transactions on*, 10(3):285 –296, june 2005.